

## NASA Contractor Report 4104

# Experimental and Analytic Studies of the Triggered Lightning Environment of the F106B

Terence Rudolph, Calvin C. Easterbrook,  
Poh H. Ng, Robert W. Haupt, and  
Rodney A. Perala

*Electro Magnetic Applications, Inc.*  
*Denver, Colorado*

Prepared for  
Langley Research Center  
under Contract NAS1-17748



National Aeronautics  
and Space Administration

Scientific and Technical  
Information Division

1987

## TABLE OF CONTENTS

Chapter	Title	Page
1	<b>INTRODUCTION</b>	1
2	<b>MEASUREMENT OF THE ELECTRIC FIELD ENHANCEMENT FACTORS ON AN AIRCRAFT</b>	4
	2.1 Introduction	4
	2.2 The Test Configuration	5
	2.3 The Charge Measurement Instrumentation	15
	2.4 Measurements on Canonical Shapes	19
	2.5 Some Theoretical Support for the Measurement Anomalies	24
	2.6 Measurements on the F106B Scale Model	25
	2.7 Conclusions	28
3	<b>LIGHTNING CHANNEL MODELING</b>	30
	3.1 Introduction	30
	3.2 Equations Describing the Channel	30
	3.3 Results	35
4	<b>1984 DATA ANALYSIS AND INTERNAL WIRE MODELING</b>	45
	4.1 Introduction	45
	4.2 Lightning Current Analysis	45
	4.3 Internal Coupling and Internal Wire Modeling	49
5	<b>THE EFFECT OF THUNDERSTORM PARTICLES ON TRIGGERED LIGHTNING</b>	93
	5.1 Introduction	93
	5.2 The Effect of Particles on Corona Formation	93
	5.3 Mathematical Development	96
	5.4 Results	103
6	<b>SUMMARY AND CONCLUSIONS</b>	109
	6.1 Form Factor Measurement	109
	6.2 Lightning Channel Modeling	109
	6.3 Internal Wire Modeling	110
	6.4 Thunderstorm Particle Modeling	110
	<b>REFERENCES</b>	111

## LIST OF FIGURES

Figure	Title	Page
2.1	The Parallel Plate Test Configuration	7
2.2	The Charge Measurement Instrumentation	8
2.3	The Parallel Plate Configuration with Guard Rings Installed	8
2.4(a)	Axial Field Mapping for Plates without Guard Rings	9
2.4(b)	Radial Field Mapping for Plates without Guard Rings	10
2.5(a)	Axial Field Mapping for Plates with Guard Rings	11
2.5(b)	Radial Field Mapping for Plates with Guard Rings	12
2.6(a)	Axial Field Mapping for Plates with Guard Rings Connected by Resistors	13
2.6(b)	Radial Field Mapping for Plates with Guard Rings Connected by Resistors	14
2.7	The Calibration Test Articles	16
2.8	The Charge Measuring Circuits	17
2.9	The Charge Transfer Probe Configuration	18
2.10	Correlation Between Measurements and Analytical and Finite Difference Solutions for Form Factors	21
2.11	Side View of F106B Showing Test Point Locations	26
2.12	Top View of F106B Showing Test Point Locations	26
2.13	Bottom View of F106B Showing Test Point Locations	27
3.1	Air Conductivity at Selected Distances from the Aircraft	36
3.2	Channel Current Two Meters from Aircraft	40
3.3	Electron Density Six Meters from Aircraft	41
3.4	Positive Ion Density Six Meters from Aircraft	42

## LIST OF FIGURES (cont'd)

Figure	Title	Page
3.5	Negative Ion Density Six Meters from Aircraft	43
4.1	Block Model of the F106B Indicating Approximate Sensor Locations	46
4.2	Typical Model Geometry for Triggered Lightning	47
4.3(a)	Measured versus Predicted I-dot Nose Waveforms	50
4.3(b)	Measured versus Predicted I-dot Nose Waveforms	51
4.3(c)	Measured versus Predicted I-dot Nose Waveforms	52
4.3(d)	Measured versus Predicted I-dot Nose Waveforms	53
4.3(e)	Measured versus Predicted I-dot Nose Waveforms	54
4.3(f)	Measured versus Predicted I-dot Nose Waveforms	55
4.3(g)	Measured versus Predicted I-dot Nose Waveforms	56
4.3(h)	Measured versus Predicted I-dot Nose Waveforms	57
4.3(i)	Measured versus Predicted I-dot Nose Waveforms	58
4.3(j)	Measured versus Predicted I-dot Nose Waveforms	59
4.3(k)	Measured versus Predicted I-dot Nose Waveforms	60
4.4	I-dot Nose Waveforms for Possible Multiple Strike Events	61
4.5	Fuselage and Wing Wire Configuration in the F106B	63
4.6(a)	Measured versus Predicted Internal Wire Responses	66
4.6(b)	Measured versus Predicted Internal Wire Responses	67
4.6(c)	Measured versus Predicted Internal Wire Responses	68
4.6(d)	Measured versus Predicted Internal Wire Responses	69

## LIST OF FIGURES (cont'd)

<b>Figure</b>	<b>Title</b>	<b>Page</b>
4.6(e)	Measured versus Predicted Internal Wire Responses	70
4.6(f)	Measured versus Predicted Internal Wire Responses	71
4.7(a)	Predicted Internal Wire Responses	72
4.7(b)	Predicted Internal Wire Responses	73
4.7(c)	Predicted Internal Wire Responses	74
4.7(d)	Predicted Internal Wire Responses	75
4.7(e)	Predicted Internal Wire Responses	76
4.7(f)	Predicted Internal Wire Responses	77
4.7(g)	Predicted Internal Wire Responses	78
4.7(h)	Predicted Internal Wire Responses	79
4.7(i)	Predicted Internal Wire Responses	80
4.7(j)	Predicted Internal Wire Responses	81
4.7(k)	Predicted Internal Wire Responses	82
4.7(l)	Predicted Internal Wire Responses	83
4.7(m)	Predicted Internal Wire Responses	84
4.7(n)	Predicted Internal Wire Responses	85
4.7(o)	Predicted Internal Wire Responses	86
4.7(p)	Predicted Internal Wire Responses	87
4.7(q)	Predicted Internal Wire Responses	88
4.7(r)	Predicted Internal Wire Responses	89
4.7(s)	Predicted Internal Wire Responses	90
4.7(t)	Predicted Internal Wire Responses	91

## LIST OF FIGURES (cont'd)

Figure	Title	Page
4.8	Predicted Internal Wire Responses for a Possible Multiple Strike Event	92
5.1	Electric Field Distribution Around a Typical Spherical Thunderstorm Particle. E <sub>o</sub> Is Ambient Field, Oriented Horizontally E <sub>b</sub> Is the Field Required for Air Breakdown	95
5.2	Spherical Coordinate System Used in the Thunderstorm Particle Analysis	98
5.3	F106B Responses for a Vertically Oriented Ambient Field with Thunderstorm Particles Absent	106
5.4	F106B Responses for a Vertically Oriented Ambient Field with Thunderstorm Particles Present	107

## LIST OF TABLES

Table	Title	Page
2.1	Form Factors for Fixed Sphere with Varying Probe Diameter Test Sphere Diameter is 3.3"	20
2.2	Form Factors for Varying Sphere Diameters but Fixed Probe (.125" dia.)	20
2.3	Form Factors for Varying Cylinder Diameters but Fixed Probe (.125" dia.) Long Cylinders Normal to Field	20
2.4	Computations and Measurements of the Form Factors Along a Finite Cylinder Oriented Along the Electric Field	23
2.5	Form Factor Measurements and Corrected Estimates	25
2.6	Comparisons of the Form Factors Obtained by Direct Measurement, by Finite Difference Analysis, and by Adjusting the Measured Values According to Correlation Data	28
4.1	Parameters Used in the Transmission Line Models of Internal F106B Wires	64
5.1	Definition of Symbols Used in Section 5.3	96
5.2	Nominal Air Breakdown Field as a Function of Air Density	104

## CHAPTER 1

### INTRODUCTION

It is clear from previous work [1-4] over the past six years that most, if not all, of the lightning strikes encountered by the NASA F106B thunderstorm research aircraft were triggered by the aircraft. This places increased importance on the investigation of the triggered lightning environment. The central question to be answered may be stated very simply: "Under what conditions will an aircraft trigger a lightning strike?" The answer to this question depends on a number of factors, the most important of which are listed below.

- 1) Electric field and charge distribution within the thundercloud, particularly near the aircraft;
- 2) Shape of the aircraft;
- 3) Orientation of the aircraft with respect to the ambient electric field;
- 4) Altitude of the aircraft;
- 5) Net electric charge on the aircraft;
- 6) Thunderstorm particle environment near the aircraft.

The local electric field in the vicinity of the aircraft is most influential in the generation of a triggered strike. It must be above a certain threshold in order for electrical corona to appear initially, and after a leader has developed and is propagating away from the aircraft, it serves to maintain that leader. The charge distribution within the cloud is, of course, responsible for the electric field distribution, and also provides a source of charge for K changes, or intracloud return strokes.

The shape of the aircraft is instrumental in enhancing an ambient electric field which is below air breakdown intensity up to a level at which air breakdown can occur. This normally occurs at locations having large field enhancements, such as the nose boom, wing tips, and tail of the F106B.



Orientation of the aircraft with respect to the ambient field is important because field enhancements are, in general, different for different directions of the field. As an example consider the F106B in level flight with an ambient electric field oriented from wing to wing. The largest local fields will be located at the wing tips of the aircraft, and may be below air breakdown intensity. If the aircraft now turns so that the ambient field is oriented along the fuselage, the largest local fields will be located at the nose. Because the field enhancement for this latter orientation is larger than for the former, it is possible that a triggered strike could be initiated. Hence some orientations of aircraft and field may be favored in triggering a lightning strike.

The altitude at which an aircraft flies influences the triggering process in that the minimum air breakdown field is a function of air density. The functional relationship is roughly linear with the breakdown field decreasing as the air density decreases. Therefore, for a given ambient electric field, triggering of lightning becomes more likely as an aircraft climbs in altitude.

In normal flight conditions an aircraft acquires a net electric charge through collisions with particles in the air. This net charge, if large enough, can significantly alter the ambient field level at which triggered lightning can occur. The alteration can be in either direction. Depending on a number of factors, one sign of charge may lower the triggering field, and the opposite sign of charge increase it.

Thunderstorm particles, in addition to providing a source of net charge on an aircraft through collisions, generate local volumes of enhanced fields. These particles, particularly ice particles, are irregularly shaped and conductive on static time scales. They can produce field enhancements of ten or more in a small volume surrounding the particle. This field enhancement in turn produces local corona. A large number density of these particles may then significantly alter the effective air breakdown characteristics in a region of space.

This report investigates various aspects of the triggered lightning environment. In Chapter 2 an effort is made to measure the form factors of the F106B aircraft with the use of a metallized plastic model placed in a uniform electric field. The measured form factors are compared with analytic and numerical form factors to validate the measurement technique. The form factors are important in that they allow one to determine the minimum triggering electric field for an aircraft. They may also be

used in the analysis of electric field mill records to derive ambient electric fields from local fields measured on the aircraft.

In Chapter 3 a two dimensional nonlinear lightning channel model is developed to investigate the late time (several microseconds) behavior of a triggered lightning event. Results from a simulated event are presented.

Chapter 4 details the analysis of internal wires on the F106B. Responses of both fuselage and wing wires have been recorded during triggered events. These wires are modeled using a linear triggered lightning model to obtain sources for the wires. The wires themselves are modeled as transmission lines with discrete sources and 50 ohm terminations. Results compare favorably to measured data.

Chapter 5 contains analysis relating to the effect thunderstorm particles have on a triggered lightning event. A general formalism is developed that allows one to vary size, shape, and density of these particles. A simulation is presented that shows the effect particles have on the responses measured on the F106B.

Chapter 6 presents a summary of the work documented here and a recap of the major conclusions.

## CHAPTER 2

# MEASUREMENT OF THE ELECTRIC FIELD ENHANCEMENT FACTORS ON AN AIRCRAFT

### 2.1 Introduction

The work discussed here stems from an attempt to determine experimentally the electric field form factors associated with locations of the field mills on the NASA F106B research aircraft. The experimental method chosen utilizes a small scale model aircraft, coated with a conductive paint, and immersed in the field produced between two large parallel plates. A small conductive probe is touched to the model at the appropriate location and the charge carried away from the surface is carefully measured. This is compared to the charge transferred to the probe after touching one of the parallel plates to get a value for the field enhancement. The method works because the net charge transferred to the probe from the test object is linearly dependent on the local electric field strength. This method has been utilized by others [5] and [6], but as far as is known, the accuracy of the method has never been reported.

Prior to making measurements on the model aircraft, tests were made with several simple shapes such as spheres, cylinders and cubes. The sphere and the infinite cylinder lying normal to the field direction can be solved analytically and thus serve as exact checks on the test technique. The cube and the finite cylinder oriented in the direction of the field were analyzed utilizing a very finely gridded finite difference method. Comparison of the form factors obtained from the analytical and finite difference solutions with measurements indicate that the experimental method has serious flaws. The errors involved increase with the magnitude of the form factors and can reach values of 200 to 300% for form factors of the order of 10 (easily reached near the extremes of a finite cylinder oriented along the field lines). As a result of this investigation, the experimental method is not recommended for calibration of field meters located on aircraft and should not be relied upon in any application where the local spatial derivatives of the electric field on the model are large over the dimensions of the probe to be used as a sensor.

In order to measure (or more correctly to infer) the ambient electric field in the free atmosphere, sensing instruments must be carried aloft by some vehicle such

as a balloon or aircraft. However, the presence of the vehicle and/or the instrument itself perturbs the ambient field, thus making the measurements incorrect. While this effect is indeed vexing, it does not necessarily preclude estimating the ambient field from measurements, since the measured field must certainly be proportional to the ambient field. The proportionality factor (or form factor) is a function of the geometry and material of the vehicle and is specific for a given point on the vehicle and a given ambient field direction. As a result, the task of estimating the ambient field from measurements taken near the conducting skin of a vehicle such as an aircraft rests very heavily on our ability to obtain accurate estimates of the form factor at the various sensor locations.

One method of obtaining the sensor location form factors is by mathematical modeling. The method of finite difference solutions to Maxwell's equations has been utilized for the NASA F106B research aircraft to compute form factors at the locations of the field mills. However, there is still some question as to the accuracy of these results since the computed values depend to some extent upon the cell size utilized in the model. Electric fields computed by this technique are averages over the dimensions of the cell. If fields are changing rapidly across the cell then local values may be significantly different than the computed value for the cell. For this reason, there has been a desire to check the results acquired through modeling by some other method.

Another method that has been utilized in the past to estimate aircraft form factors utilizes a scale-model aircraft in a parallel plate electric field. The model, which is coated with conductive paint, is touched at the points of concern with a small conducting probe. The charge transferred to the probe is proportional to the electric field in the region where the probe makes contact with the aircraft. By touching the aircraft and measuring the charge, and subsequently touching one of the end plates and measuring the charge, one can presumably estimate the form factor by computing the ratio of the charges transferred. It is this method that is the subject of the investigation discussed here.

## **2.2 The Test Configuration**

A 1:48 scale plastic model coated with a highly conductive silver paint is utilized for the F106B. The electric field is generated between 4' x 4' aluminum plates

separated by exactly one meter. A potential of 5 kV is applied between the plates by a dry cell battery pack, thereby maintaining a balanced system to ground. An unbalanced system with one plate grounded through a power supply was found to create problems with the charge transfer to the probe and led to significantly unbalanced charge transfer between one plate and the other. Isolating the system and keeping any net charge from residing on the plates or the test object cured this problem.

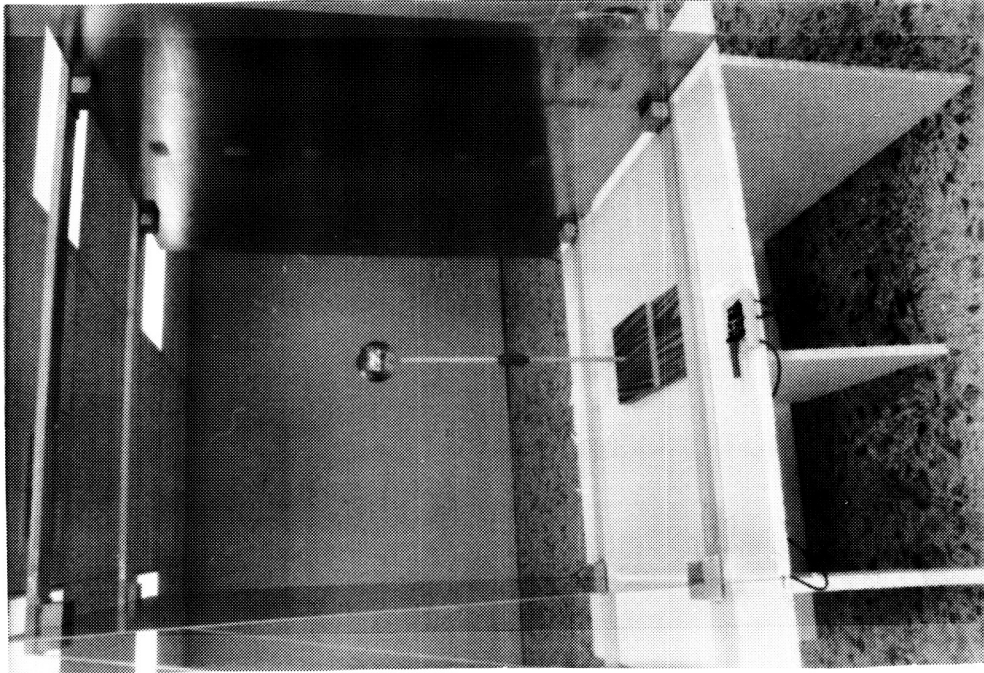
The test configuration initially set up for measurements on the model aircraft is shown in Figure 2.1(a). Figure 2.1(b) shows one of the test spheres mounted in the same parallel plate system. Figure 2.2 shows the charge measurement instrumentation. A Keithley Model 616 electrometer was used for charge measurement in a modified "ice pail" arrangement.

During the early measurements, it was found that a non-uniform field existed between the plates, giving rise to an error of a few percent. Therefore, a system of guard rings coupled to each other with 10 megohm resistors was installed between the plates and is shown in Figure 2.3. The field with guard rings in place was found to be uniform within a small fraction of 1%.

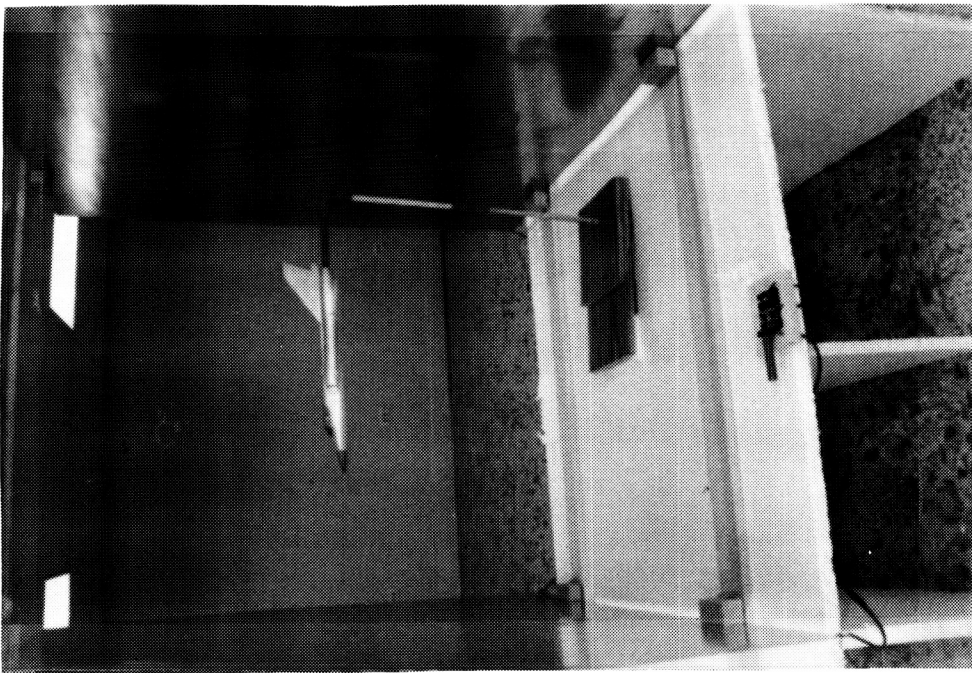
Numerical modeling of the parallel plate test arrangement was performed to verify the quality of the field distribution between the plates. This modeling was done using two dimensional cylindrical symmetry to increase spatial resolution as much as possible. Therefore, the plates, rather than being square as in the experimental situation, were round. Similarly the modeled guard rings had a circular shape rather than square. The area of the modeled plates was chosen to match that of the real square plates. A fixed potential was imposed between the modeled plates and the static field distribution calculated using the finite difference technique. Results of the analysis are shown in Figures 2.4 - 2.6. Figure 2.4 shows contour maps of the axial and radial electric field magnitudes for the plates without guard rings. Only one quadrant is shown, as symmetry exists around the axis and the center line between the plates. Also, the field magnitude shown is normalized to that at the exact center of either plate. Note in particular the distinct falloff in field near the center between the plates, due entirely to edge effects.

(text continued on page 15)

ORIGINAL PAGE IS  
OF POOR QUALITY



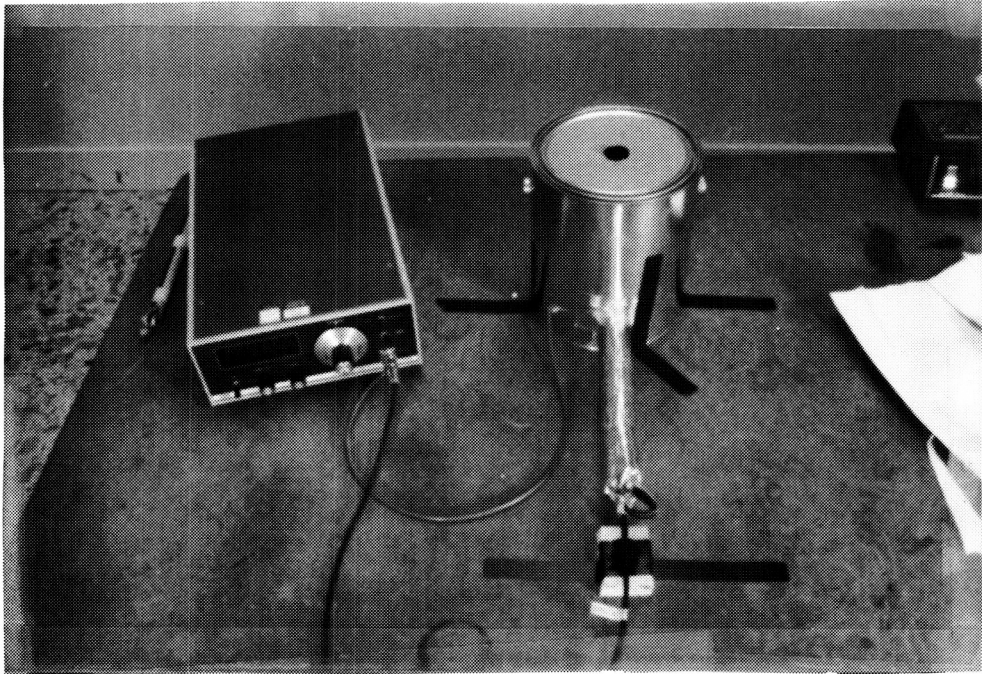
(b) 3.3 Inch Diameter Sphere



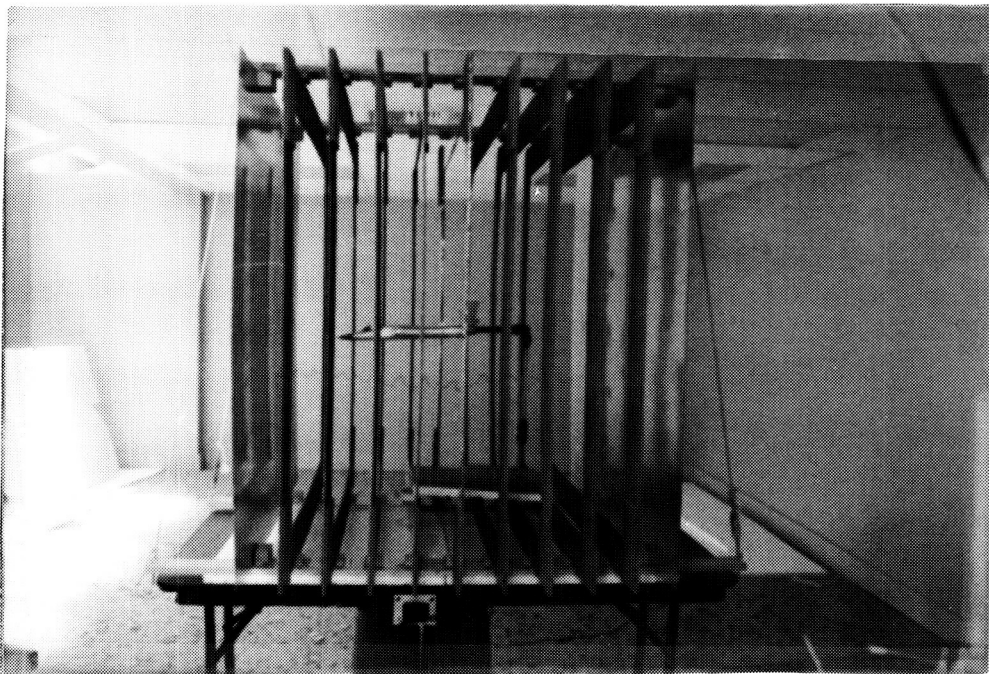
(a) F-106 Model

Figure 2.1 The Parallel Plate Test Configuration

ORIGINAL PAGE IS  
OF POOR QUALITY



**Figure 2.2** The Charge Measurement Instrumentation



**Figure 2.3** The Parallel Plate Configuration with Guard Rings Installed

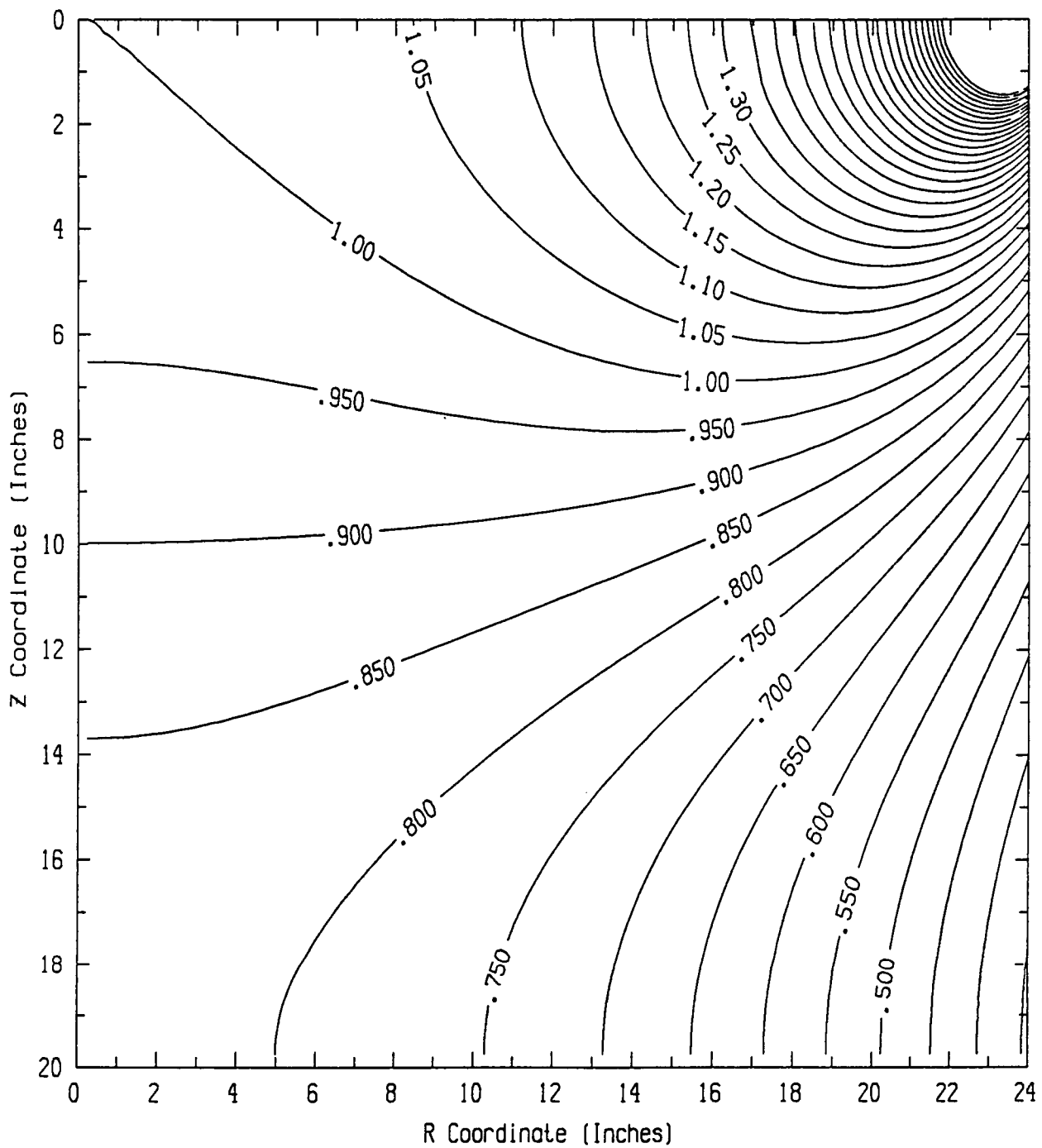


**Figure 2.4(a) Axial Field Mapping for Plates without Guard Rings**



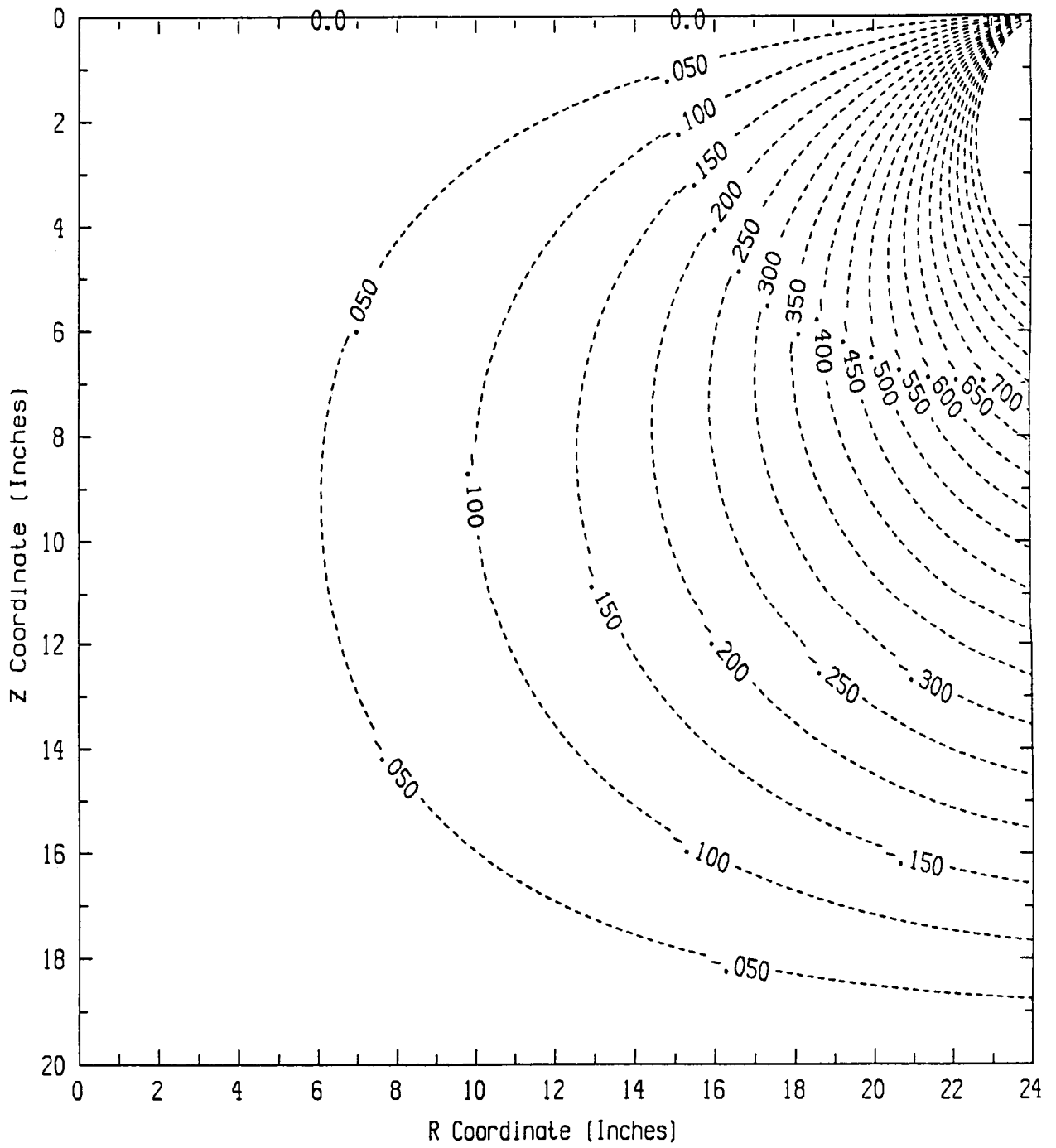


**Figure 2.4(b) Radial Field Mapping for Plates without Guard Rings**

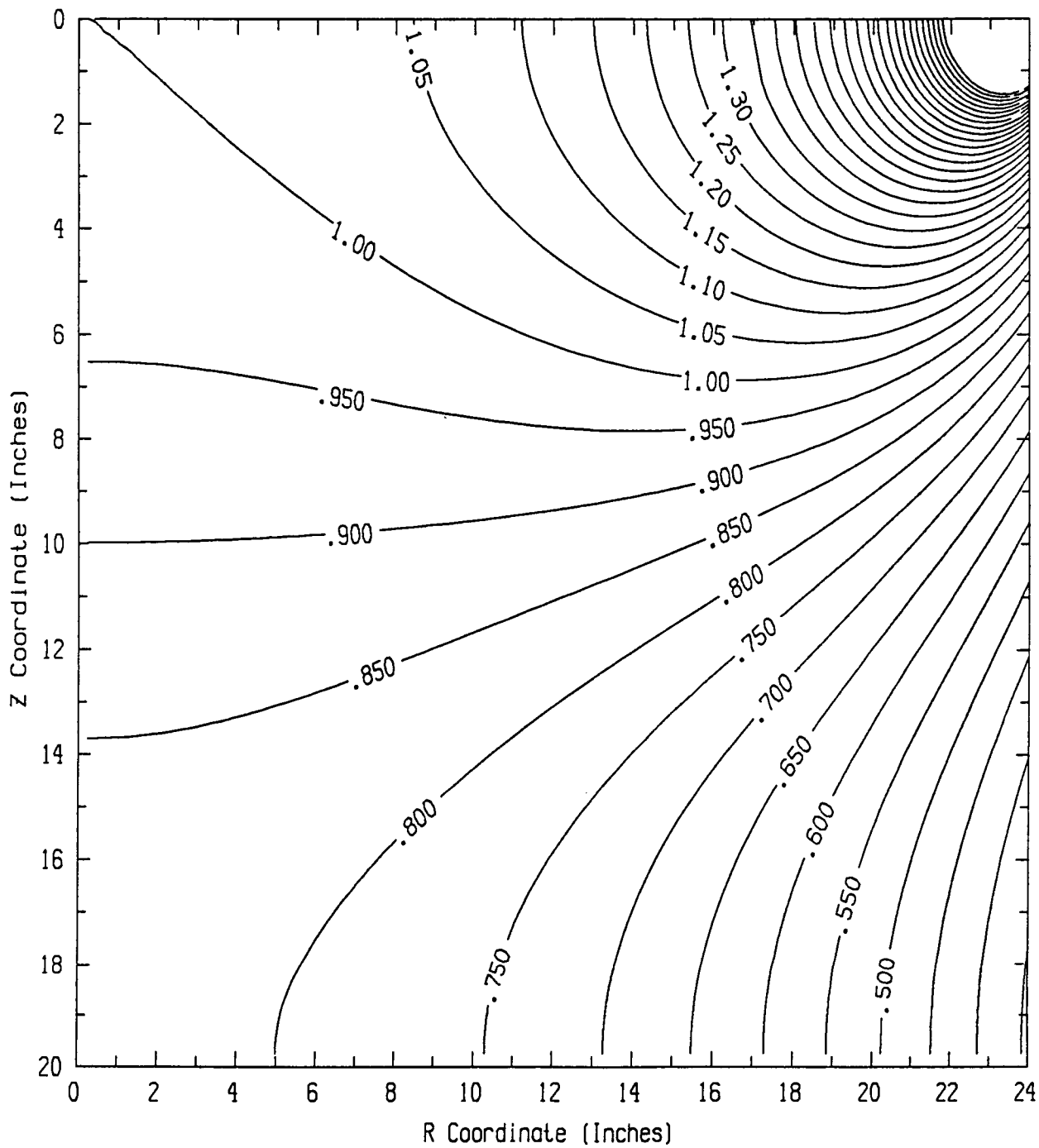


**Figure 2.4(a) Axial Field Mapping for Plates without Guard Rings**

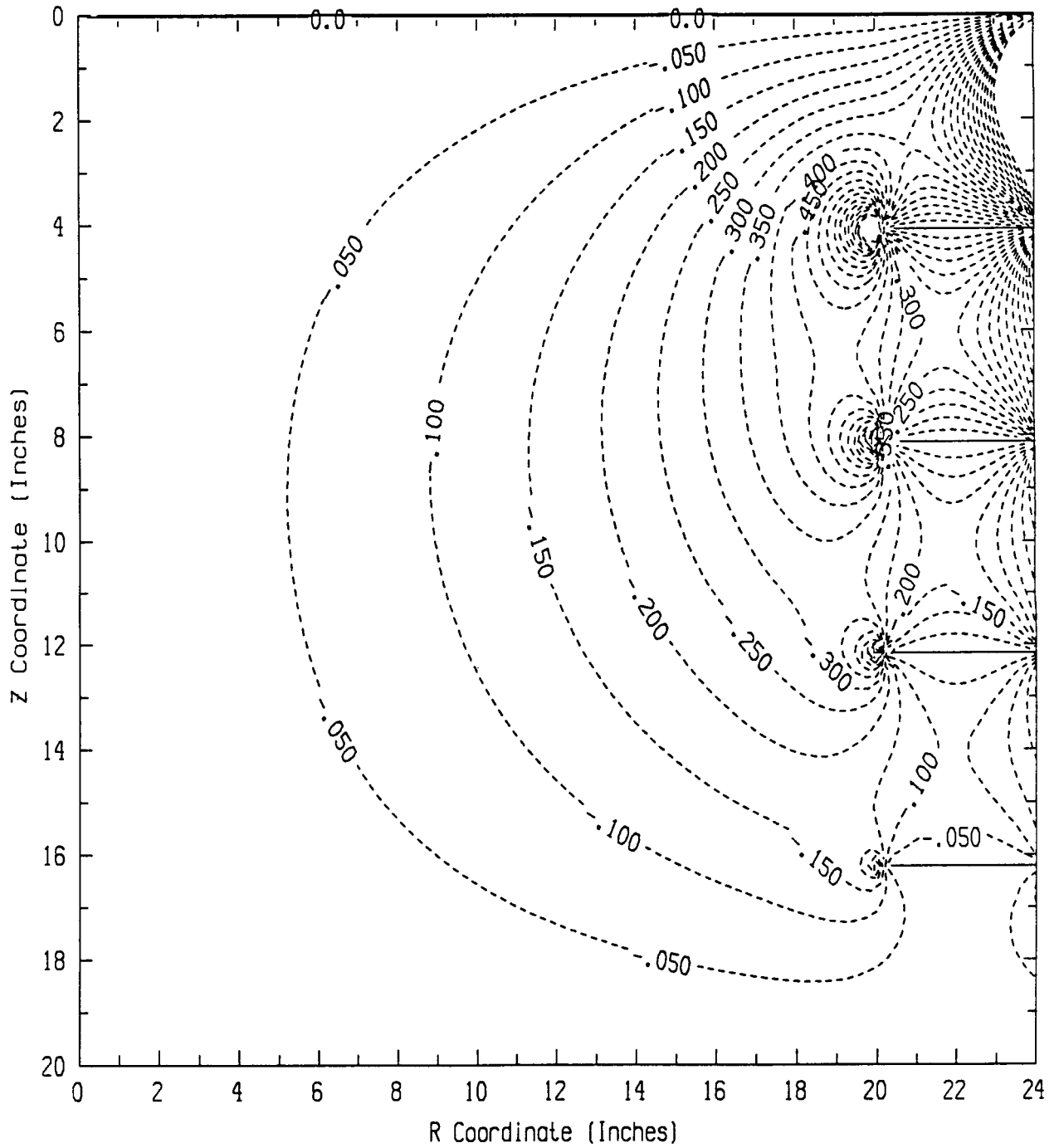


**Figure 2.5(b) Radial Field Mapping for Plates with Guard Rings**

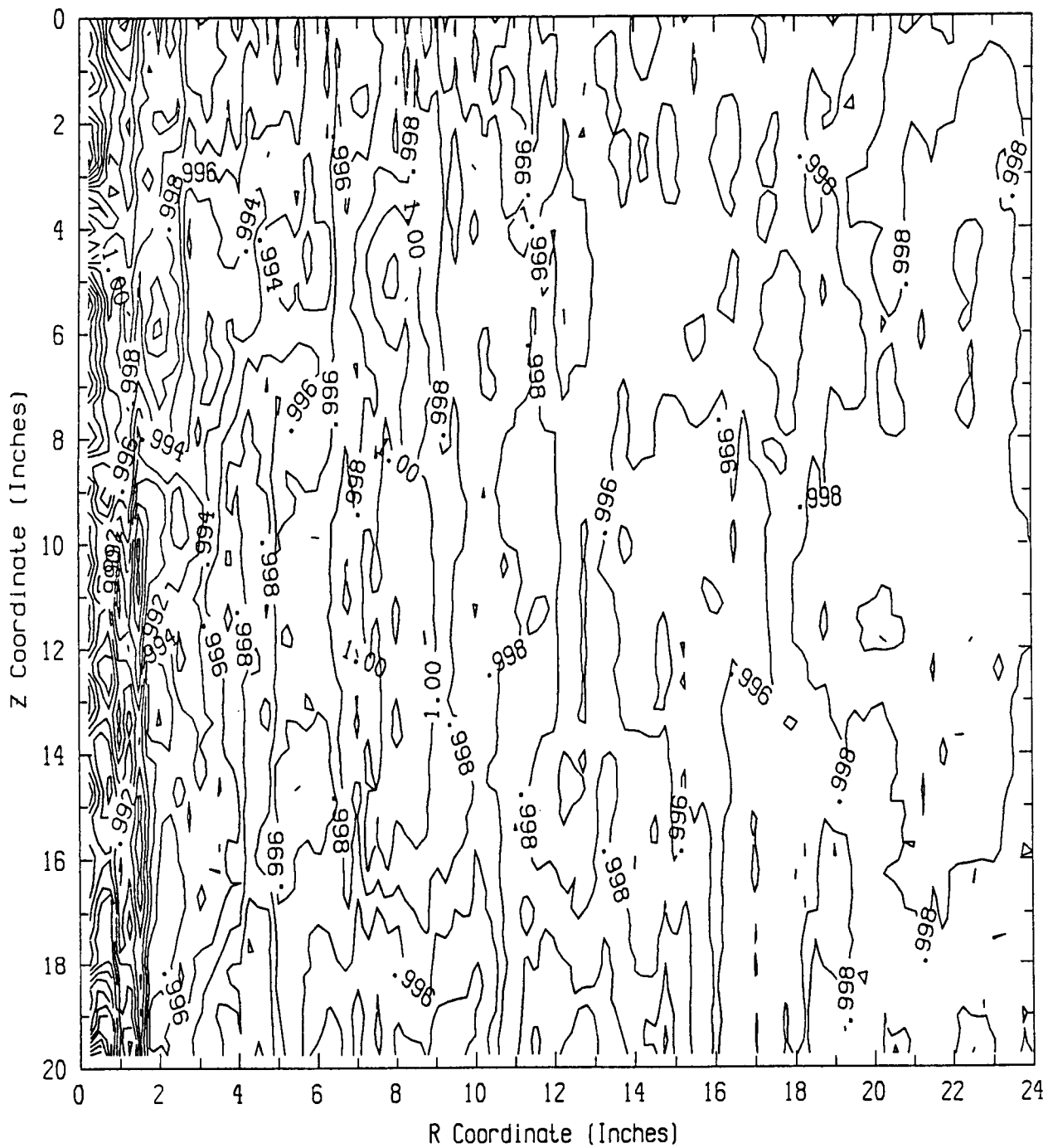


**Figure 2.6(a) Axial Field Mapping for Plates with Guard Rings Connected by Resistors**

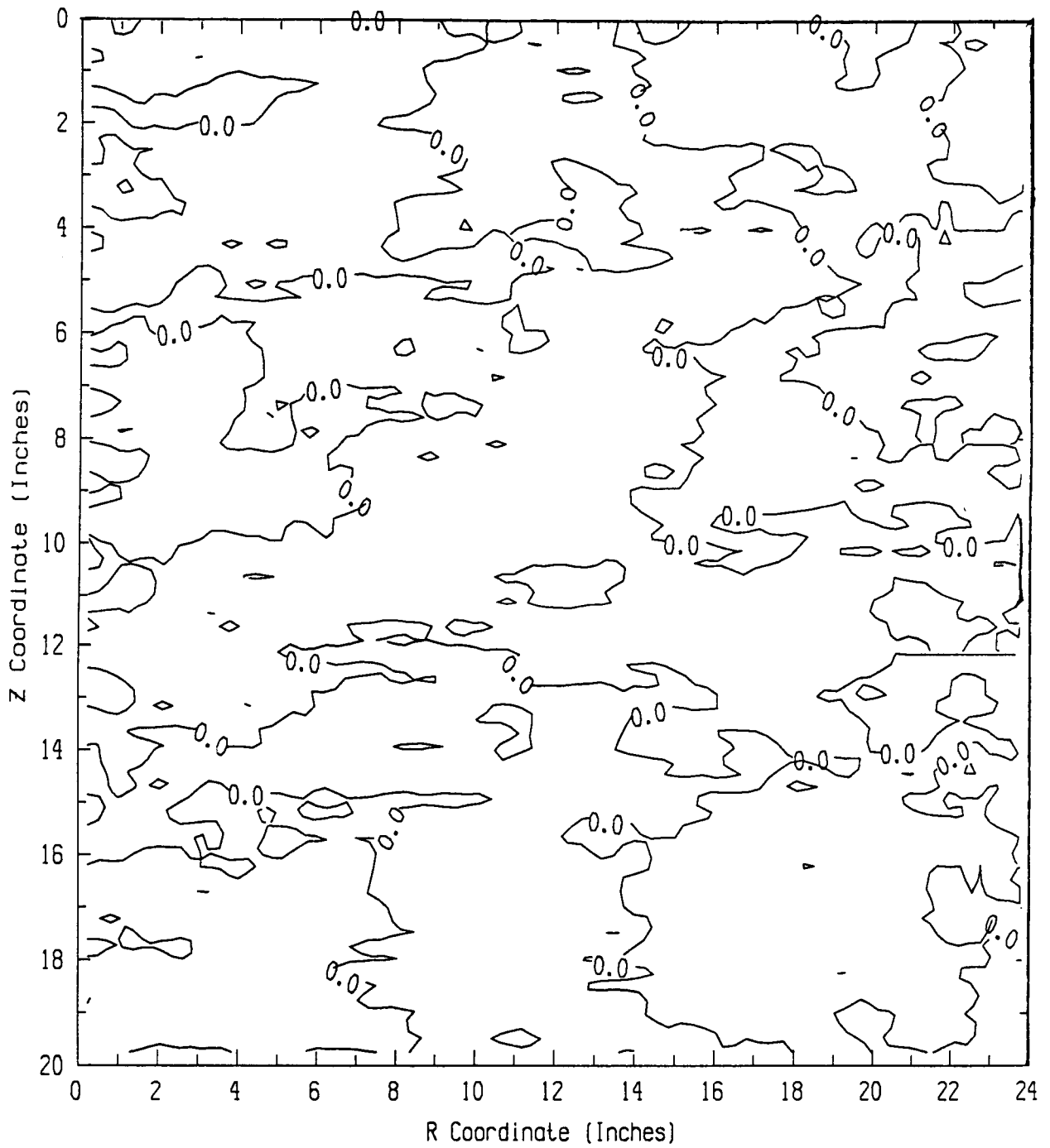


**Figure 2.6(b) Radial Field Mapping for Plates with Guard Rings Connected by Resistors**

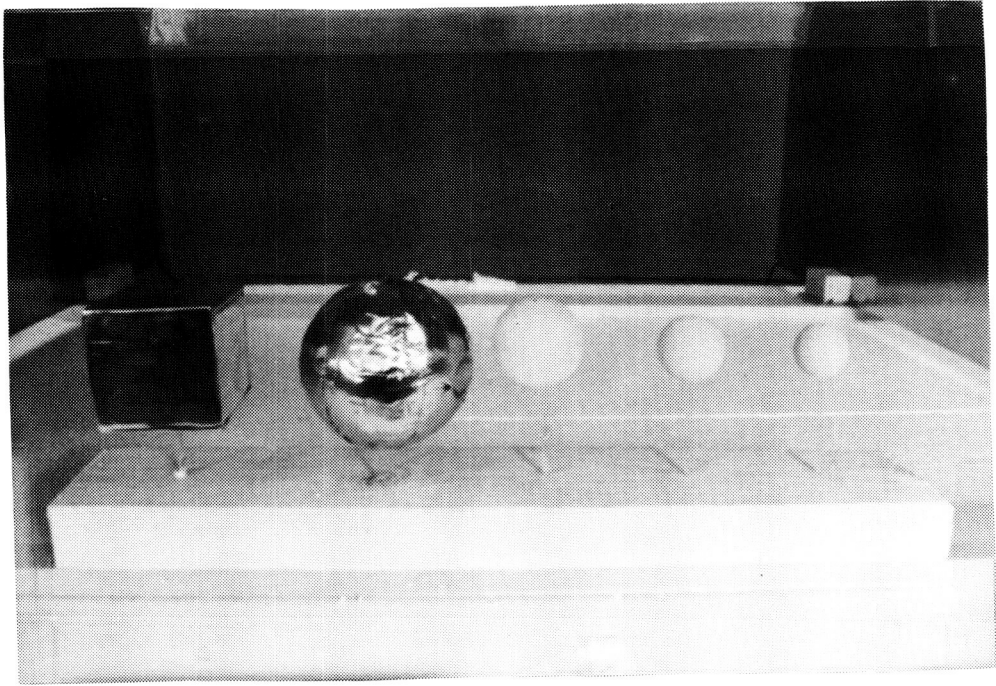
The effect of including guard rings with the plates is shown in Figure 2.5. The field distribution is not significantly changed, and may be slightly more nonuniform. It is necessary to connect the guard rings with large resistances to smooth the field distribution. This ensures that a uniform potential gradient is maintained at the edge of the plates. The large size of the resistors holds the actual current flow from the power source to a small value. The field contours for this situation are shown in Figure 2.6. Although the fields appear chaotic, closer examination reveals that the field magnitude is axial and everywhere nearly the same. It was therefore decided that this guard ring/plate configuration adequately provided the necessary uniform electric field.

Figures 2.7(a) and 2.7(b) show the array of spheres and cylinders as well as the cube utilized in the method evaluation tests. The spheres range in diameter from 1.2 to 3.3 inches while the cylinders range from .88 inches to 3.1 inches in diameter. The cube is 2.5 inches on a side.

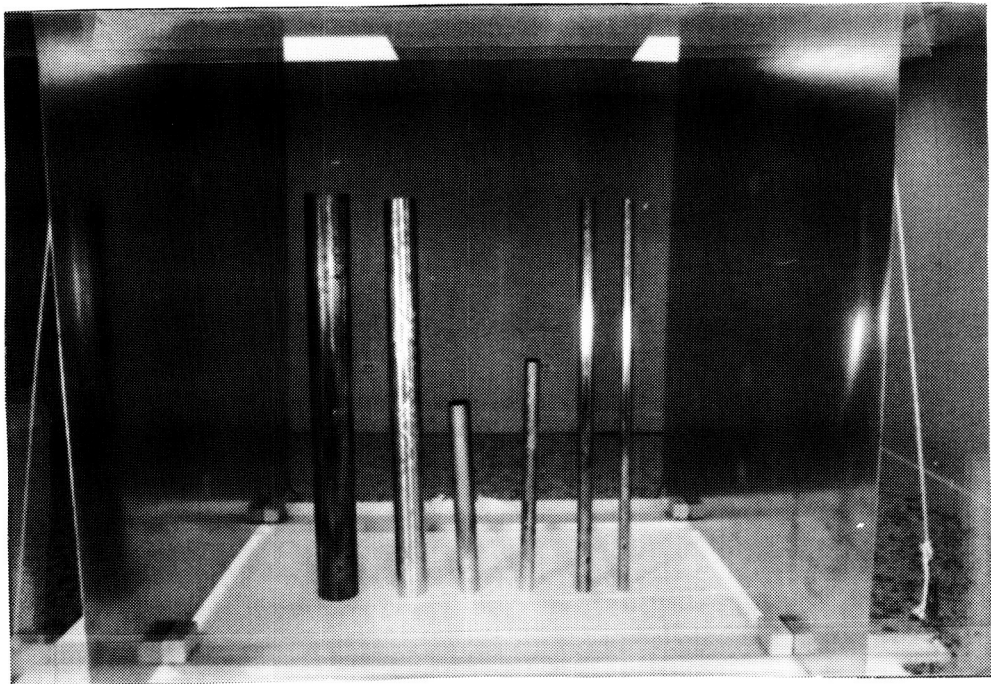
### **2.3. The Charge Measurement Instrumentation**

Initially, Faraday's "ice pail" method was tried as the charge measuring approach. The circuit is shown in Figure 2.8(a). The charge is determined by measuring the capacitive coupling between the charged probe and the surfaces of the "ice pail." However, it was found that this configuration was much too susceptible to external influences such as operator body movements and small charges that occasionally reside on the dielectric parts of the probe. Therefore, a modification was developed as shown in the circuit of 2.8(b). Here, the gallon paint-can (shown in Figure 2.1(b)) provides a grounded shield to the sensing sphere inside the can. In this latter circuit, the measuring probe is inserted through the hole in the outer can and contact is made with the inner copper sphere. Since the input capacitance of the meter and inner sphere is many orders of magnitude larger than the tiny metal sphere of the probe, essentially all of the charge residing on the probe is transferred to the instrument. The Keithley 616 is operated in the "Coulomb" mode (and thus measures the charge transferred directly). The measurement resolution of the system as shown is approximately  $\pm 1 \times 10^{-13}$  Coulombs, and is very stable and noise free.

The probe configuration utilized for the measurements is shown in Figure 2.9. The probe sensor is a 1/8" diameter ball-bearing bonded to a 1/8" diameter lucite

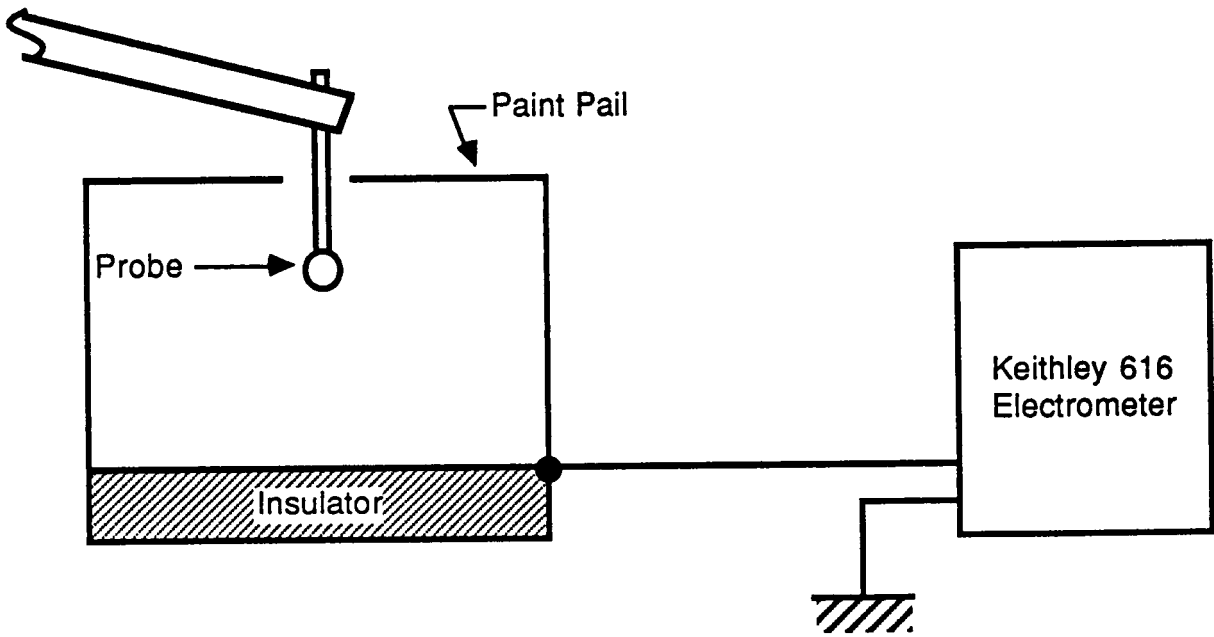


(a) Calibration Spheres and Cube

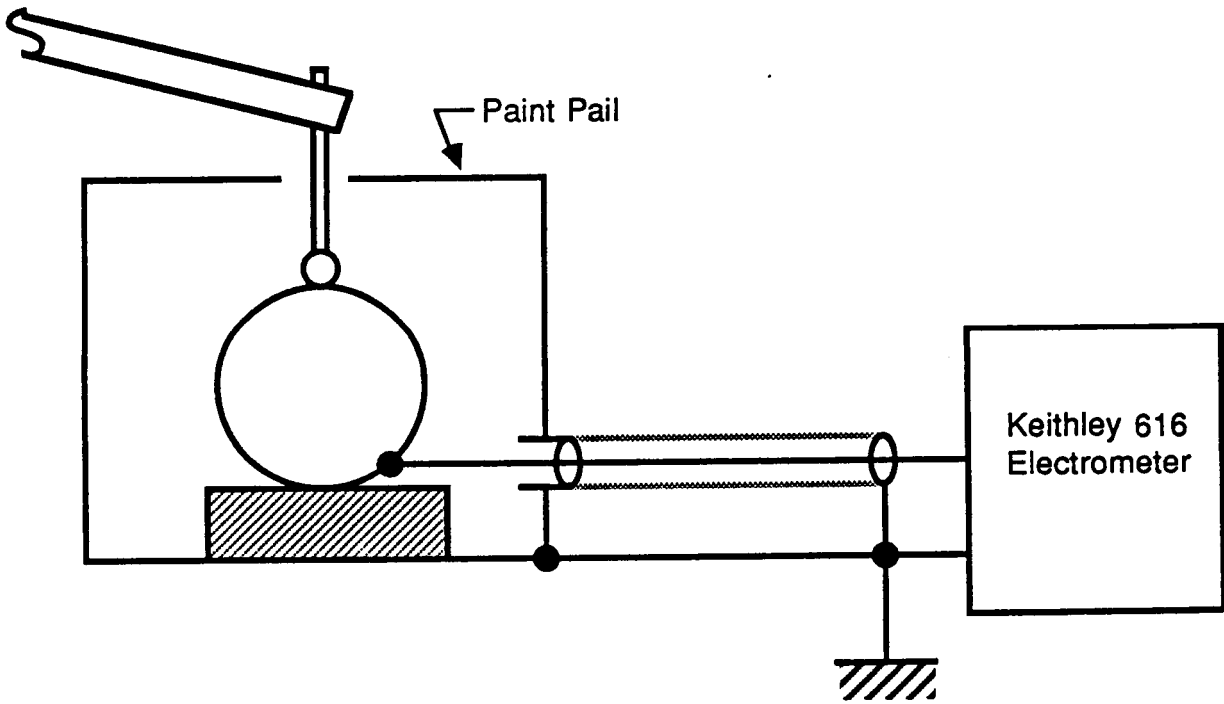


(b) Calibration Cylinders

Figure 2.7 The Calibration Test Articles



(a) Faraday's Method



(b) Test Configuration Used for the Tests

**Figure 2.8 The Charge Measuring Circuits**



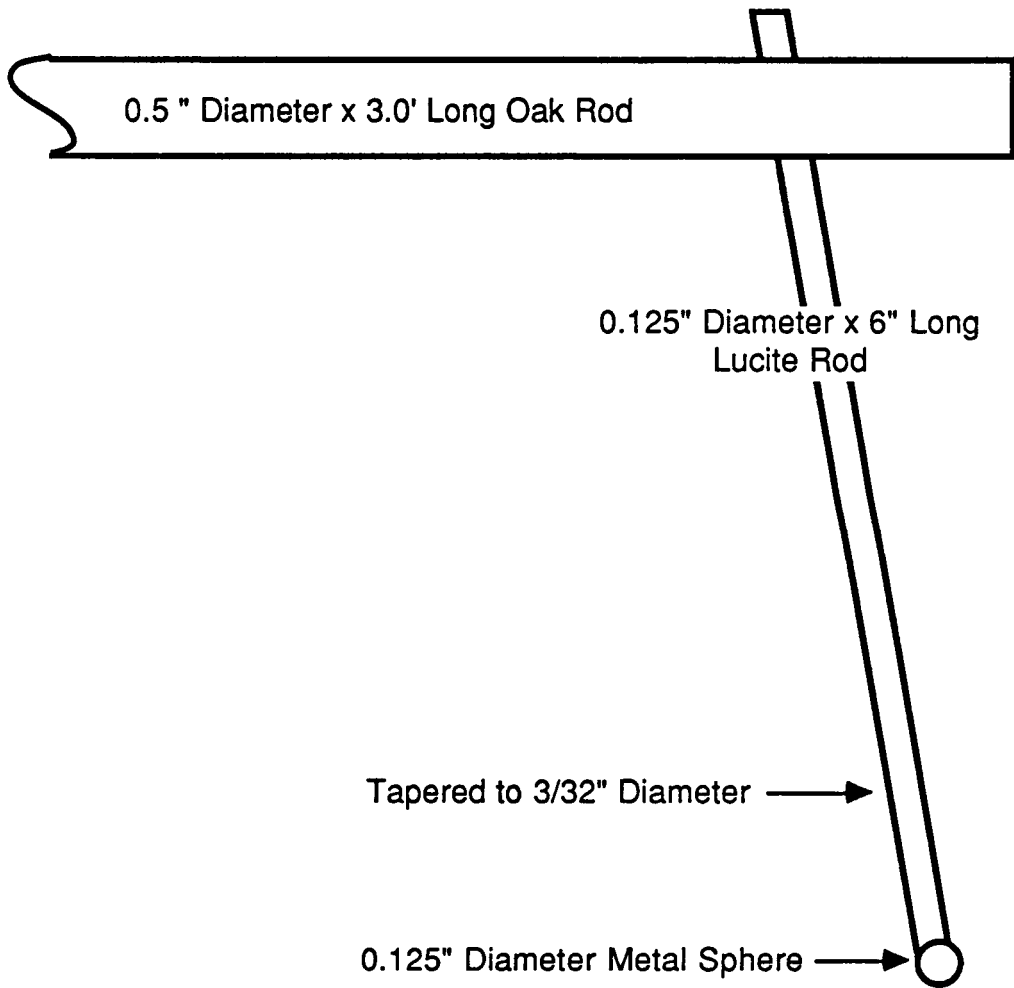


**Figure 2.9 The Charge Transfer Probe Configuration**

rod. The lucite rod is tapered to 3/32" diameter at the tip where it is bonded to the small sphere. The handle for the probe is a 1/2" diameter oak rod approximately 3 feet in length. Other materials such as nylon and teflon were tested as handle material but proved to be no better than the wood. Apparently the lucite rod at the sensor provided all the electrical isolation required for the sensor.

## **2.4 Measurements on Canonical Shapes**

Early in this investigation, it became clear that something was wrong either with the basic assumptions of the method or with the experimental technique being used. Initial measurement of the maximum form factor of a 1 inch diameter sphere was about 2.4 instead of 3.0 and for a long cylinder oriented with axis normal to the field was about 1.5 instead of 2.0. These measurements were made as close as possible to the known analytic locations of maximum field enhancement. At this time, a copper coated B-B shot (diameter .173") was being utilized for the sensing probe.

In order to gain some insight into the reason for the errors in measurement, tests were done with varying sizes of probe spheres against a fixed diameter test sphere of 3.3 inches. Also varying diameters of both spheres and cylinders were sampled with a fixed diameter probe sphere. The results are given in Tables 2.1 - 2.3. The measurements on the spheres and cylinders are shown plotted in Figure 2.10.

The test results indicate that, at least for the large sphere, there is only a very small dependence of the measurements on the probe diameter. However, it is seen that there is considerable variation of the measurements with the diameters of the test spheres and cylinders, especially as the diameters get smaller.

**Table 2.1**  
**Form Factors for Fixed Sphere with Varying Probe**  
**Diameter - Test Sphere Diameter Is 3.3"**

Probe Diameter	Measured Form Factor
.092"	2.68
.125"	2.68
.173"	2.64
.30"	2.63

**Table 2.2**  
**Form Factors for Varying Sphere Diameters But Fixed**  
**Probe (.125" dia.)**

Sphere Diameter	Measured Form Factor
3.3"	2.68
2.0"	2.53
1.5"	2.44
1.2"	2.38

**Table 2.3**  
**Form Factors for Varying Cylinder Diameters but Fixed**  
**Probe (.125" dia.)**  
**Long Cylinders Normal to Field**

Cylinder Diameter	Measured Form Factor
3.1"	1.63
2.5"	1.59
1.6"	1.54
1.1"	1.45
.88"	1.40

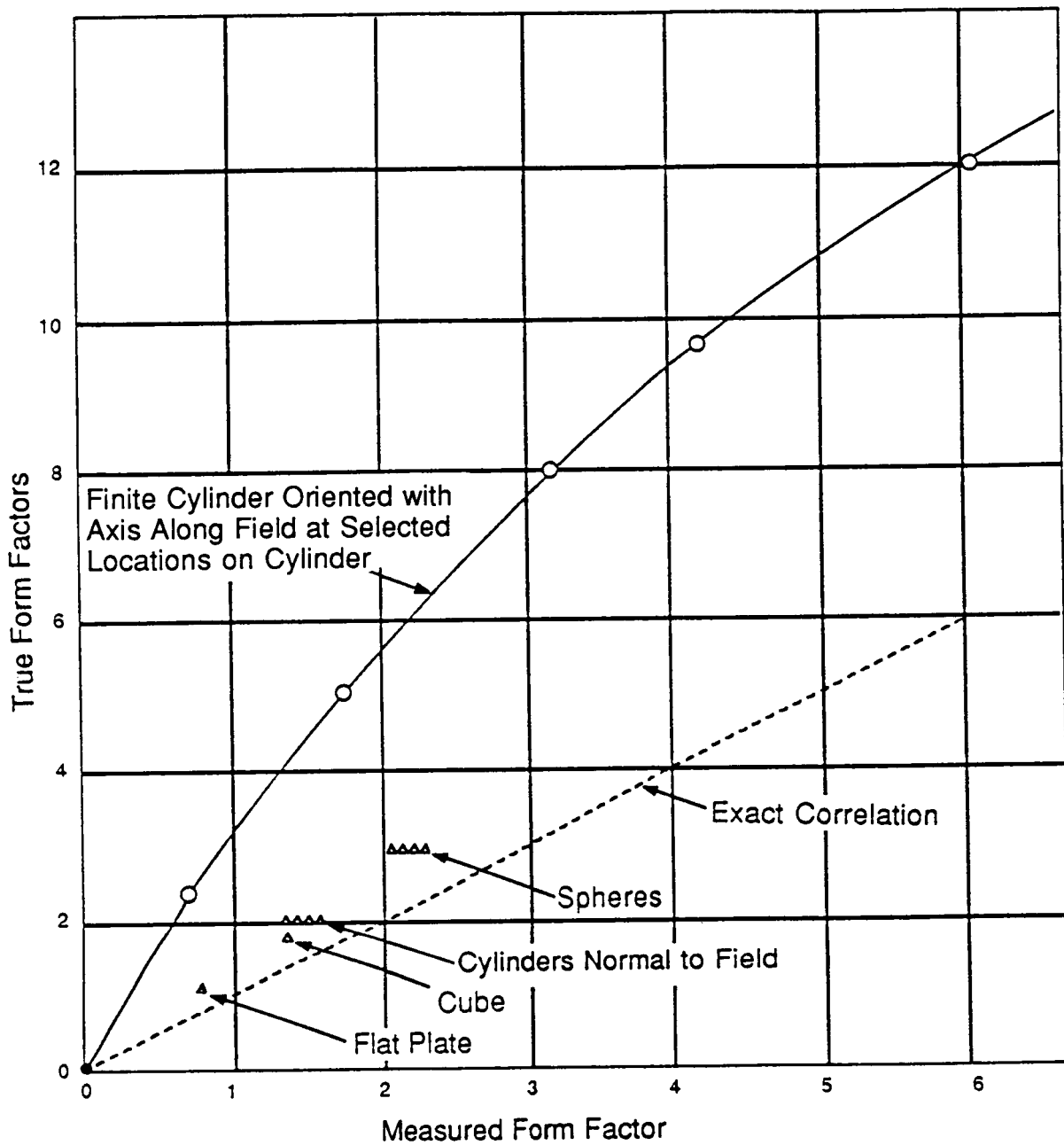


**Figure 2.10** Correlation Between Measurements and Analytical and Finite Difference Solutions for Form Factors

Apparently, the form factor measurements move closer to the theoretical values as the radius of curvature of the test article at the contact point increases.

In order to check the observations more carefully, measurements were made on a limited size flat plate (8" x 8") and a 2.5 inch cube. The flat plate was oriented with its surface normal to the field direction, and the cube with one of its coordinate axes along the field direction. The measurement of the flat plate was made in the center of the face, and for the cube in the center of one of the faces perpendicular to the ambient field. The flat plate measured 0.97 (only a 3% error) and the cube measured 1.63 at the center of the faces normal to the field. A finite difference computation of the form factor of a cube in a uniform field gave a value of 1.7 which indicates an error of about 4% for the measurement.

Further checks of the measurement technique were made utilizing a finite length cylinder (15" long) oriented along the field. This configuration provides a range of form factors from 0 at the center of the cylinder to in excess of 20 at the ends. The cylinder problem was first solved by finite difference methods utilizing a very fine grid (~ 1/32"). These results are shown in the first column of Table 2.4. The second column of the table shows the same solution utilizing a 1/4" grid. Both these cases were run with an idealized uniform ambient field. Note the large degradation of the computed values when a larger grid spacing is used. The third column in the table shows the results of the finite difference analysis where the test geometry is introduced (i.e., the end plates and the guard rings). Obviously the plates and guard rings are not reproducing the uniform field exactly. However, the deviations are not large and are not the main source of the error.

**Table 2.4**  
**Computations and Measurements of the Form Factors Along the Axis of a**  
**Finite Cylinder Oriented Parallel to the Electric Field**

Distance from End (Inches)	Finite Difference Solutions		Plates & Guard Rings In place - 1/4" Grid	Measurements .125" prob dia.
	1/32" grid	1/4" grid		
.25	12.79	8.17	7.36	7.1
.50	11.11	6.44	5.79	5.54
1.0	9.75	4.9	4.39	4.23
2.0	8.13	3.55	3.16	3.06
4.0	5.17	2.06	1.80	1.80
6.0	2.22	0.89	0.77	0.74
7.5	0	0	0	0

The last column in Table 2.4 shows the measured values of form factors along the cylinder using the .125 inch diameter probe. Note that these measurements agree quite well with computations made by modeling the measurement geometry with a 1/4" grid (a smaller grid was not possible for this model because of the small time step involved and the resulting increase in computing time).

The results of the analysis and measurements of the finite cylinder indicate clearly that the measurement technique is far from accurate. Errors range from 45% near the ends to 300% near the center of the cylinder. A correlation plot of all the computed and measured form factors obtained during the study are shown in Figure 2.10. Note that the correlation curve for the cylinder oriented along the field is considerably different than for the spheres and cylinders oriented normal to the field. It was originally thought that a universal correlation curve could be found that would permit translating measured form factor values to actual values. However, it is seen from Figure 2.10 that the uncertainty factor is large, even for the simple geometries tested. In other words, the charge transferred to a small metal probe touched to a conductive object immersed in an ambient field depends not only on the shape and size of the probe and the magnitude of the ambient field but it also depends in a complex way on the local distribution of the field at the contact points.

## 2.5 Some Theoretical Support for the Measurement Anomalies

Hara and Akayaki [7] have solved the problem of the small sphere in contact with a flat plate in a uniform field. The charge transfer to the sphere is given by:

$$\Delta q = k\epsilon_0 E r^2 \quad (2.1)$$

where  $r$  = radius of small sphere  
 $E$  = ambient uniform field  
 $k$  = constant.

Note that the charge transferred is a function of the radius of the small sphere and the field only. This is the condition required for the experimental method being investigated to be valid. However, another interesting problem has been analyzed that shows the experimental method to be invalid. This is the problem of two spheres brought into contact in a uniform field [8]. Here the charge transferred to a small sphere from a larger sphere is given by

$$\Delta q = \gamma\epsilon_0 E r^2 \quad (2.2)$$

where  $r$  = radius of small sphere  
 $E$  = ambient electric field  
 $\gamma$  = parameter which is a function of  $r/R$ , where  $R$  is the radius of the large sphere.

The parameter  $\gamma$  was computed for a number of values of  $r/R$ . It was shown that when  $r/R$  approached zero,  $\gamma$  approached a constant as in equation (2.1). Thus the two solutions agree in the limiting case of the sphere and the flat plate.

The analytical results for the case of spheres clearly shows that the experimental method is not valid for the simple case of a sphere, since the charge transferred will vary with the radius of the sphere being measured whereas the form factor of a sphere is independent of its radius. It follows that if the experimental method is not valid for spheres, it is not likely to be valid for complex shapes with large aspect ratios and multiple curvatures.

## 2.6 Measurements on the F106B Scale Model

While it was known that the experimental method being utilized was not universally valid, measurements were made on the model aircraft anyway in order to obtain data for comparison with the earlier estimates of the form factors generated by finite difference analysis. Fourteen different points on the aircraft were measured including the three positions where the field meters are located on the real aircraft. The locations of the test points are shown in Figures 2.11, 2.12 and 2.13.

The results of the measurements and some rough estimates of adjusted values are given in Table 2.5. The adjusted values can only be very approximate since they were obtained by estimating the test point locations as they compared with the data given in Figure 2.10. These numbers may not be any more accurate than the original measurements. They are included to give the reader some feel for the likely errors in the measurements. The three points representing the actual locations of the field meters are identified by an asterisk.

**Table 2.5**  
**Form Factor Measurements and Corrected Estimates**  
**for Points on the F106B**

Aircraft Test Points	Measurements			Adjusted Measurements		
	K <sub>x</sub>	K <sub>y</sub>	K <sub>z</sub>	K <sub>x</sub>	K <sub>y</sub>	K <sub>z</sub>
* 1	4.8	1.4	0.8	10.6	2.6	1.0
3	5.3	0	1.9	11.2	0	2.3
* 4	3.1	0	1.7	8.0	0	2.0
5	3.8	0	2.4	9.2	0	3.2
6	1.3	0	2.2	4.2	0	2.8
7	0.3	0.5	1.2	1.0	0.6	1.4
9	0.2	0.7	0.7	0.6	1.3	0.8
10	2.2	4.4	0.8	6.2	8.6	0.9
11	0.5	0.5	0.4	1.2	0.6	0.4
12	6.2	0.9	4.8	12.2	1.6	7.6
* 13	0.5	0.2	1.4	1.2	0.3	1.8
14	0.5	1.0	1.0	1.2	1.8	1.1



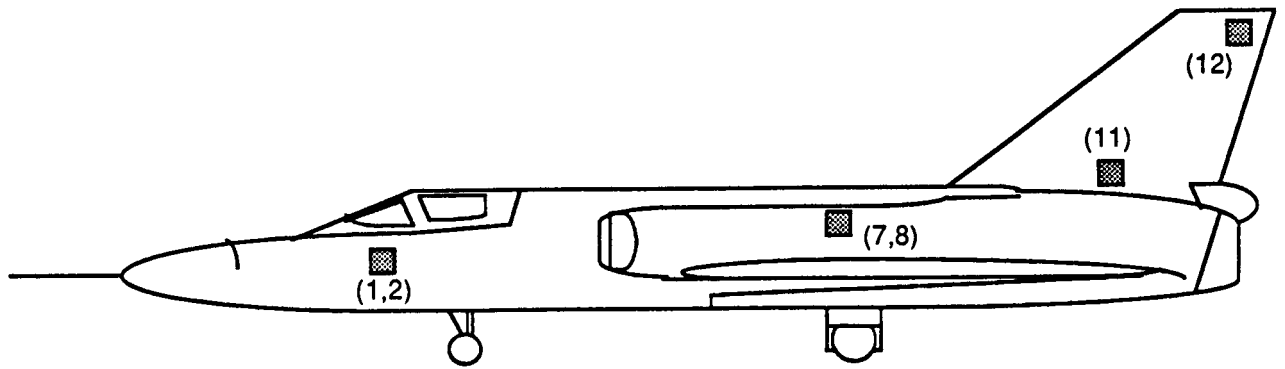


**Figure 2.11 Side View of F106B Showing Test Point Locations**

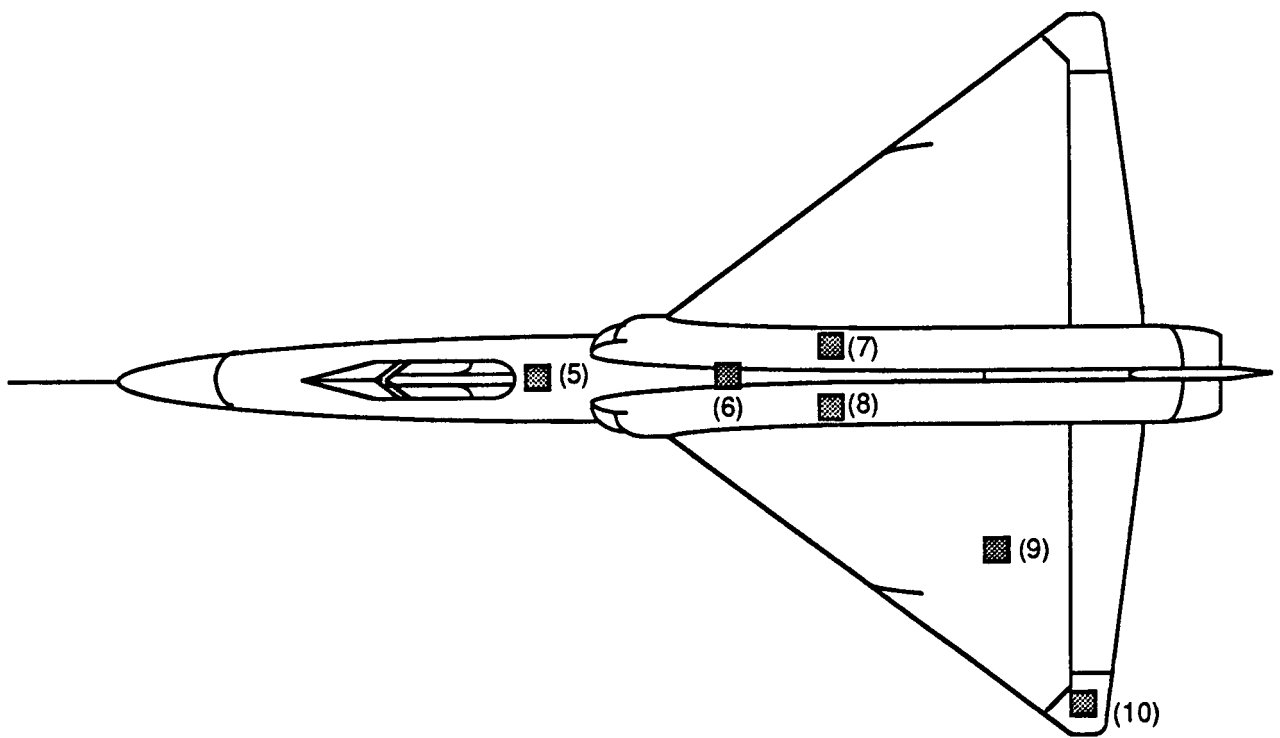


**Figure 2.12 Top View of F106B Showing Test Point Locations**

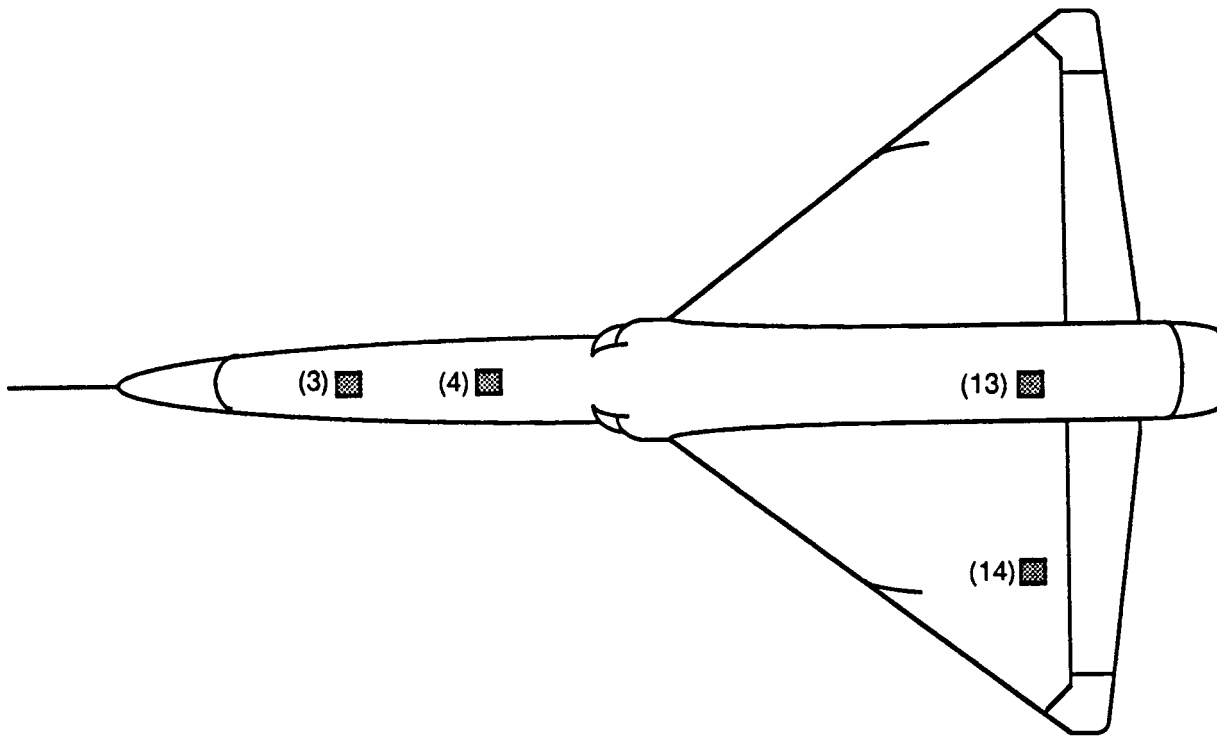


**Figure 2.13 Bottom View of F106B Showing Test Point Locations**

Table 2.6 shows a comparison of the computed values obtained by finite difference analysis, the actual measured values and the adjusted values. Note that the measured values compare quite well with the computed values. It is believed that this result is obtained because both methods suffer from a similar problem, i.e., both methods produce a value that is averaged over a volume in which the field can vary a great deal. As a result, the perceived form factors are different than actual, especially where they are much larger than unity.

The estimated corrections in Table 2.6 are given primarily to indicate that there may well be large errors in the values now being used, especially the values for  $K_{1x}$  and  $K_{3x}$ .

**Table 2.6**  
**Comparisons of the Form Factors Obtained by Direct Measurement,**  
**by Finite Difference Analysis, and by Adjusting the Measured Values**  
**According to Correlation Data**

Points	Measurements			Finite Difference Estimates			Adjusted Measurements		
	$K_x$	$K_y$	$K_z$	$K_x$	$K_y$	$K_z$	$K_x$	$K_y$	$K_z$
E <sub>1</sub>	4.8	1.4	0.8	4.38	1.46	0.08	10.6	2.6	1.0
E <sub>3</sub>	3.11	0	1.7	2.47	0	1.52	8.0	0	2.0
E <sub>4</sub>	0.5	0.2	1.4	0.89	0.15	1.03	1.2	0.3	1.8

## 2.7 Conclusions

It has been found that the experimental method for measuring form factors utilizing a small scale model immersed in a field and a tiny metal probe has serious difficulties. The problems apparently stem from the similarity between the scale of the field variations near the skin of the model and the size of the small metal probe.

Indications are that if the aircraft model were made very large and the probe kept very small, the accuracy of the measurements might be acceptable. However, this action would defeat the purpose of the technique which was to facilitate the calibration of field meters in a small laboratory environment.

## CHAPTER 3

### LIGHTNING CHANNEL MODELING

#### 3.1 Introduction

Lightning discharges that attach to the F106 aircraft often show a large number of pulses occurring in the range of several microseconds to tens of milliseconds or even hundreds of milliseconds following the initial attachment. The number of pulses following the initial discharge varies considerably from flash to flash. A crude visual count of the F106 analog data for the year 1984 shows an average repetition rate of about 250 pulses per second. This rate is undoubtedly the lower limit to the true rate since the data used are mostly in the form of low resolution 25 cm/sec records. The better resolution 50 cm/sec records, where available, invariably show a larger number of pulses in the same time interval. Indeed a higher rate of 1000 pulses per second has been reported for a lightning strike on the CV-580 aircraft [9]. These pulses are probably due to the discharging of charge clusters in the cloud by the leader of a lengthening lightning channel. This would explain the variable pulse repetition rate and the time delay between consecutive pulses. An efficient lightning channel model is desirable for a better understanding of this phenomenon.

#### 3.2 Equations Describing the Channel

The formation and propagation of a lightning channel is a complex phenomenon. Many physical processes are involved in the formation of the channel. While there are many theoretical models to describe individual stages of channel formation, there is presently no model to predict the whole event starting from the inception of corona discharge to the highly conducting channel.

An electrical corona model has been quite successful in modeling the first microsecond of a triggered lightning strikes to aircraft [2,3]. The emphasis in the application of the model so far has been on the initiation and early time interaction of the corona discharge with the aircraft. As a fully three dimensional model with a rather elaborate set of fluid equations the existing corona model is not appropriate for channel modeling because of its great demand on computer resources. This chapter reports on the modification of the corona model to study the characteristics of a leader

channel propagating away from the aircraft. This entails extending the analysis to cover times greater than a microsecond and distances greater than a few meters from the aircraft. An obvious simplification is to assume azimuthal symmetry so that a two dimensional model is applicable. Another area of possible simplification is in the way the conductivities of the cells are calculated. For channel modeling it is reasonable to assume that the conductivity of air away from the channel is low and that its variation in time can be neglected. With this assumption only the conductivities of the cells forming the channel need to be calculated. With a two dimensional model the lightning channel is predetermined to be along the z-axis of an r-z coordinate system. The conductivities of these cells are calculated from the charged particle densities and mobilities. The use of the fluid conservation equations for mass, momentum and energy in the calculation of air conductivity has been described in previous reports [2,3]. In the present model the equations for the conservation of momentum are not used. Instead the fluid velocities of the charged particles are calculated as the product of the respective mobility and electric field,  $\vec{V}_s = \pm \mu_s \vec{E}$ . Here the s subscript represents species type, and can be e, +, or -. In the model only motion along the z-axis (channel) is considered. A new feature in the present model is the inclusion of the vibrational energy reservoir for the neutrals. This and other additional features are further explained in the following.

The rate equations for the particle densities are:

$$\begin{aligned}
 \frac{\partial n_e}{\partial t} + \nabla \cdot (n_e \vec{V}_e) &= Q + G n_e - \alpha_e n_e - \beta n_e n_+ + \alpha_d n_- \\
 \frac{\partial n_+}{\partial t} + \nabla \cdot (n_+ \vec{V}_+) &= Q + G n_e - \beta n_e n_+ - \gamma n_- n_+ \\
 \frac{\partial n_-}{\partial t} + \nabla \cdot (n_- \vec{V}_-) &= \alpha_e n_e - \gamma n_- n_+ - \alpha_d n_- \\
 \frac{\partial n_n}{\partial t} &= -G n_e + \alpha_d n_- + 2\gamma n_+ n_- + \beta n_e n_+ - \alpha_e n_e
 \end{aligned} \tag{3.1}$$

where  $G$  = is the avalanche rate [2,3,10],  
 $\alpha_e$  = the electron attachment rate [2],  
 $\beta$  = the electron-ion recombination coefficient [11],  
 $\gamma$  = the ion-ion recombination coefficient [2],  
 $\alpha_d$  = the detachment rate [11] and  
 $Q$  = the ambient ionization rate due to cosmic rays [2].

The detachment rate is a strong function of the ionic temperature and humidity. It is insignificant for ionic temperature lower than 1000° K. For an ionic temperature of 2000° K, the detachment lifetime of  $O_2$  is about 31 nanoseconds. For a humidity of 4 gram/m<sup>3</sup>, the detachment lifetime increases rapidly to microseconds for secondary types like  $O_2$ -  $H_2O$ . The other coefficients in the rate equations have been discussed in detail in the previous reports. The equation for the neutrals is included to handle the situation of a fully ionized gas. However it never needs to be solved. The neutral density can be obtained simply from the charged particle densities, the conservation of mass and the assumption of singly ionized ions. As mentioned earlier, the fluid velocities,  $V_s$ , of the charged particles are calculated from the mobility,  $\mu_s$ , by  $\vec{V}_s = \pm \mu_s \vec{E}$ , where  $s$  stands for species (e,+, -). The mobilities are given by

$$\mu_e = \frac{q_e}{m_e(v_{en} + v_{e+})} \quad (3.2)$$

$$\mu_{\pm} = \frac{2.5 \times 10^{-4}}{\rho_r}$$

where  $v_{en}$  = is the collision frequency for momentum transfer between electrons and neutral molecules [12];  
 $v_{e+}$  = is the momentum transfer frequency for electron-ion collisions [11],  
 $\rho_r$  = the relative air density,  
 $q_e$  = the electronic charge.  
 $\mu_e, \mu_+, \mu_-$  = mobilities.

Through elastic and inelastic collisions, energy is transferred from the electrons to the neutral molecules and ions. The energy transferred to the neutrals is used in the ionization or dissociation of the molecules, in increasing the translational energy or in the excitation of the electronic, rotational or vibrational energy states of the molecules. The relaxation of the rotational energy states is fast. Therefore the energy released in their relaxation can be combined with the gain in the translational energy to increase directly the temperature of the neutrals. In contrast the relaxation time of the vibrational states is relatively slow. Therefore a separate conservation equation for the vibrational energy reservoir,  $W_v$ , with a temperature of  $T_v$  is used in the model. The ion and neutral energy equations are combined. This can be done because both the ions and neutrals are approximately at the same temperature due to strong coupling from collisions. The full set of energy density equations is then:

$$\begin{aligned} \frac{\partial \epsilon_e}{\partial t} + \vec{V}_e \cdot \nabla \epsilon_e = q_e n_e \vec{E} \cdot \vec{V}_e - G n_e \epsilon_{ion} - (\alpha_e + \beta n_+) \epsilon_e \\ + \epsilon_q + \alpha_d n_- T_n - C_{en} - C_{e+} \end{aligned} \quad (3.3a)$$

$$\begin{aligned} \frac{\partial \epsilon_n}{\partial t} = q_+(n_+ + n_-) \vec{E} \cdot \vec{V}_+ + (1 - f_v) C_{en} + C_{e+} \\ + \frac{W_v(T_v) - W_v(T_n)}{\tau_{vt}} \end{aligned} \quad (3.3b)$$

$$\frac{dW_v}{dt} = f_v C_{en} - \frac{W_v(T_v) - W_v(T_n)}{\tau_{vt}} \quad (3.3c)$$

In these equations,  $\epsilon_{ion}$  is the ionization energy of a neutral molecule [2]. The temperature for a given species is simply defined by  $\epsilon = nkT$ , where  $k$  is the Boltzmann constant. The rate of energy exchange between electrons and neutrals is

$$C_{en} = n_- v_{en} k(T_e - T_n) \quad (3.4)$$



where  $\nu_{en}$  is the electron-neutral energy exchange collision frequency [12]. The excitation of vibrational energy states of the neutral molecules provides an efficient path for the transfer of energy from the electrons to the much heavier neutrals. Because of this transfer the temperature of the electron fluid is limited to less than  $25,000^\circ$  K when the neutral temperature is low compared to that of the electron. The rate of energy exchange between electrons and ions through coulomb collisions is

$$C_{e+} = n_e^3 \frac{m_e}{m_+} \nu_{e+} k(T_e - T_n). \quad (3.5)$$

Thus in the electron energy density equation (Equation 3.3a) the first term on the right is energy gained from the ambient electric field. The second term is the energy lost in ionizing collisions. The third term is the energy lost in attachment and recombination. The fourth term is the energy gained from ambient ionization due to cosmic rays. The fifth term is the energy gained from detachment, assuming the freed electrons are at the ionic temperature. The last two terms are the energy exchanged between electrons and the heavy particles in nonionizing collisions. The energy density stored in the vibrational reservoir of the neutrals is

$$W_v(T_v) = \frac{n_n \epsilon_v}{e^{\epsilon_v/kT_v} - 1} \quad (3.6)$$

where  $\epsilon_v$  is the average vibrational energy level. It is taken to be equal to the energy of the first excited vibrational state of nitrogen molecule,  $\epsilon_v = 0.28\text{eV}$  [11]. In the equations for the energy balance for the heavy particles and the vibrational energy reservoir,  $f_v$  is the fraction of the energy transfer in electron-neutral collisions that goes into the excitation of the vibrational states. For a reduced field,  $E/n_n$ , of less than  $5 \times 10^{-19} \text{ VM}^2$ ,  $f_v$  is larger than 0.75 [11]. Therefore for lightning strike environments most of the energy goes into the excitation of the vibrational states.  $\tau_{vt}$  is the vibrational relaxation time. It is a function of the neutral temperature and humidity. For a neutral temperature of  $1000^\circ$  K,  $\tau_{vt}$  is about 40 microseconds and increases rapidly as the temperature drops. It is 200 microseconds for a temperature of  $400^\circ$  K [11]. Thus the transfer of the vibrational energy to the translational energy is rather slow at low temperature. There are other energy reservoirs which are not included in the

energy equations. Among them is the radiation energy of the photons, which may be important in the propagation of a lightning channel via photoionization at the head of the leader channel.

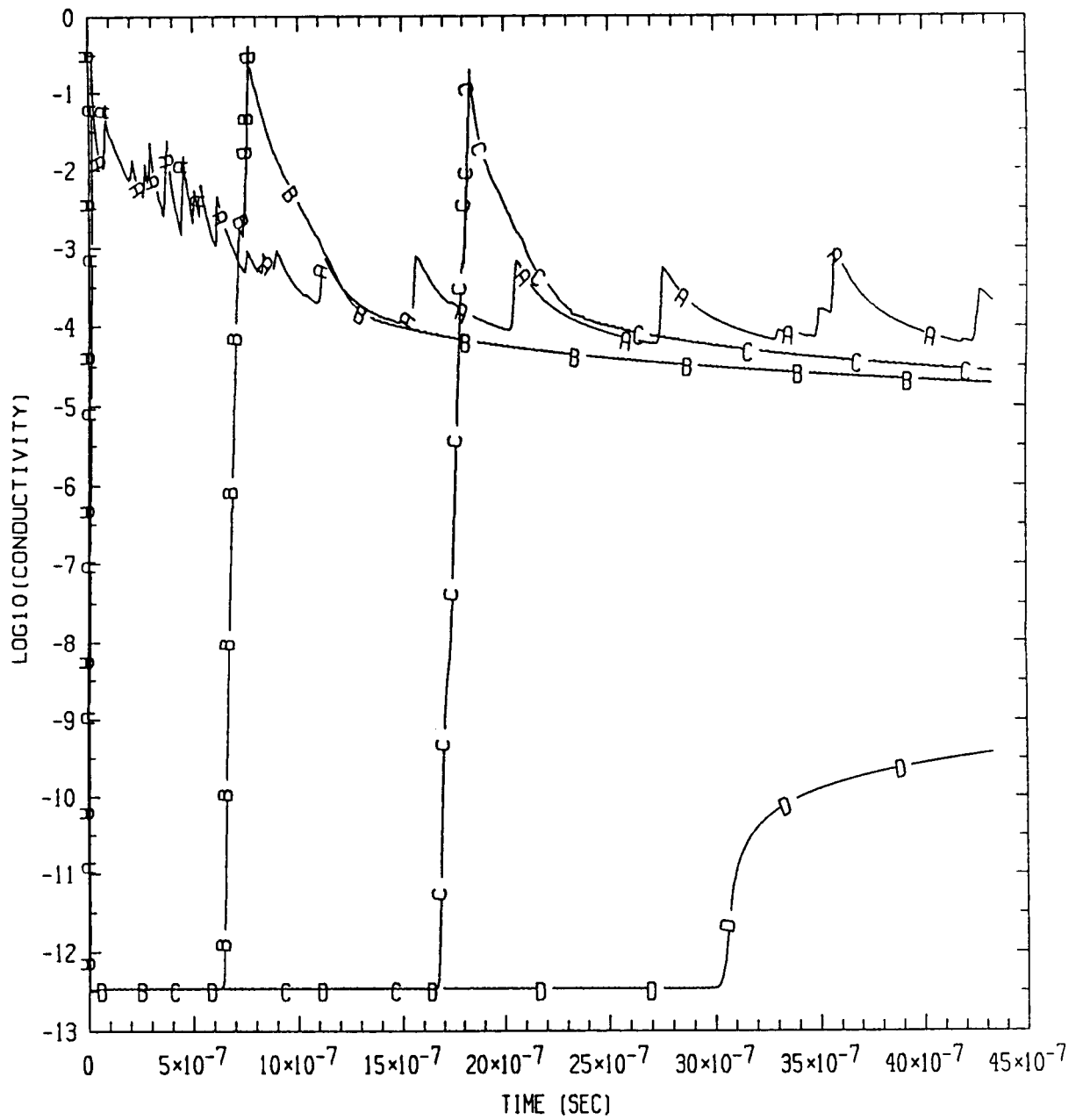
In the solution of the conservation equations, the functional dependence and the values of the rate coefficients are taken from the references cited. They are in the form of curve fitted expressions, graphs or tables. These data are usually measured in conditions which are not those found in a lightning environment. Nevertheless for lack of better data they are assumed to be applicable to the study of air breakdown. From the densities and mobilities of the particles the conductivity for each cell in the finite difference grid can be calculated from

$$\sigma = q(n_e \mu_e + (n_+ + n_-) \mu_i) . \quad (3.7)$$

### 3.3 Results

The model has been utilized to examine the propagation of a triggered lightning leader from an airplane. The problem space dimensions are 400 meters in the z-direction with a resolution of 2 meters, and 150 meters in the radial direction with a resolution of 3 meters. In the two dimensional model the gridding for the nose of the aircraft is a tapered rod along the z-axis. For the results presented, a 12-cell cylinder with zero resistance is used to model the aircraft. The relative air density used is 0.5. The initial temperature is 300° K.

For an ambient field of 0.45 MV/m, the conductivity of the leader channel at selected distances from the aircraft is shown in Figure 3.1. The variation of the conductivity of the cell 2 meters from the aircraft as a function of time is shown in curve A of Figure 3.1. Similarly curves B,C, and D show the conductivities of the cells at distances of 42 m, 82 m and 112 m from the aircraft respectively. It is seen that air breakdown in the cell at a distance of 42 m away from the aircraft (curve B) occurs more than .6 microseconds later than that near the nose. The occurrence of air breakdown 3 microseconds later at a distance of 112 m from the aircraft is shown by curve D. Thus Figure 3.1 clearly shows the formation and propagation of the leader channel away from the aircraft. For a given cell the conductivity increases very rapidly at the onset of the breakdown and then decreases gradually as the high breakdown



DISTANCE FROM PLANE: A=2M  
 B=42M  
 C=82M  
 D=112M

Figure 3.1 Air Conductivity at Selected Distances from the Aircraft

field passes on to the next cell in front of the leader tip. The breakdown field is propagated forward due to a highly conducting channel behind the tip. As the conductivity of the channel decreases due to the attachment of the electrons the field at the tip of the channel decreases until it becomes less than the breakdown field strength whereupon the propagation of the channel is terminated. Thus in this model the conductivity of the channel determines the propagation of the channel. The conductivity of the channel and hence the length of the channel is strongly dependent on the ambient field. For this particular run, with an ambient field of 0.45 MV/m, the length of the leader channel is about 112 meters. The corresponding channel lengths are 10 m and 35 m for ambient fields of 0.25 and 0.35 MV/m respectively. For an ambient field of 0.5 MV/m the leader channel reaches the problem space boundary and presumably would be able to reach the charge centers that produced the ambient field. This result is consistent with observations showing maximum measured thunderstorm fields of about 0.4 MV/m. Fields greater than this value would not exist because of corona growth around thunderstorm particles.

An interesting feature of the leader channel is the pulses that originate from the cell adjacent to the aircraft as shown by curve A in Figure 3.1. These pulses propagate away from the aircraft with diminishing amplitude. It is seen that the rate of rise of the pulses is very fast while their decay is comparatively slow. This is characteristic of air breakdown and electron attachment. The phenomenon can be explained by the value of the local field at the particular cell of interest. After the breakdown wave passes through, the conductivity of the cell starts to decrease. As the resistance rises, the field in the cell also rises until another breakdown of air occurs in the cell, whereupon the process is repeated to give the pulse structure in the conductivity curve. However, the pulse structure described is most probably a numerical phenomenon arising from the way the conductivity is calculated. In the present model, the conductivity of air is calculated only for those cells that constitute the lightning leader channel. Furthermore, to model the motion of the charges, which is mainly along the channel, the conductivity associated with the z-component of the field is computed as a function of time, while the conductivity associated with the r-component (transverse to the channel) is not calculated as a function of time. It is kept at a low constant value equal to the air conductivity outside the channel. In a previous three dimensional study where the conductivity of air is calculated in every cell and where the motion of charges is calculated consistently, no such pulse structure is seen in the conductivity curve adjacent to the nose of the aircraft.

Therefore the physical conductivity curve should be approximated by the smoothed average of the numerical curve.

From Figure 3.1, the speed of the leader channel is calculated to be  $3.6 \times 10^7$  m/s. The leader speed decreases to  $3 \times 10^7$  m/s and  $1.8 \times 10^7$  m/s for ambient fields of 0.35 and 0.25 MV/m respectively. It is seen that the leader velocity calculated from the model is strongly dependent on the ambient fields and is much higher than the measured value of about  $10^6$  m/s. In this model the locally enhanced field adjacent to the aircraft is responsible for the initiation of the corona discharge and subsequent propagation of the leader. With the existing radial resolution of 3 meters the enhancement factor is low. Consequently a relatively large ambient field is required for the initiation of the leader channel. With a larger enhancement factor from a finer grid, the ambient field required would be smaller, thereby lowering the calculated leader velocity. Numerically for the leader to propagate a few meters a field higher than the observed value is also required. This is not surprising because in this model the conductivity of the channel determines the field and hence the avalanche rate at the tip of the channel. In this respect the present model can be improved by the inclusion of other physical processes, such as photoionization and streamers, which are active at the tip of the channel. This is an area where further research work is much desired and can be fruitful. An initial effort to incorporate the effects of streamers has been done. It is rather difficult to include streamers into the finite difference code because of their microscopic dimension compared to the cell size in the code. Nevertheless the effects of streamers have been incorporated heuristically as shown in a previous report [4]. As formulated in reference [4], there are two free parameters to characterize the streamers: their velocity and their growth factor. The product of the growth factor and the excess positive ion density is the rate of electron-ion pairs produced over and above that produced by field and temperature ionizations. In the present implementation streamers are included in the cells at the leader tip only. When streamers are included the length of the leader channel typically increases by a factor of two or three over that without streamers. For the case of streamers with a velocity of  $10^6$  m/s and a growth factor of  $10^8$ , the leader channel would reach the problem space boundary when the ambient field is 0.45 MV/m.

The case in which charge centers exist along the leader channel has also been examined by placing charges in selected cells along the path of the channel, i.e. the axis. For the cell size utilized in the present model the charges that

can be placed in a given cell without exceeding the breakdown field is of the order of microcoulombs. With this charge at a distance at least 50m away from the aircraft, the field at the aircraft is very much smaller than the breakdown field. Additional ambient field of the order of breakdown field has to be imposed in the problem space. As such the development of the leader channel is then controlled mainly by the imposed ambient field. The effects of the charge centers are confined to the breakdown of the cells where the charges reside. Thus the present model needs to be improved to take into account the role of charge centers in leader propagation.

Thus far the emphasis has been on the propagation of the channel. It is also of interest to examine the other properties associated with the channel. For an ambient field of 0.45 MV/m the nose current as a function of time is shown in Figure 3.2. The maximum current is 9.6 kA. The nose current is taken to be the current in the cell adjacent to the aircraft. The current in a cell is calculated by the product of the field and the conductivity of the cell. The current in the channel decreases rapidly as the initial ambient field decreases. The corresponding maximum nose current decreases from 9.6 kA to 6.8 kA to 4.9 kA as the field decreases from .45 to .35 to .25 MV/m. The rate of rise of the lightning current from the model is about  $10^{12}$  A/s. However the breakdown of air in a given cell typically occurs in a couple of time steps in the model. Consequently the rate of rise of the lightning current is not accurately calculated by the present model, at least near the initiation point.

The densities of the charged particles in the channel six meters away from the aircraft are shown in Figures 3.3 - 3.5. The densities rise rapidly to a maximum as air breakdown commences in the cell upon the arrival of the leader tip. After the passage of the leader tip the densities decrease. The rate of decrease is much slower than the avalanche rate, and decreases with time. The rate of decrease is greatest for the electron density, especially in the short period immediately following air breakdown. The loss of the electrons is mainly through attachment to neutrals. the attachment rate is so high that a microsecond after air breakdown starts most of the negative charges are carried by negative ions and not by electrons. Since the mobility of the negative ions is much lower than electrons, the attachment of the electrons to neutrals to form negative ions results in rapid reduction of the conductivity of the leader channel. The temperature of the electrons rises rapidly and tends to oscillate around 20,000°K, which is close to the observed value. The temperature of the heavy particles increases by only a few degrees above the initial value, while the

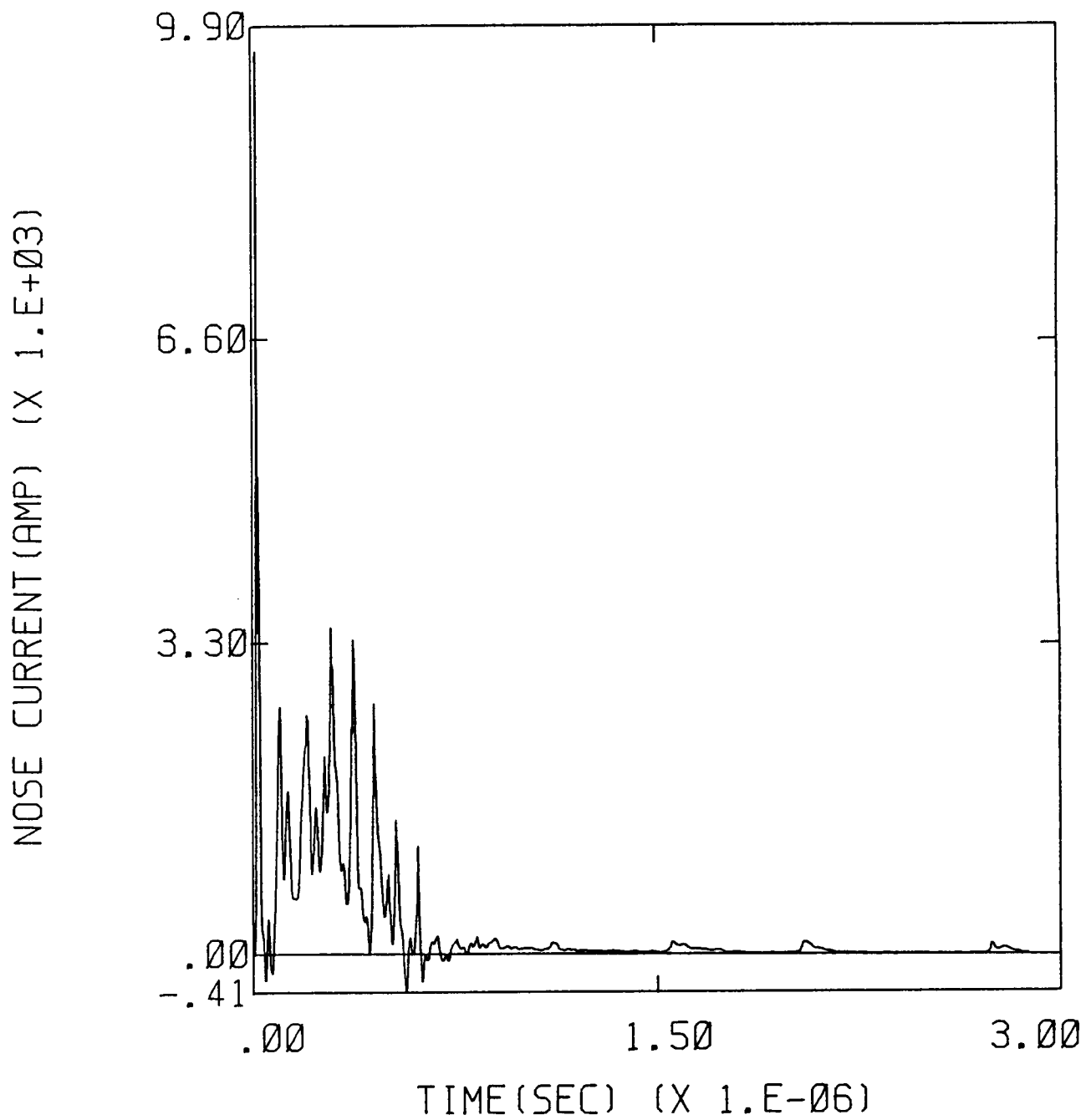
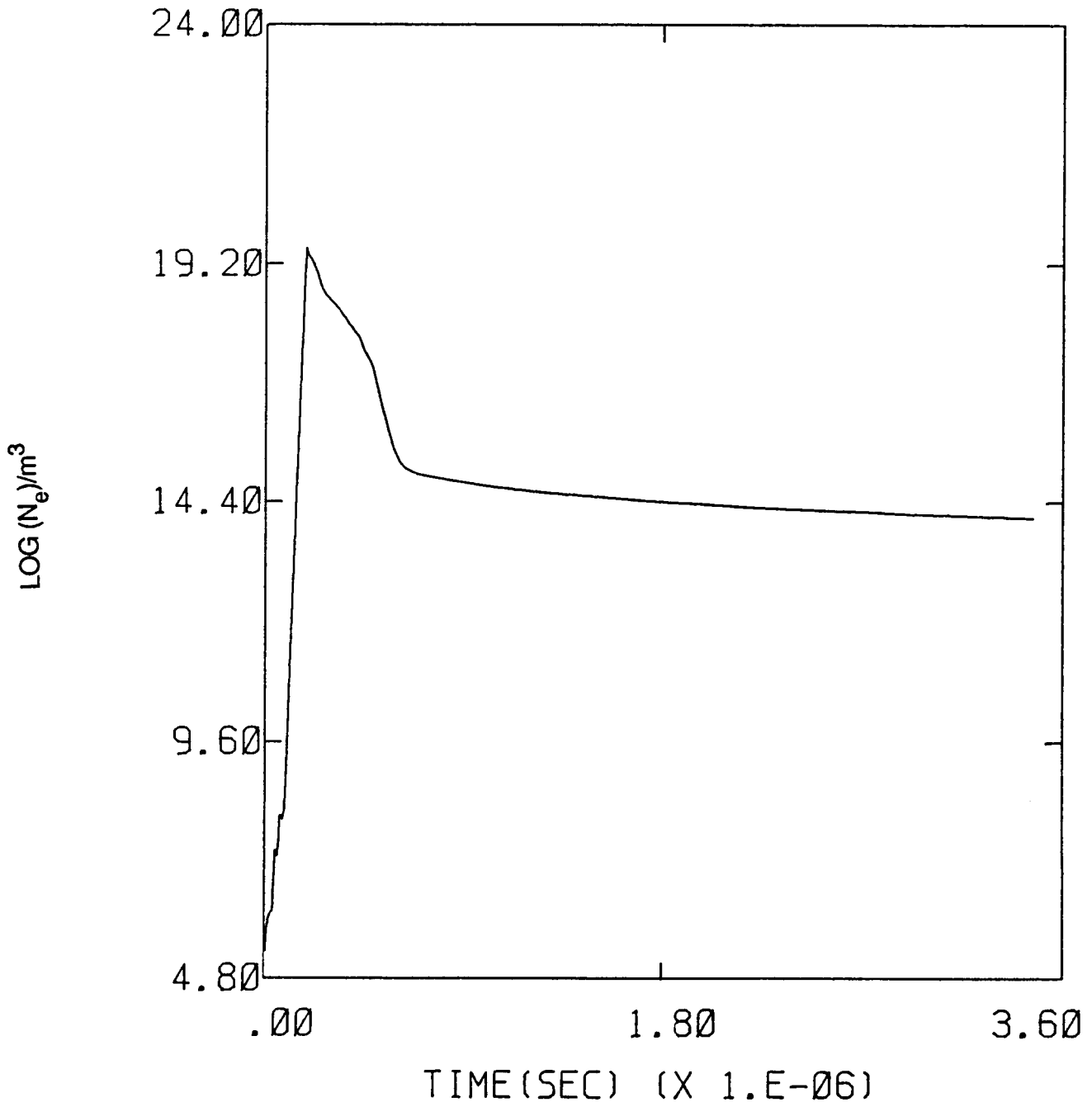
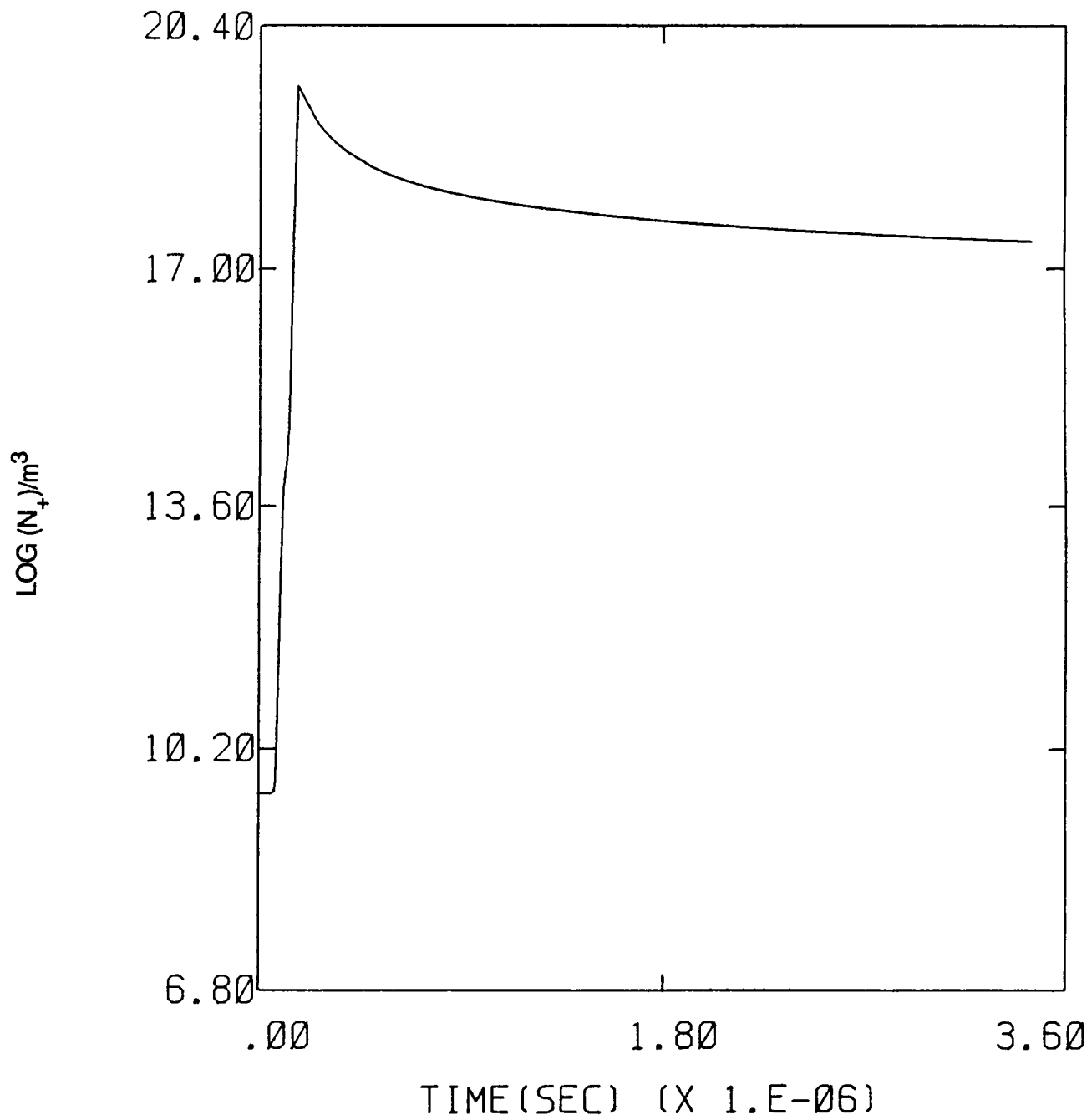


Figure 3.2 Channel Current Two Meters from Aircraft



**Figure 3.3 Electron Density Six Meters from Aircraft**





**Figure 3.4 Positive Ion Density Six Meters from Aircraft**

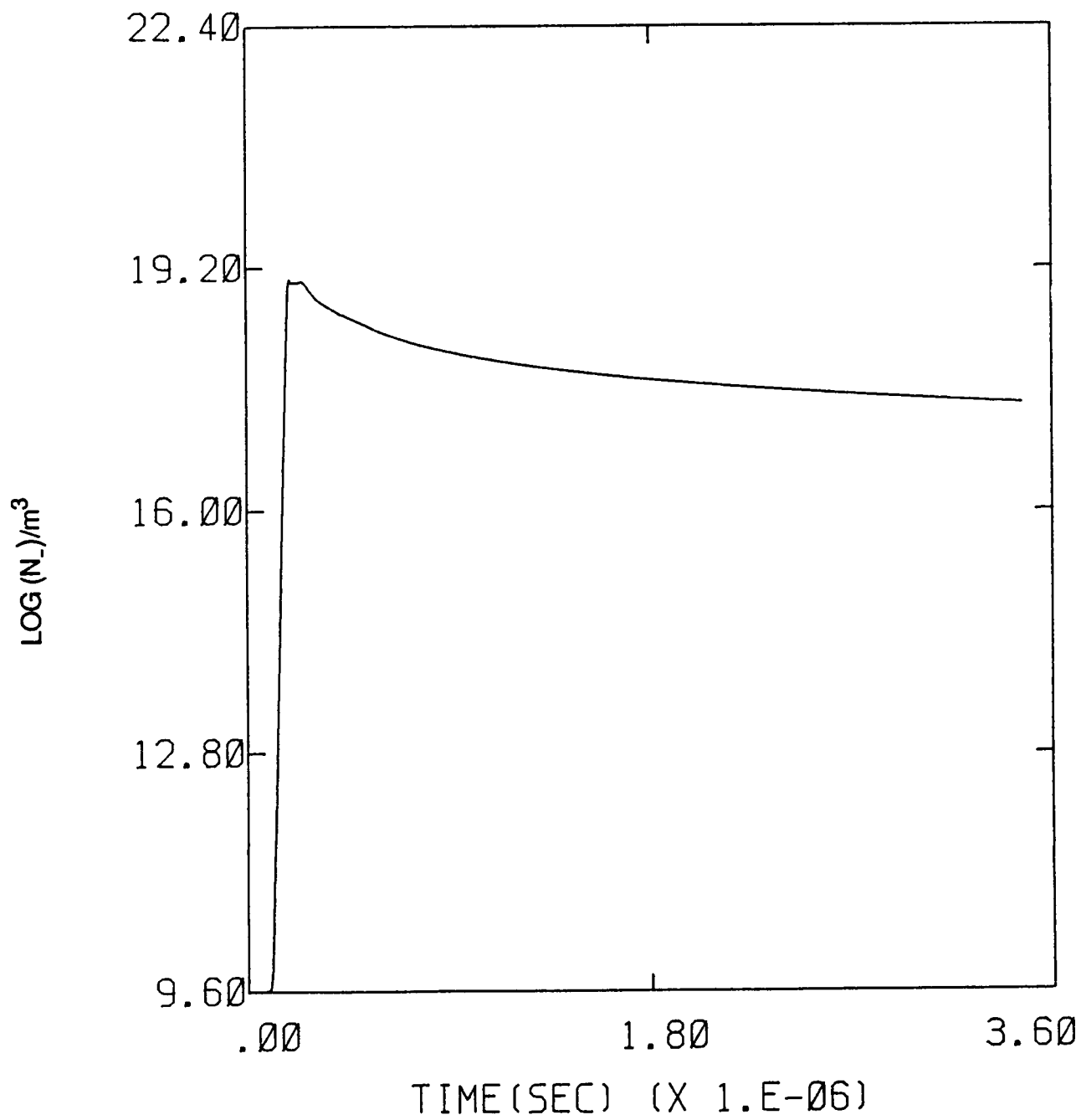


**Figure 3.5 Negative Ion Density Six Meters from Aircraft**

temperature of the vibrational reservoir has almost doubled. Therefore most of the electronic energy has gone into the excitation of the vibrational states. The transfer of vibrational energy to translation energy is hindered by the low neutral temperature. The low gas temperature is also a result of low degree of ionization, since the energy gained from the electric field by the relatively small number of charge carriers has to be shared among the gas particles. At this gas temperature the detachment rate is so low that most of the electrons remain attached. It is seen from Figures 3.3 -3.5 that after the rapid air breakdown the electron density is at least three orders of magnitude down from the ion densities.

In conclusion the corona discharge model has been successfully modified to study the propagation of the leader channel. The model is based on the consideration of some of the pertinent physical processes occurring in the breakdown of air; such as field and temperature ionization; recombination of charged particles to form neutrals, attachment of electrons to neutrals to form negative ions, detachment of electrons from negative ions, energy transfer between the various species and the vibrational energy reservoir. The length of the channel, the speed of the leader and the current have been shown to depend strongly on the strength of the ambient field. It was found that the energy gained by the heavy particles is stored in the vibrational energy reservoir of the neutrals. As a result the temperature of the heavy particles hardly increases. Electrons that were attached remain attached because of the low ionic temperature. With the loss of the free electrons the conductivity of the leader channel decreases rapidly and its propagation is terminated.

## CHAPTER 4

### 1984 DATA ANALYSIS AND INTERNAL WIRE MODELING

#### 4.1 Introduction

The 1984 thunderstorm season yielded a large quantity of measured lightning responses on the F106B. This chapter presents the analysis of that data and concentrates on the derivation of lightning currents from the response waveforms using the transfer function technique documented in a previous report [2]. These lightning currents are then used to drive the finite difference model of the F106B shown in Figure 4.1. This serves two purposes. The first is to verify that the transfer function model chosen is correct; essentially this means that the lightning attach point is correctly positioned. The verification is done by comparing calculated and measured response waveforms for sensors not used in the transfer function process. If these compare favorably the model can be trusted, if not, it is likely that the lightning attach point must be altered.

The second purpose of the finite difference model calculation is to determine the sources which couple to the inside of the aircraft via seams and apertures. These sources can then be used in a separate calculation to determine internal cable currents and voltages. The details of how this is done are presented later in this chapter. A number of overlays of measured versus predicted internal wire responses are presented as well as predicted responses in cases where no measured response was available.

#### 4.2 Lightning Current Analysis

There are several steps in the procedure which calculates a lightning current from a measured response. The procedure, described in more detail in Reference [2], is briefly as follows. A finite difference model of the F106B aircraft and surrounding space is constructed as shown in Figure 4.2. A lightning channel is added to the model in the form of a thin wire running from an assumed lightning attach point

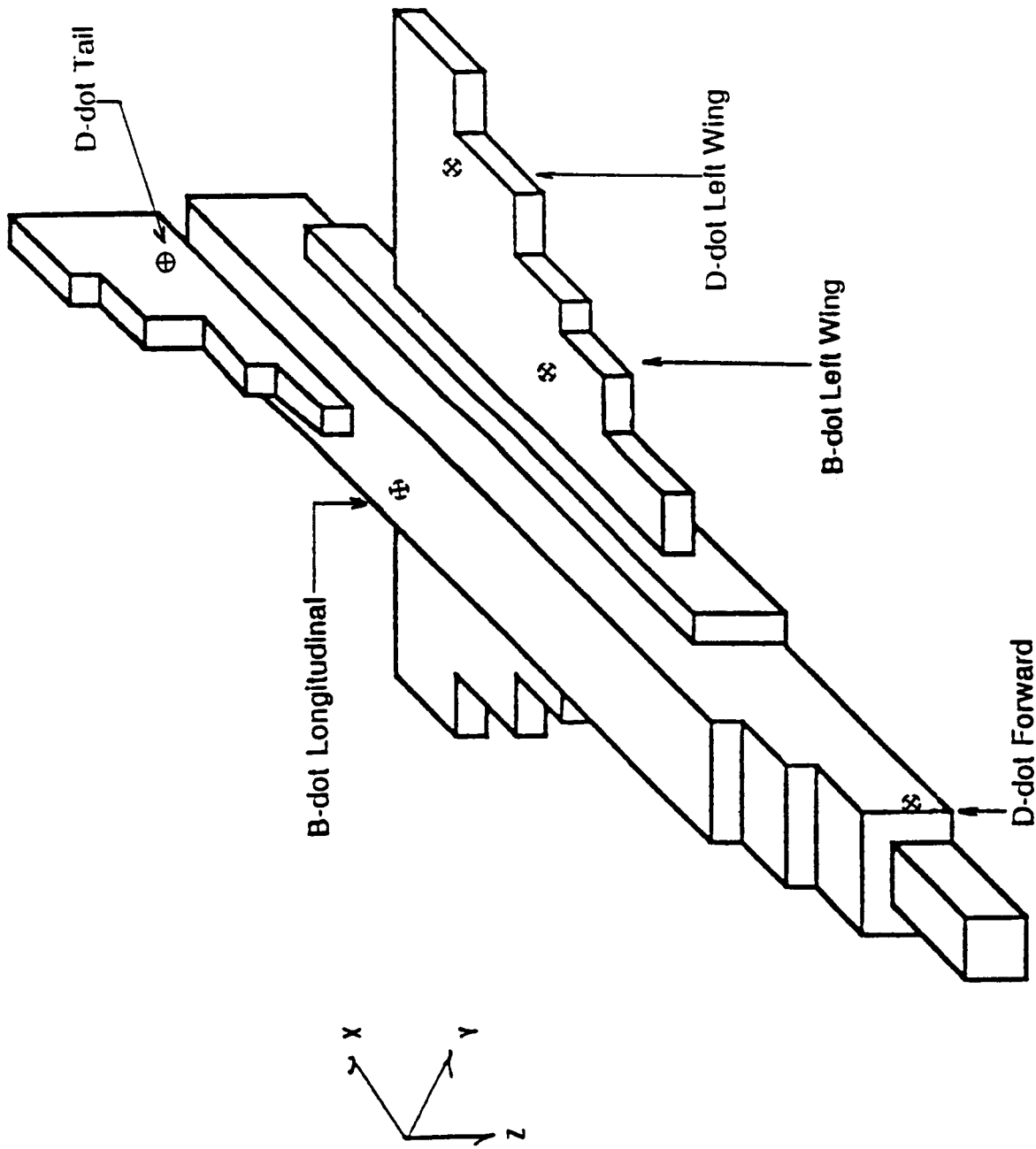
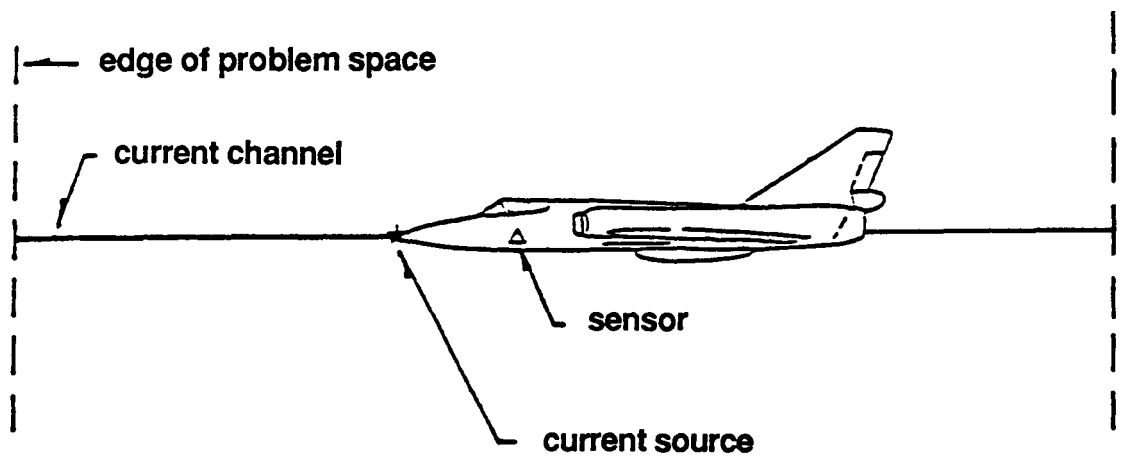


Figure 4.1 Block Model of the F106B Indicating Approximate Sensor Locations



**Figure 4.2 Typical Model Geometry for Triggered Lightning**

(usually the nose) to the boundary of the problem space. A source at the attach point of the thin wire drives a current on the wire simulating the effect of a triggered strike on the aircraft. The resulting current injected on the aircraft is Fourier transformed and divided into the Fourier transform of each of the calculated sensor responses on the F106B. This gives a number of transfer functions relating injected current at a given attach point to sensor response.

The next step is to Fourier transform a measured sensor response from an actual lightning strike on the F106B and to divide it by the appropriate transfer function calculated earlier. This results in a frequency domain function which is the injected current necessary to cause the measured sensor response in the finite difference model. This function is inverse transformed to give the time domain current at the attach point of the lightning channel. This derived current is then used in the finite difference model to calculate both sensor responses and the fields necessary to derive sources for internal coupling purposes. Clearly the measured sensor response must by definition match the one calculated by the finite difference code, but the other sensor responses are not required to do so. If these comparisons are also good, it is an indication that the model used is an accurate simulation of the triggered lightning event.

Sixty-five lightning strikes from the 1984 data set were analyzed in this way. In all cases the measured sensor response used to derive the lightning current was from the B-dot longitudinal or the D-dot forward sensor. The choice between these two was based first of all on which was available, if both were not, and secondly on which measured waveform gave better results.

In all cases a predicted quantity for the I-dot sensor response was calculated from the lightning current. This was calculated as shown below:

$$I\text{-dot nose} = \frac{\Delta I}{\Delta t} \quad (4.1)$$

where  $I$  is the lightning current at the nose sensor, and  $\Delta t$  is the time step used in the finite difference code (1 nanosecond). Predicted responses for I-dot nose were regenerated for each 1984 strike on which the sensors functioned properly. In

Figures 4.3(a) - 4.3(k) are shown overlaid measured and predicted I-dot nose waveforms. Each of these cases was modeled to 1 microsecond. Figure 4.4 shows I-dot nose predictions for possible multiple strike events. In these cases the modeled responses were calculated to 2 microseconds.

In summary it may be said that the comparison of the predicted versus the measured I-dot nose responses was in general quite good. Waveforms tend to overlay in terms of times of minima and maxima, and amplitudes are usually within twenty percent. There were several cases in which disagreements were as much as a factor of three between measured and predicted values. In these cases it is likely that the attach point chosen for the model was incorrect.

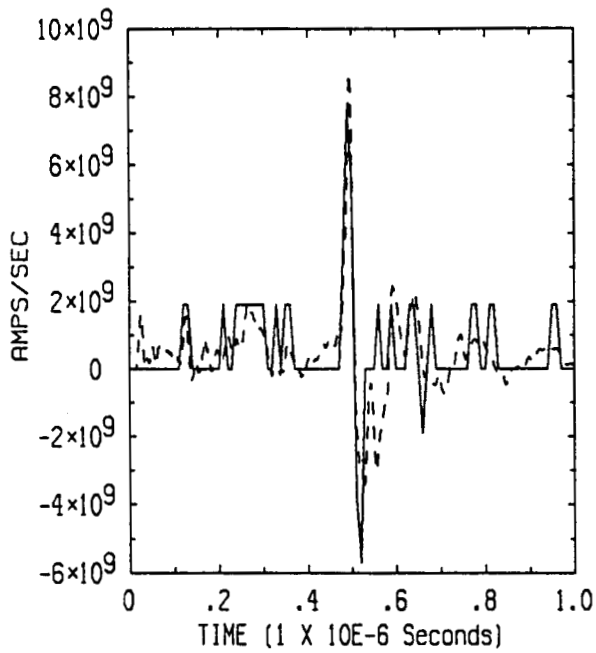
Some general observations about the calculated and measured sensor responses may be made. Magnitudes for the I-dot nose sensor responses usually ranged  $\pm 25 \times 10^9$  A/s, but were measured as high as  $\pm 50 \times 10^9$  A/s for a few cases. I-dot nose response magnitudes of  $\pm 30 \times 10^9$  A/s in general correspond to D-dot forward and B-dot longitudinal magnitudes of  $\pm 15$  A/m and  $\pm 1500$  T/s, respectively. The relationship between these different sensor responses seems to be linear, so it can be expected that every  $10^{10}$  A/s increase in I-dot nose will result in increases in D-dot forward and B-dot longitudinal of 5 A/m and 500 T/s, respectively. It should be noted that the maximum values discussed here are those derived from transient measurements. Peak detector measurements in most cases found significantly higher values.

#### **4.3 Internal Coupling and Internal Wire Modeling**

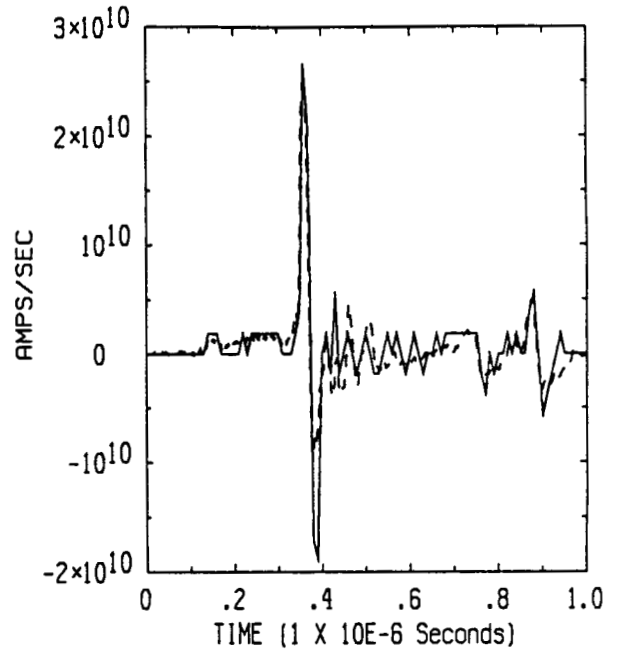
Electromagnetic energy generated by lightning channels attached to an aircraft can produce fields inside the aircraft. External fields on the aircraft surface can couple to the interior via external wiring and antennas leading to the interior, diffusion through the aircraft surface, seams and joints, and apertures. One of the most significant consequences of internal coupling is that the external fields caused by the attached channel can induce voltages and currents on internal wiring routed across or near these points of entry into the aircraft. For the F106B, the largest mode of internal coupling to the fuselage and wing wires appears to be through seams around the wheel well and instrument bay doors.

(text continued on page 62)

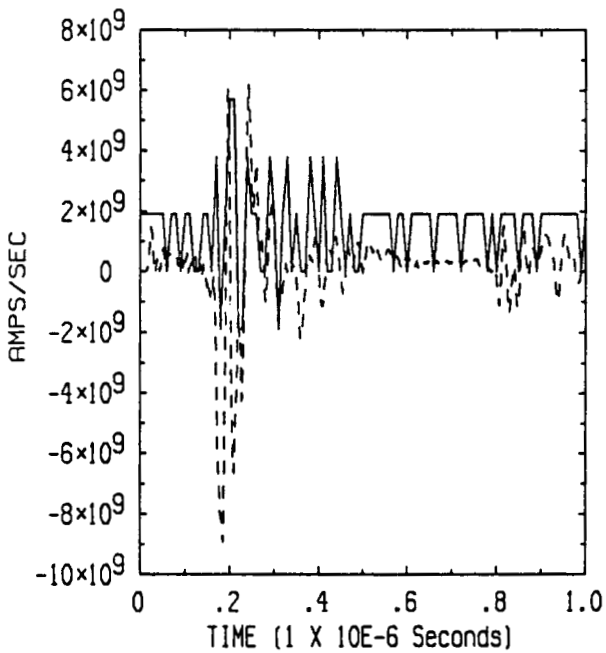




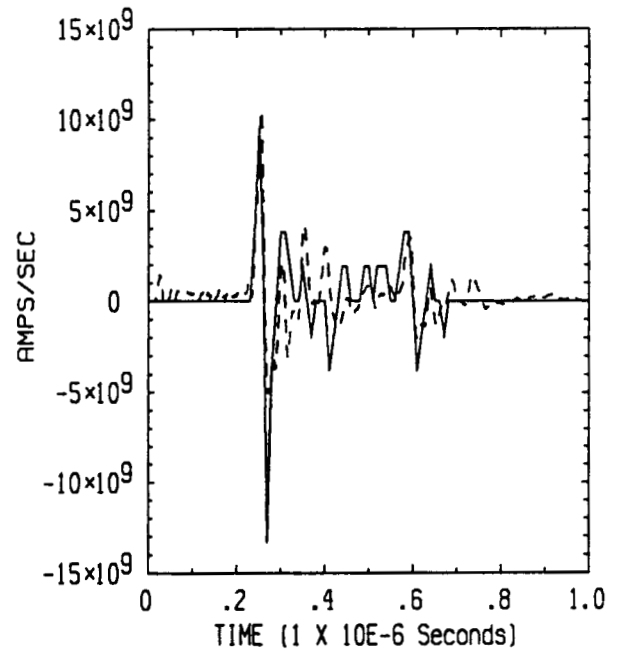
I-DOT NOSE  
 - MEASURED; -- PREDICTED  
 Flight 84-024, run 001, strike 001



I-DOT NOSE  
 - MEASURED; -- PREDICTED  
 Flight 84-024, run 003, strike 003

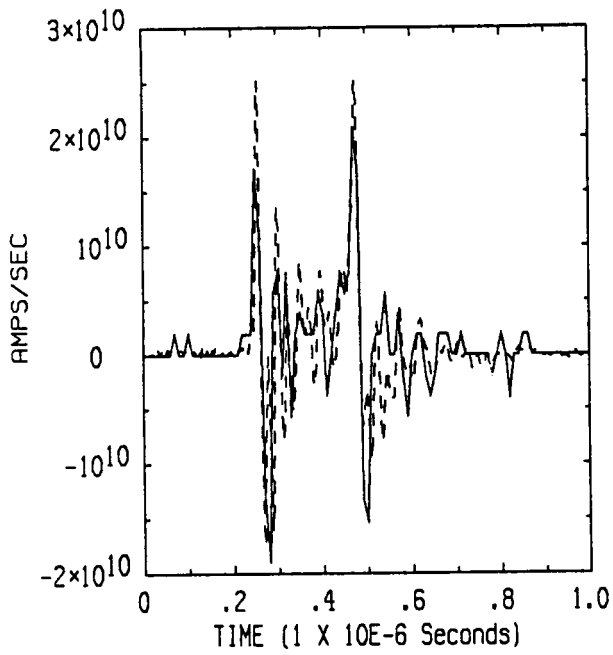


I-DOT NOSE  
 - MEASURED; -- PREDICTED  
 Flight 84-025, run 001, strike 001

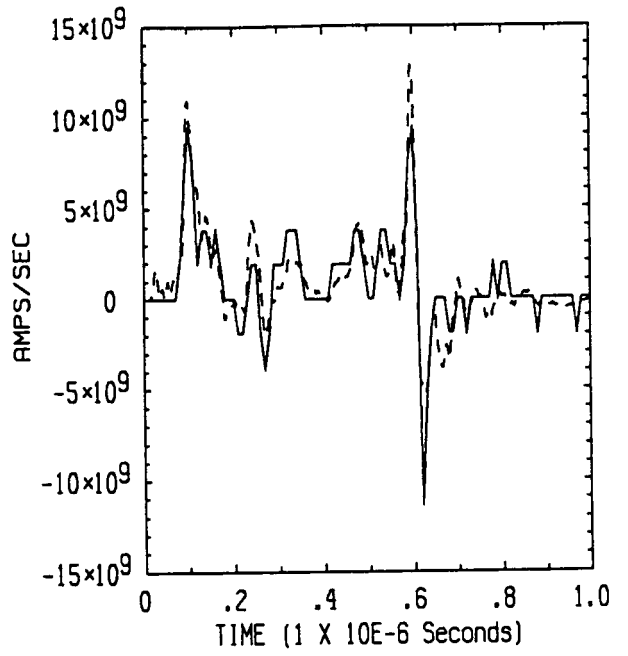


I-DOT NOSE  
 - MEASURED; -- PREDICTED  
 Flight 84-025, run 002, strike 003

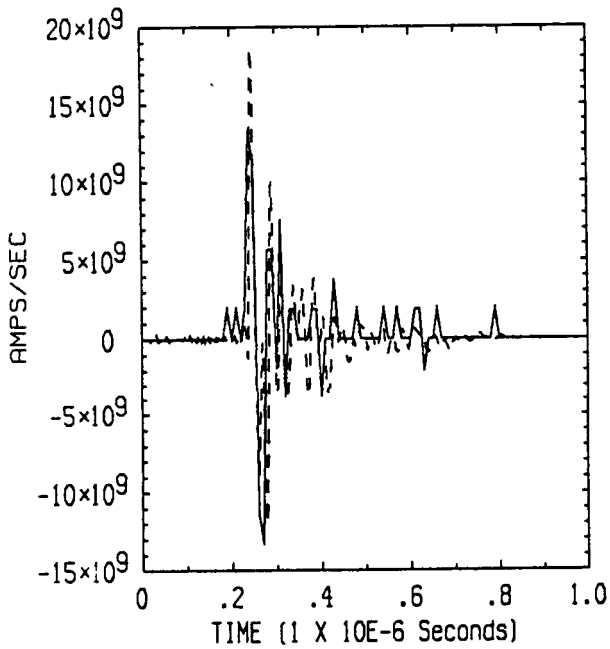
**Figure 4.3(a) Measured versus Predicted I-dot Nose Waveforms**



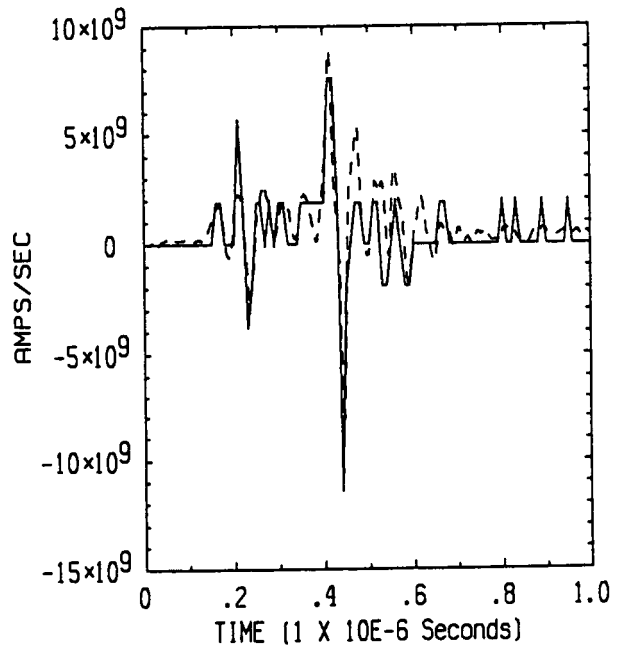
I-DOT NOSE  
 - MEASURED; -- PREDICTED  
 Flight 84-025, run 003, strike 004



I-DOT NOSE  
 - MEASURED; -- PREDICTED  
 Flight 84-025, run 004, strike 005

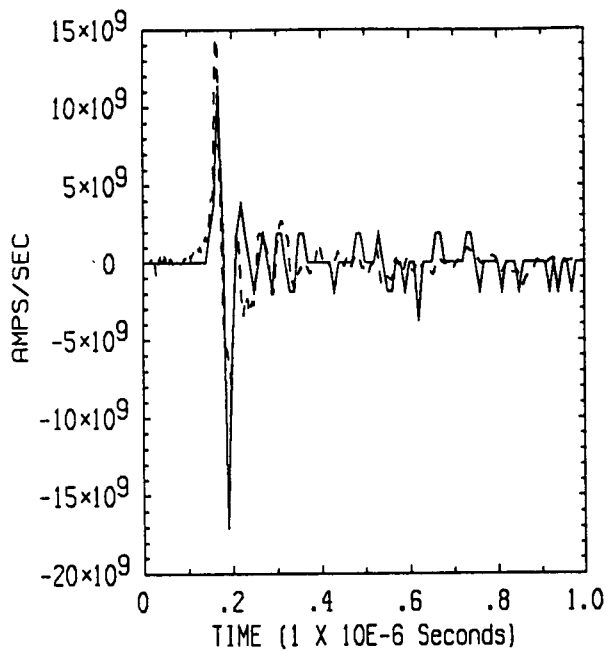


I-DOT NOSE  
 - MEASURED; -- PREDICTED  
 Flight 84-025, run 007, strike 010

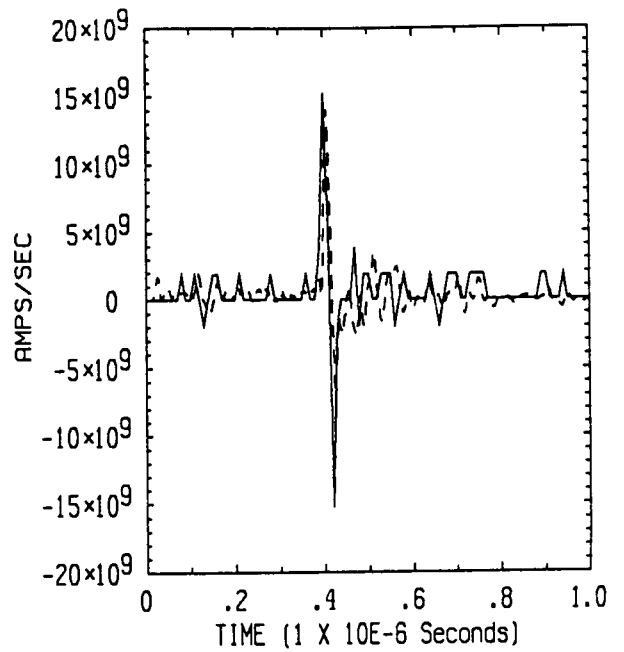


I-DOT NOSE  
 - MEASURED; -- PREDICTED  
 Flight 84-025, run 008, strike 011

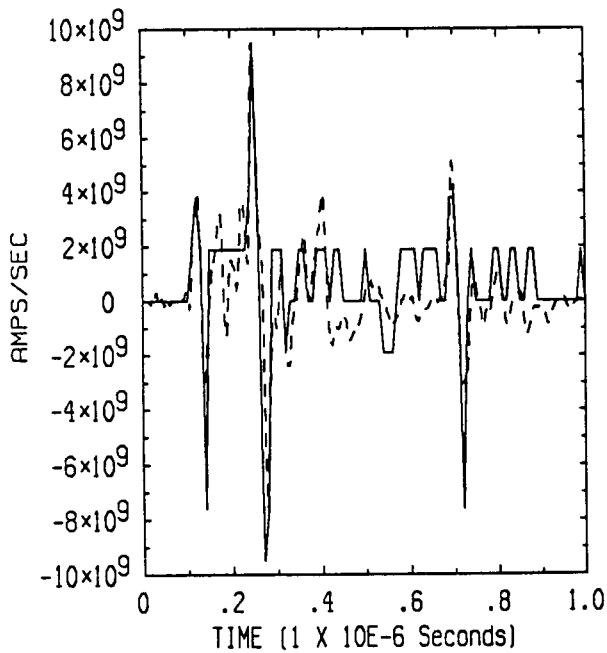
**Figure 4.3(b) Measured versus Predicted I-dot Nose Waveforms**



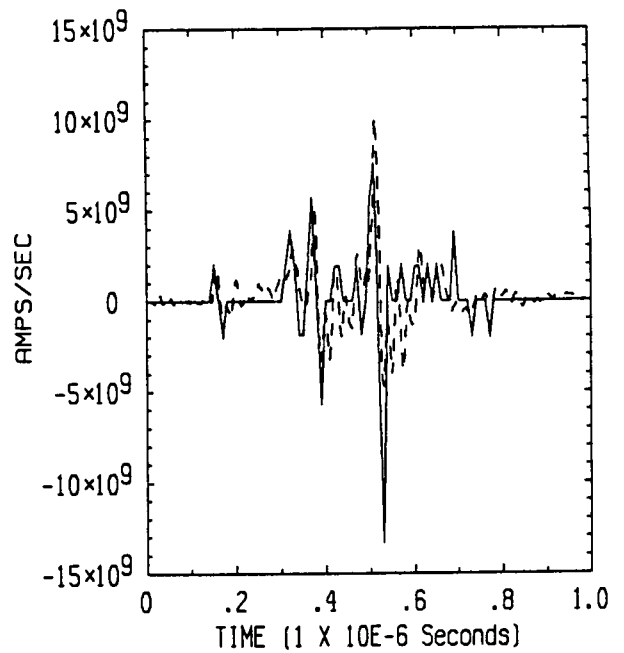
I-DOT NOSE  
 - MEASURED; -- PREDICTED  
 Flight 84-025, run 011, strike 014



I-DOT NOSE  
 - MEASURED; -- PREDICTED  
 Flight 84-025, run 013, strike 017

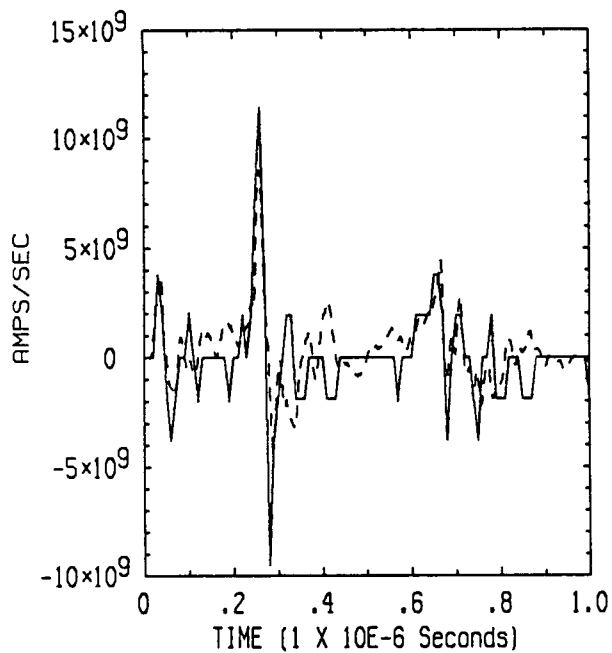


I-DOT NOSE  
 - MEASURED; -- PREDICTED  
 Flight 84-025, run 015, strike 019

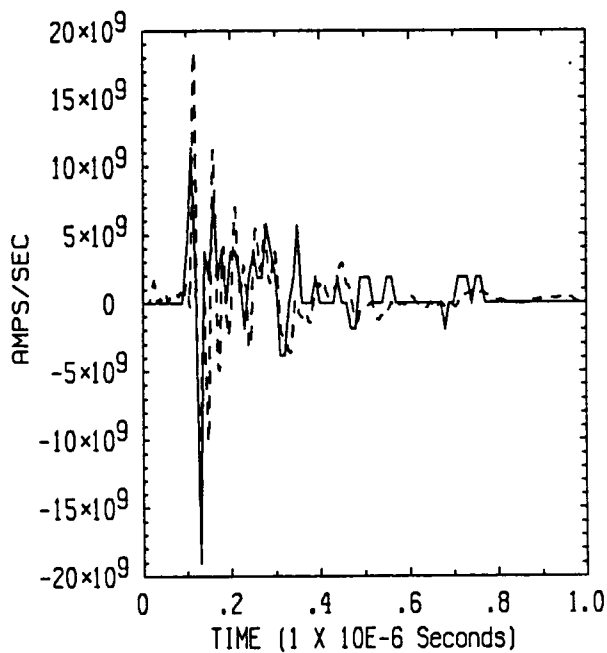


I-DOT NOSE  
 - MEASURED; -- PREDICTED  
 Flight 84-027A, run 001, strike 001

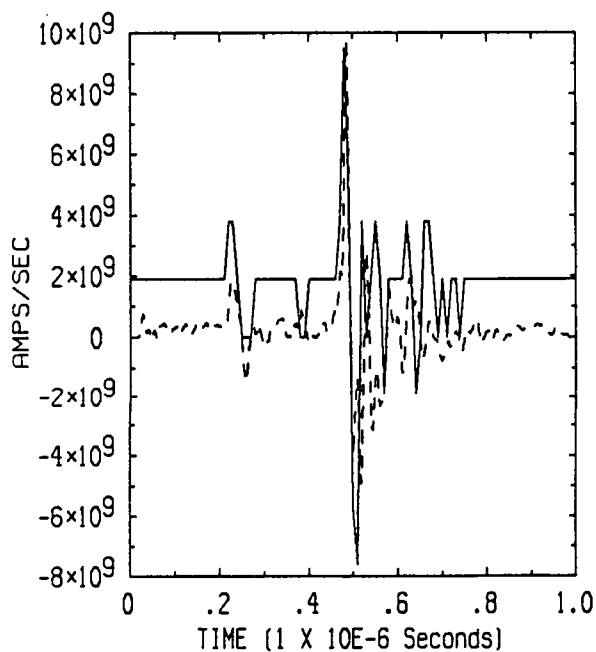
**Figure 4.3(c) Measured versus Predicted I-dot Nose Waveforms**



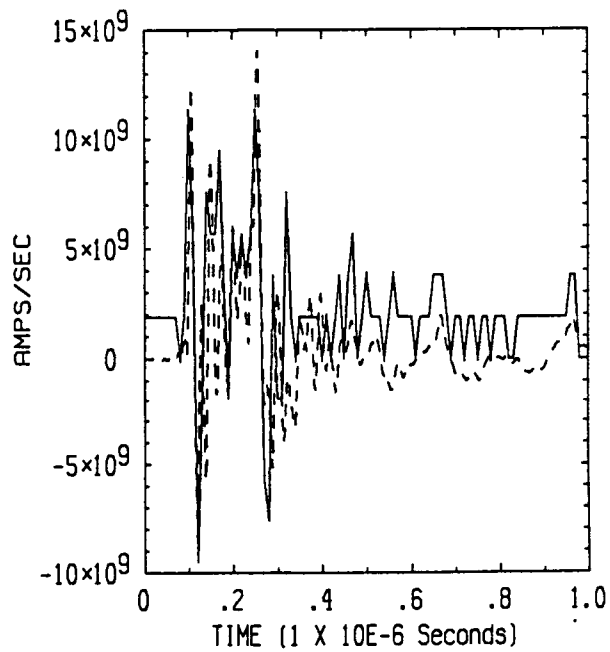
I-DOT NOSE  
 - MEASURED; -- PREDICTED  
 Flight 84-027B, run 001, strike 001



I-DOT NOSE  
 - MEASURED; -- PREDICTED  
 Flight 84-027A, run 002, strike 002

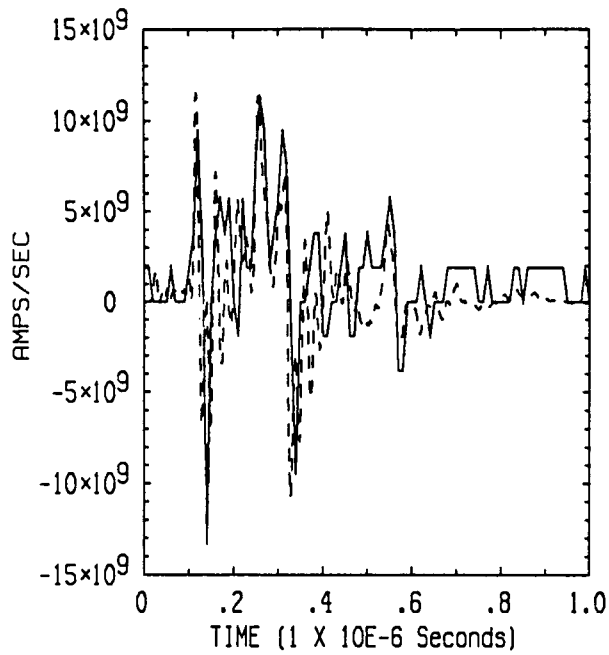


I-DOT NOSE  
 - MEASURED; -- PREDICTED  
 Flight 84-027B, run 002, strike 002

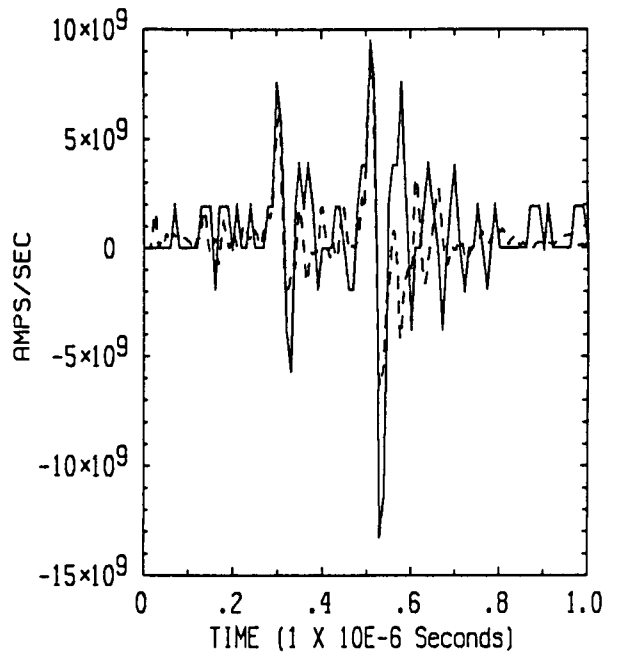


I-DOT NOSE  
 - MEASURED; -- PREDICTED  
 Flight 84-027, run 004, strike 005

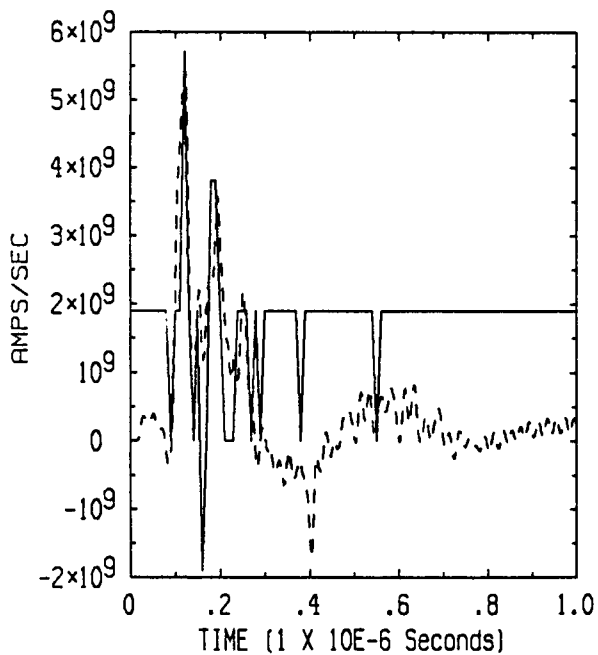
**Figure 4.3(d) Measured versus Predicted I-dot Nose Waveforms**



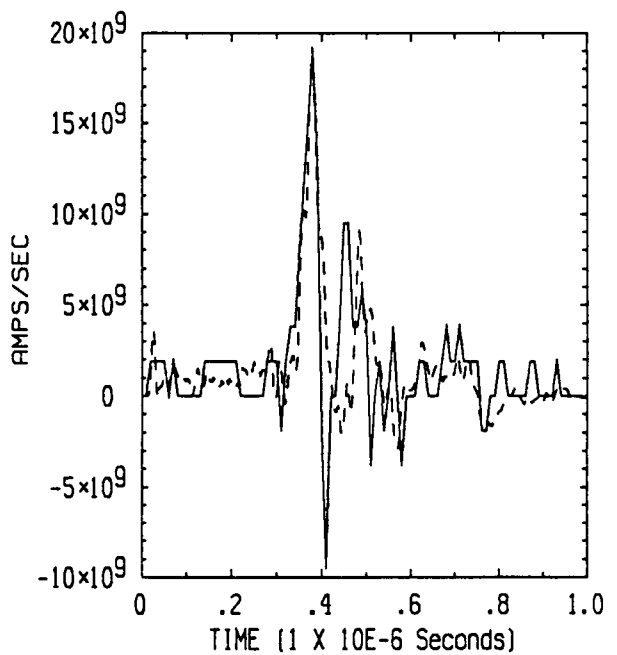
I-DOT NOSE  
 - MEASURED; -- PREDICTED  
 Flight 84-027, run 005, strike 006



I-DOT NOSE  
 - MEASURED; -- PREDICTED  
 Flight 84-029, run 001, strike 001

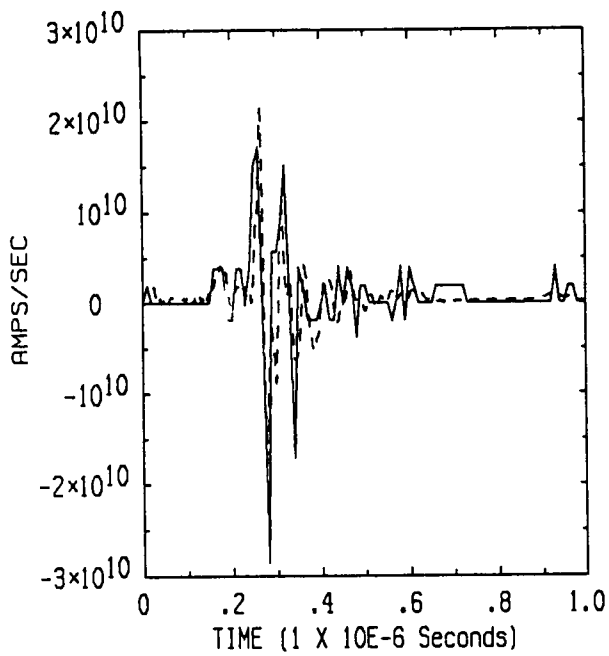


I-DOT NOSE  
 - MEASURED; -- PREDICTED  
 Flight 84-032, run 001, strike 002

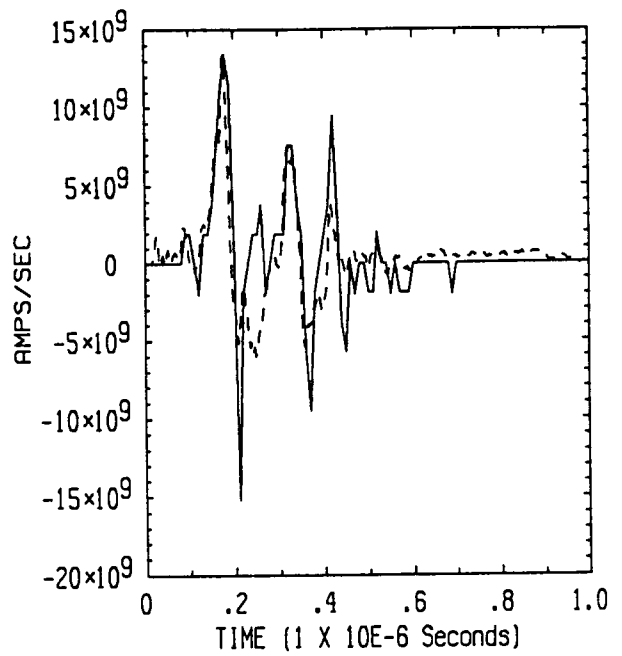


I-DOT NOSE  
 - MEASURED; -- PREDICTED  
 Flight 84-032, run 002, strike 003

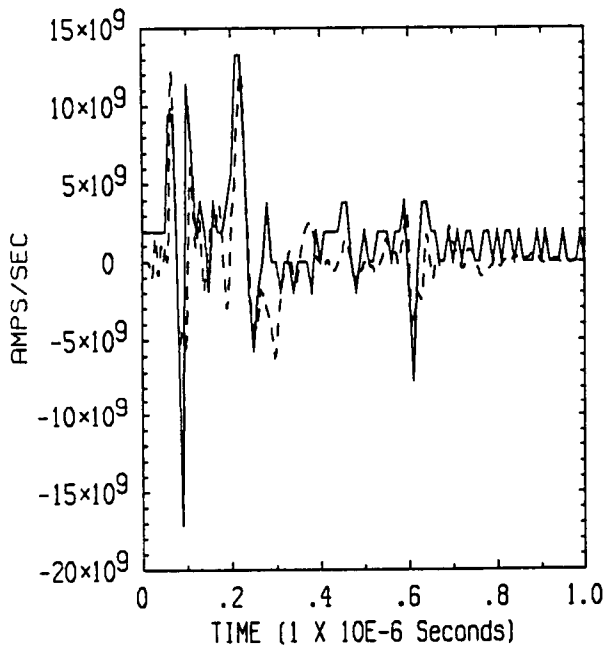
**Figure 4.3(e) Measured versus Predicted I-dot Nose Waveforms**



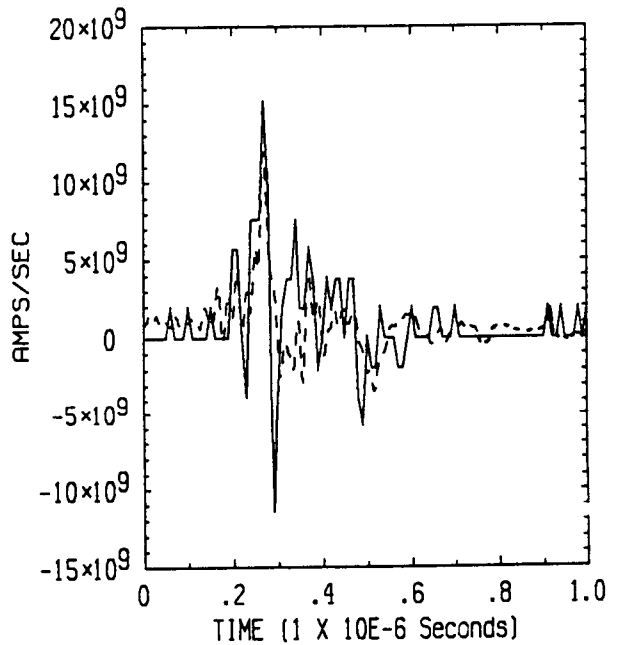
I-DOT NOSE  
 - MEASURED; -- PREDICTED  
 Flight 84-032, run 002, strike 004



I-DOT NOSE  
 - MEASURED; -- PREDICTED  
 Flight 84-032, run 003, strike 005

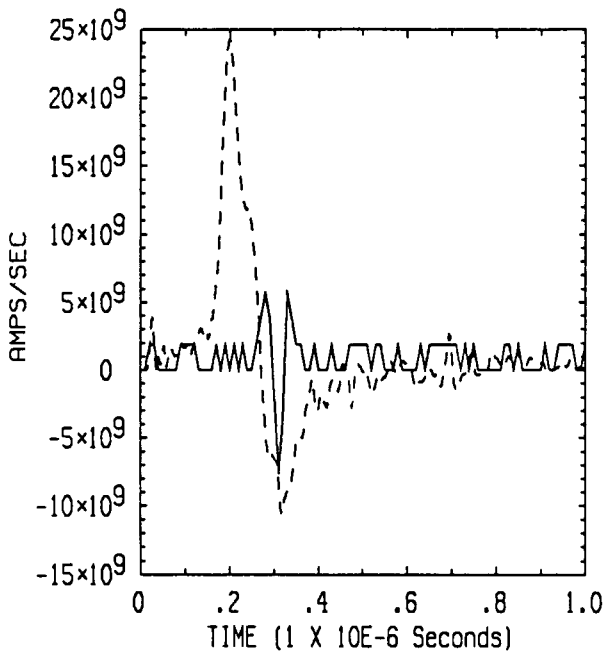


I-DOT NOSE  
 - MEASURED; -- PREDICTED  
 Flight 84-032, run 004, strike 013

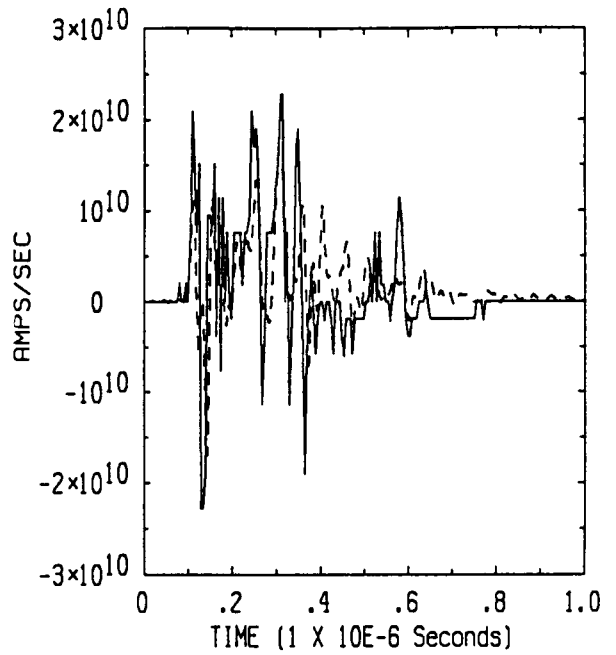


I-DOT NOSE  
 - MEASURED; -- PREDICTED  
 Flight 84-035, run 001, strike 001

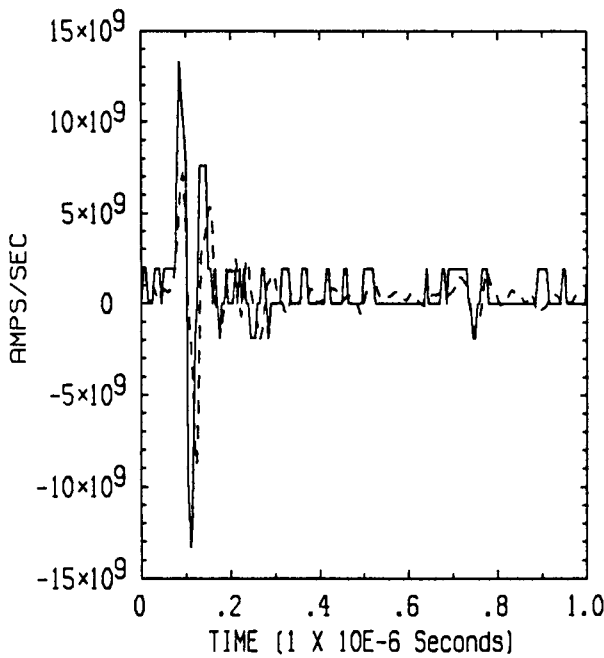
**Figure 4.3(f) Measured versus Predicted I-dot Nose Waveforms**



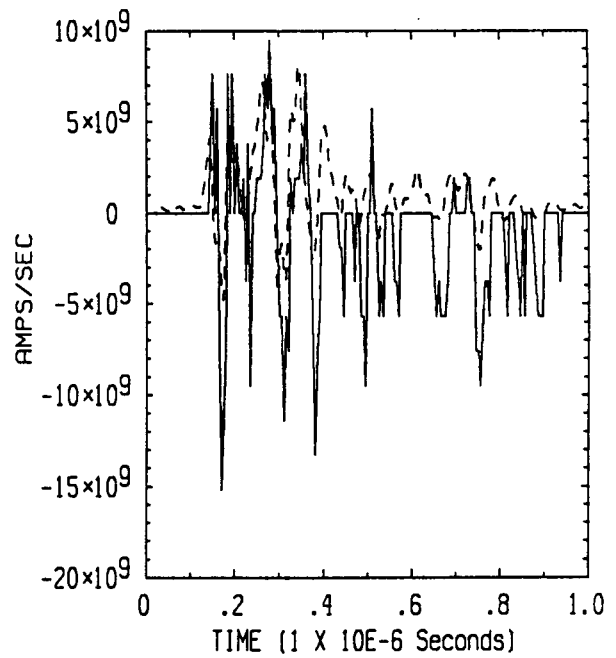
I-DOT NOSE  
 - MEASURED; -- PREDICTED  
 Flight 84-035, run 003, strike 004



I-DOT NOSE  
 - MEASURED; -- PREDICTED  
 Flight 84-036, run 001, strike 001

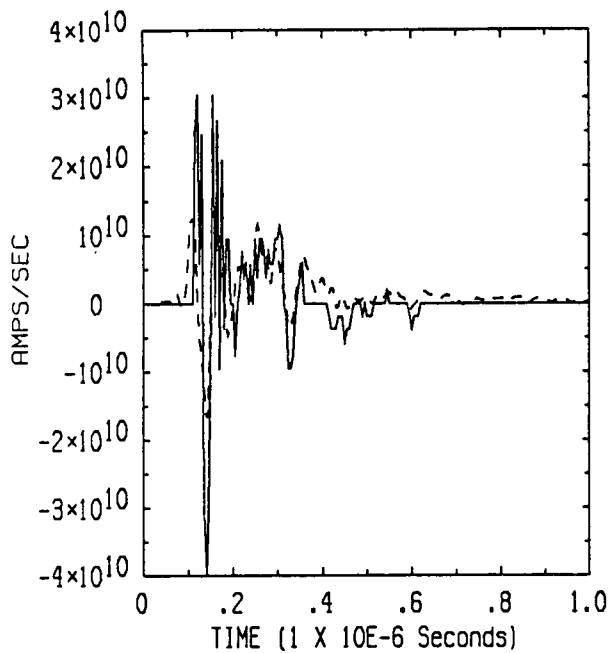


I-DOT NOSE  
 - MEASURED; -- PREDICTED  
 Flight 84-036, run 002, strike 002

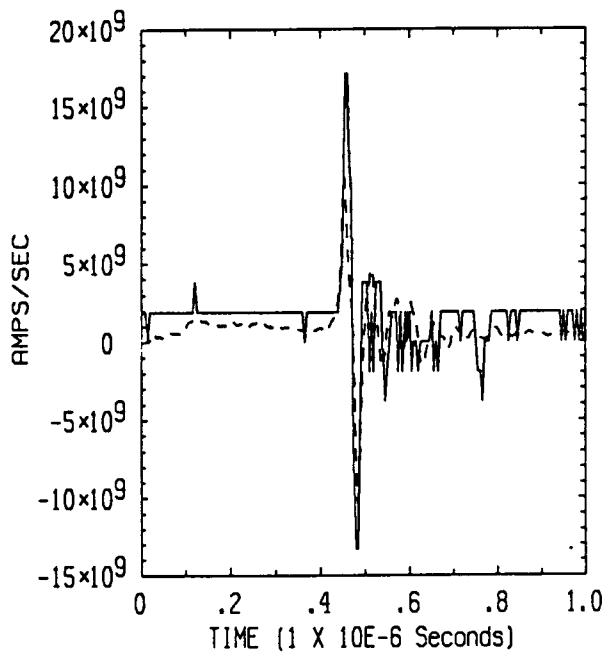


I-DOT NOSE  
 - MEASURED; -- PREDICTED  
 Flight 84-036, run 006, strike 009

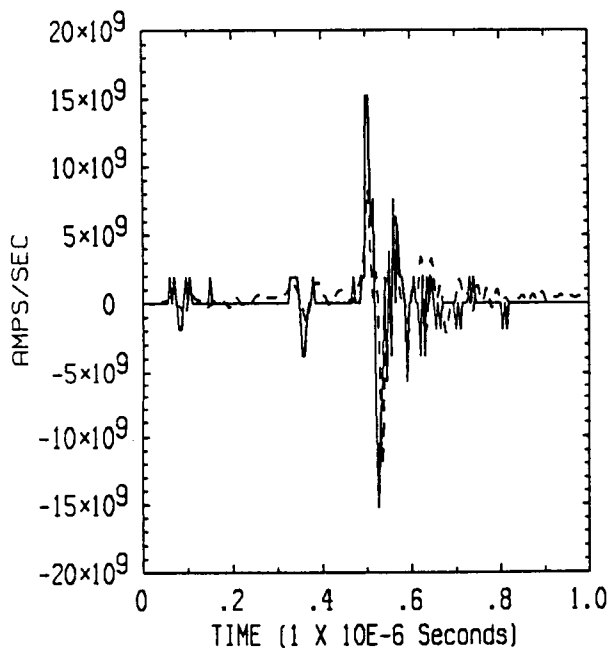
**Figure 4.3(g) Measured versus Predicted I-dot Nose Waveforms**



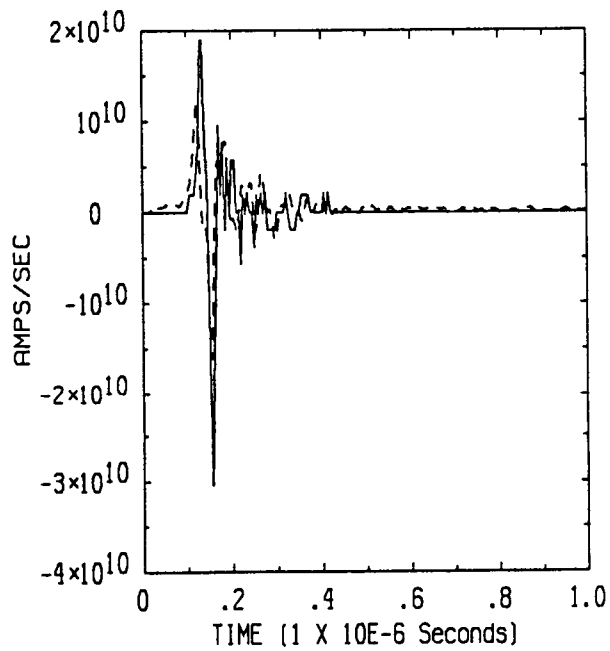
I-DOT NOSE  
 - MEASURED; -- PREDICTED  
 Flight 84-037, run 002, strike 018



I-DOT NOSE  
 - MEASURED; -- PREDICTED  
 Flight 84-037, run 003, strike 022



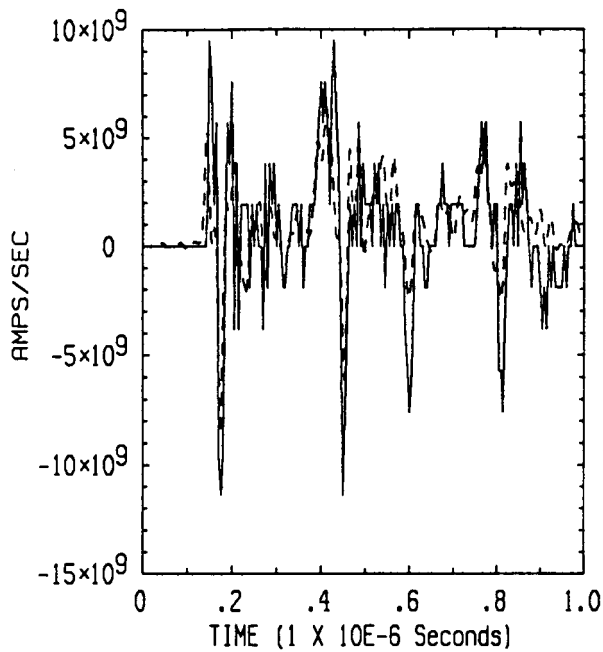
I-DOT NOSE  
 - MEASURED; -- PREDICTED  
 Flight 84-037, run 004, strike 024



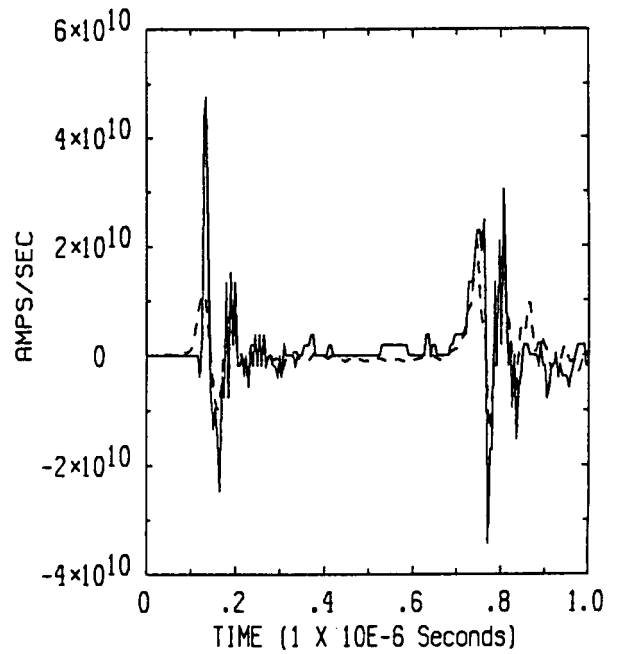
I-DOT NOSE  
 - MEASURED; -- PREDICTED  
 Flight 84-037, run 005, strike 029

**Figure 4.3(h) Measured versus Predicted I-dot Nose Waveforms**

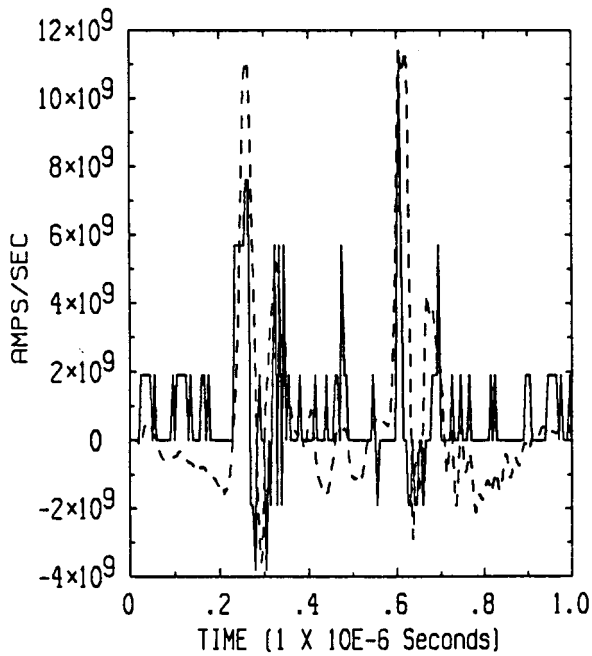




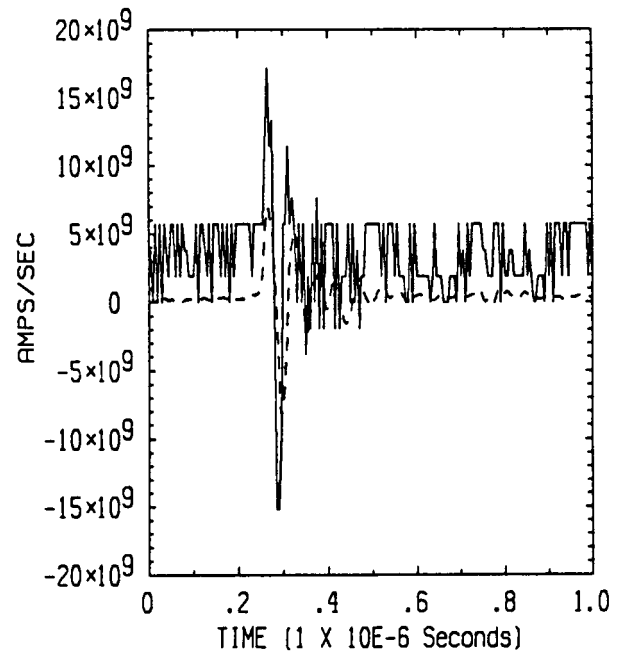
I-DOT NOSE  
 - MEASURED; -- PREDICTED  
 Flight 84-037, run 006, strike 034



I-DOT NOSE  
 - MEASURED; -- PREDICTED  
 Flight 84-037, run 008, strike 041

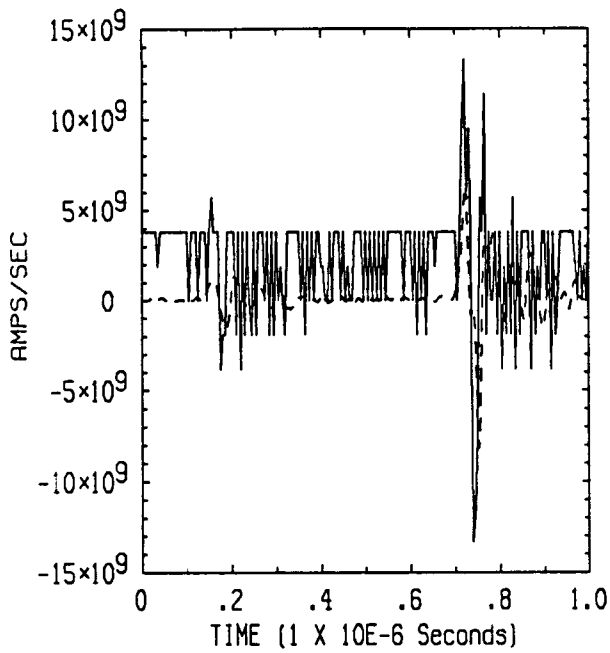


I-DOT NOSE  
 - MEASURED; -- PREDICTED  
 Flight 84-037, run 010, strike 052

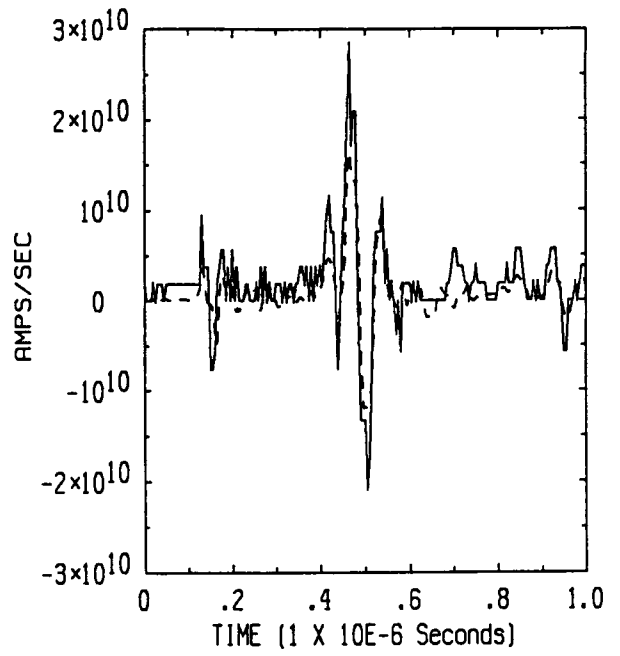


I-DOT NOSE  
 - MEASURED; -- PREDICTED  
 Flight 84-037, run 014, strike 058

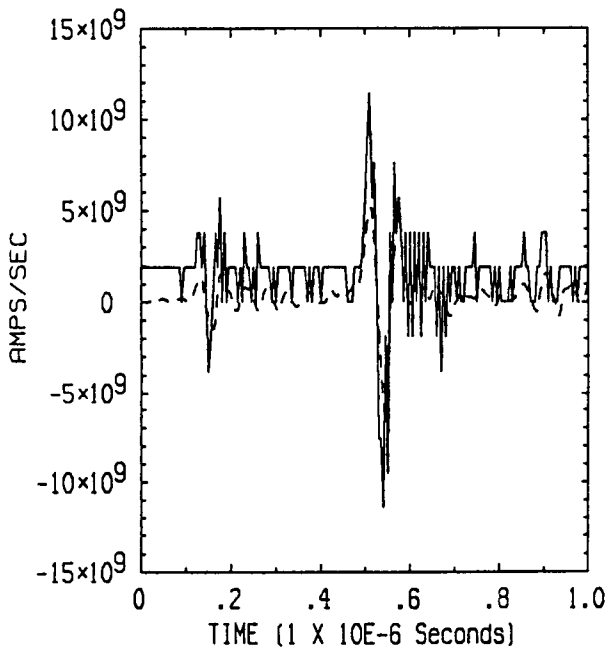
**Figure 4.3(i) Measured versus Predicted I-dot Nose Waveforms**



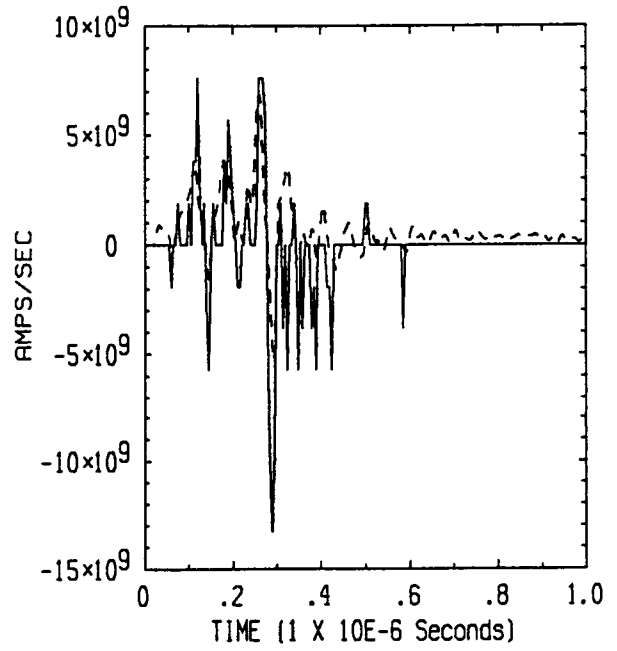
I-DOT NOSE  
 - MEASURED; -- PREDICTED  
 Flight 84-037, run 015, strike 062



I-DOT NOSE  
 - MEASURED; -- PREDICTED  
 Flight 84-037, run 017, strike 066

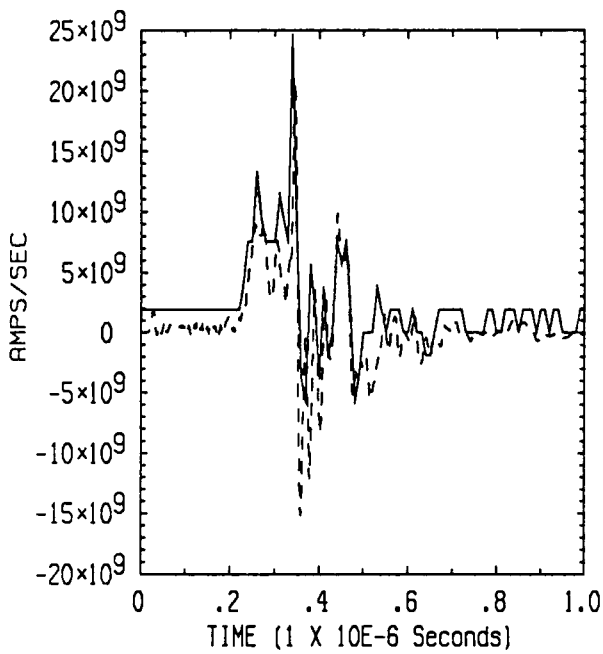


I-DOT NOSE  
 - MEASURED; -- PREDICTED  
 Flight 84-037, run 019, strike 071

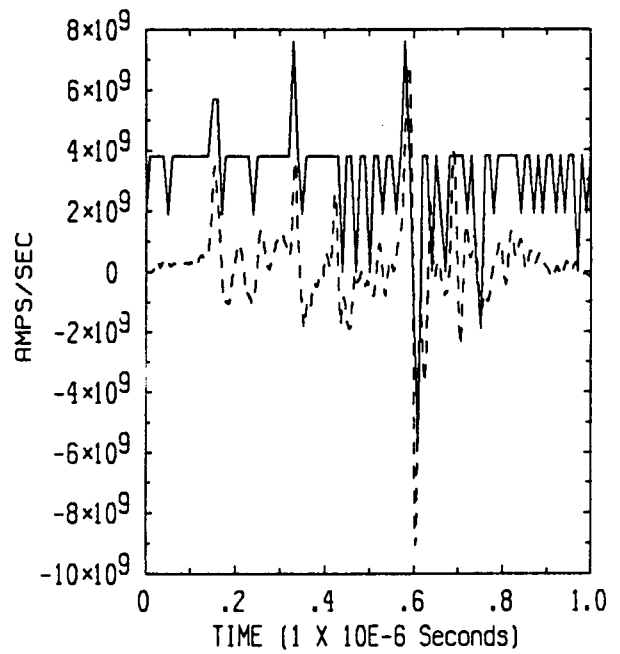


I-DOT NOSE  
 - MEASURED; -- PREDICTED  
 Flight 84-037, run 001, strike 002

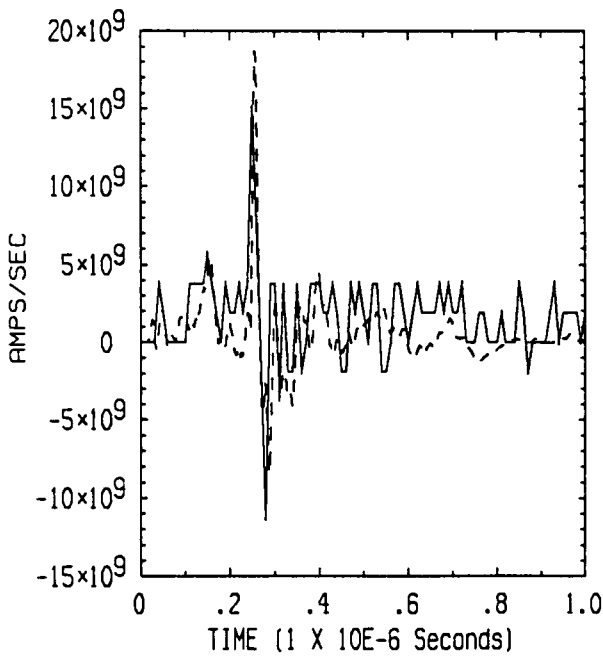
**Figure 4.3(j) Measured versus Predicted I-dot Nose Waveforms**



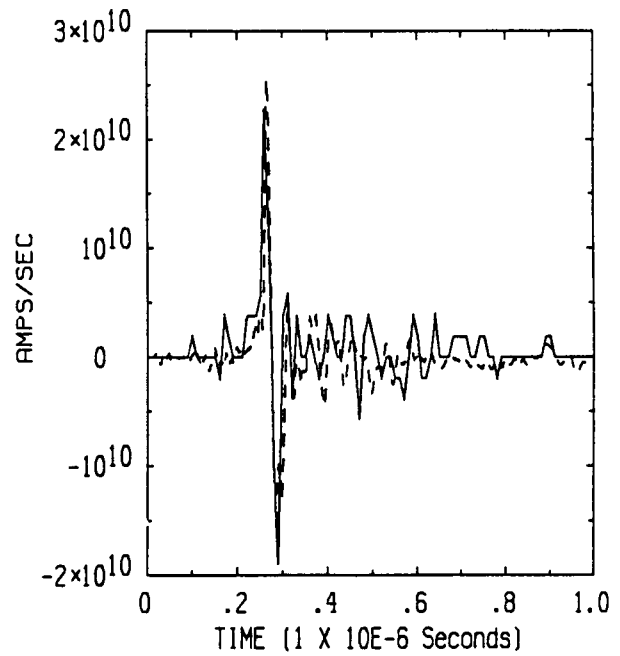
I-DOT NOSE  
 - MEASURED; -- PREDICTED  
 Flight 84-042, run 001, strike 001



I-DOT NOSE  
 - MEASURED; -- PREDICTED  
 Flight 84-042, run 003, strike 003

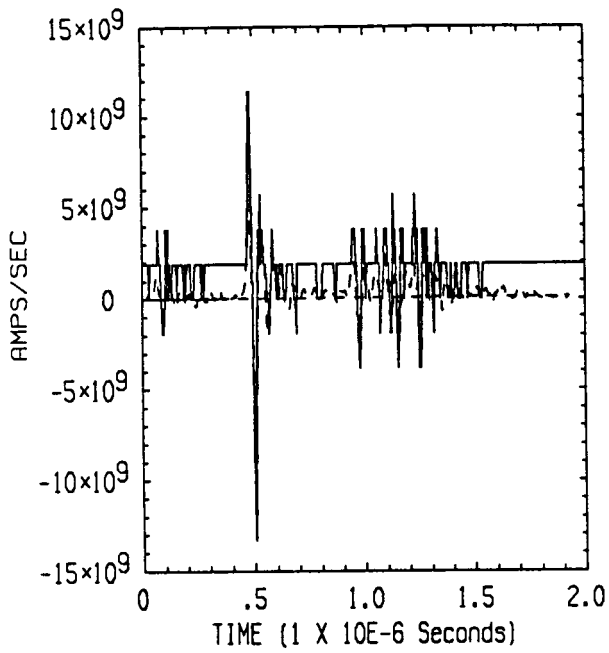


I-DOT NOSE  
 - MEASURED; -- PREDICTED  
 Flight 84-042, run 005, strike 005

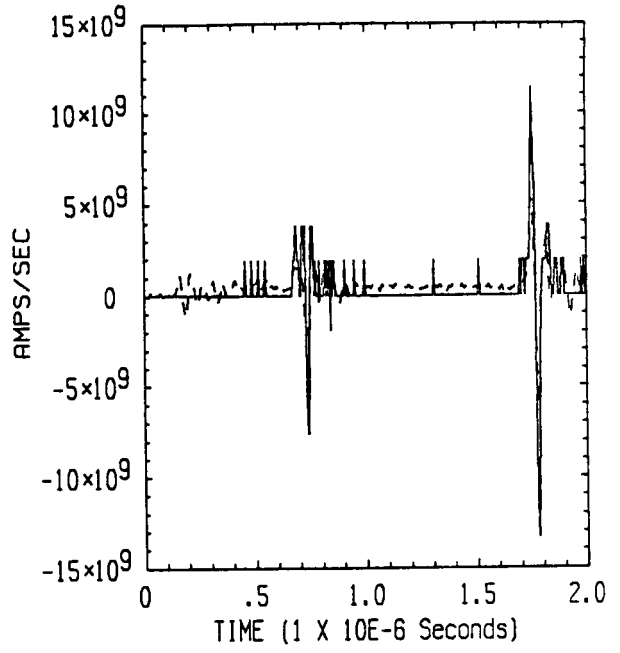


I-DOT NOSE  
 - MEASURED; -- PREDICTED  
 Flight 84-043, run 002, strike 003

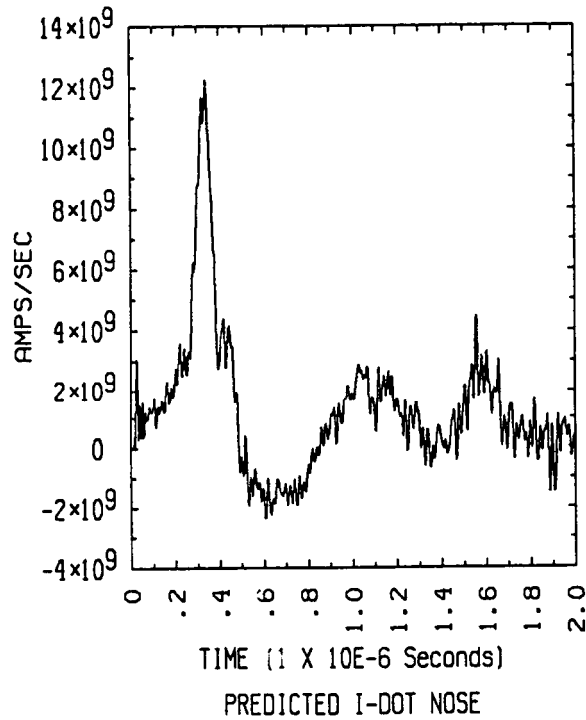
**Figure 4.3(k) Measured versus Predicted I-dot Nose Waveforms**



I-DOT NOSE  
 - MEASURED; -- PREDICTED  
 Flight 84-037, run 009, strike 044



I-DOT NOSE  
 - MEASURED; -- PREDICTED  
 Flight 84-037, run 016, strike 063



PREDICTED I-DOT NOSE  
 Flight 84-050, run 07A, strike 16A

**Figure 4.4 I-dot Nose Waveforms for Possible Multiple Strike Events**

Because these seams have no deliberate electrical connections across them, it is likely that the electromagnetic coupling through these seams is inductive. That is, the internal voltage sources are directly proportional to the time derivative of the current density on the outside skin of the aircraft. This voltage can be determined by calculating or assuming a value for the inductive impedance of the seam. Formally it is given by,

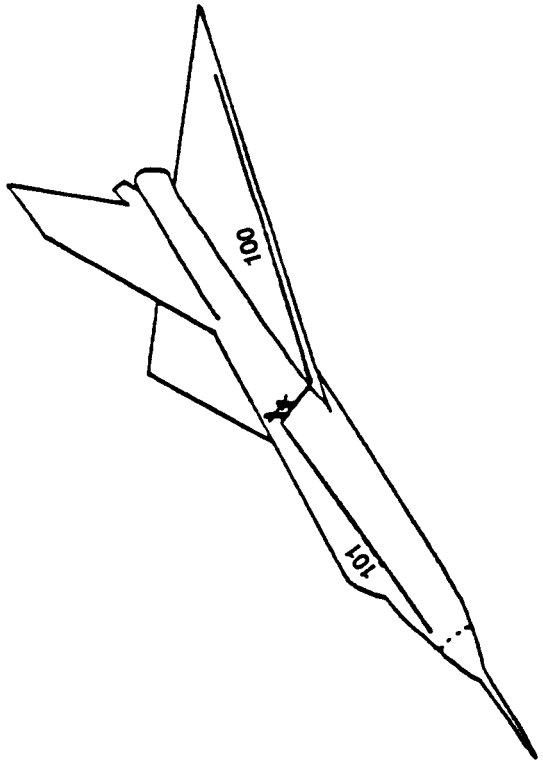
$$V = L \frac{dj}{dt} \quad (4.2)$$

where  $V$  is the internal voltage generated at the seam,  $L$  is the inductive coupling coefficient for the seam, and  $j$  is the external current density across the seam.

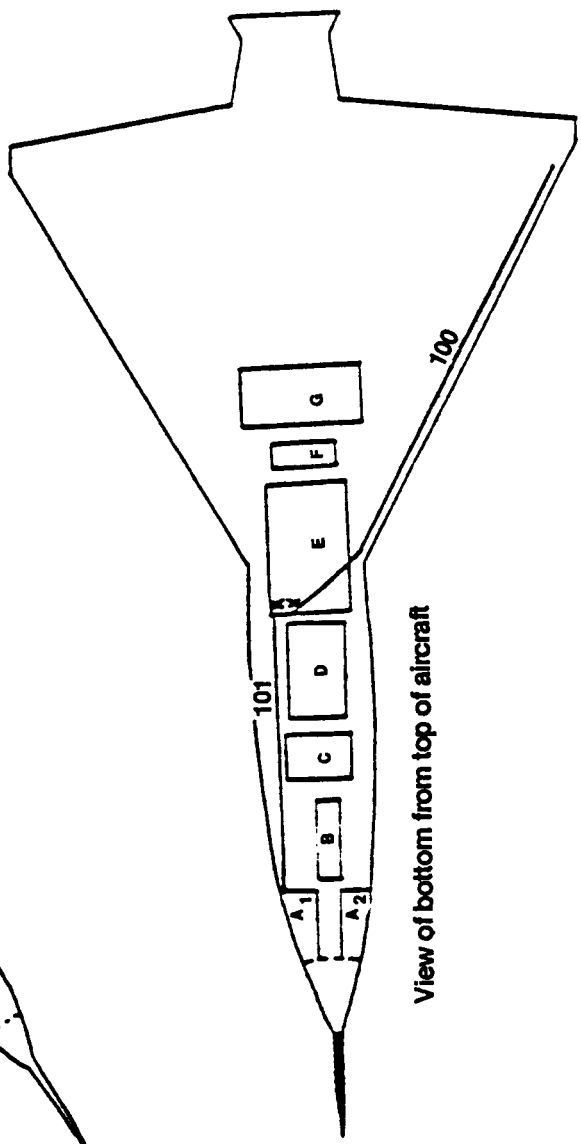
For each of the sixty-five cases analyzed in Section 4.2, an internal coupling calculation was also done. Fuselage and wing wires were modeled and their voltage responses compared to the actual measured responses. Wire voltages were also predicted for those lightning events for which wire responses were not recorded or the sensors did not function properly. The arrangement of these particular wires with respect to the F106B is shown in Figure 4.5. The wires are described as insulated, 22-gauge wires. The wing wire (test point #100) is grounded near the left wing tip and routed inside the leading edge of the wing to the instrument bay. The fuselage wire (test point #101) is grounded to the radome bulkhead and routed along the right inside of the fuselage to the instrument bay. Both wires are terminated in 50 ohms.

The wire responses are calculated by modeling the internal wire as a transmission line illuminated at various points along its length by electric field sources. These sources are calculated from the voltage driver of equation (4.2), which in turn is derived from external currents calculated by the F106B finite difference code and an assumption about the inductive coupling coefficient of the seams. The transmission line model of the internal wire allows the wire to have varying inductance and capacitance per unit length. In practice, however, because the wires of interest were in large wire bundles and the detailed routing was difficult to follow, a single capacitance per unit length was used at all points on the wire. Table 4.1 shows the parameters used in the two wire models.

#	Type of Probe	Test Point Location	Wire Location
100	COP-1	Instrumentation Package	From weapons bay along leading edge of left wing tip.
101	COP-1	Instrumentation Package	From weapons bay along right side of aircraft to radome bulkhead.



- A<sub>1</sub> Right forward electronics compartment
- A<sub>2</sub> Left forward electronics compartment
- B Nose wheel well
- C O5 Compartment
- D Coffin
- E Missile bay (Instrumentation package)
- F Hydraulic compartment
- G Main landing gear wheel well



View of bottom from top of aircraft

Figure 4.5 Fuselage and Wing Wire Configuration in the F106B

**Table 4.1  
Parameters Used in the Transmission Line Models of Internal  
F106B Wires**

<b>Parameter</b>	<b>Fuselage Wire</b>	<b>Wing Wire</b>
Length	9 meters	13.5 meters
Cell Size	.5 meters	.5 meters
External Field Source Coupling Locations	Front and back seams at wheel well door; Front seam at instrument bay door	Front and left side seams at the instrument bay door <sup>1</sup>
Best Fit Averaged Inductive Transfer Impedance (L) <sup>2</sup>	7.7 nH-m (for all 3 seams)	2.0 nH-m (for both seams)
Propagation Velocity for Insulated Wire	$2 \times 10^8$ m/sec	$2 \times 10^8$ m/sec
Wire Impedance	50 ohms	50 ohms
Wire Capacitance per Unit Length	$1 \times 10^{-10}$ f/m	$1 \times 10^{-10}$ f/m
Wire Inductance per Unit Length	$2.5 \times 10^{-7}$ H/m	$2.5 \times 10^{-7}$ H/m
Terminations	Shorted at forward bulkhead; terminated in 50 ohms in the instrument bay	Shorted at left wing tip; terminated in 50 ohms in the instrument bay

**Notes:**

1. The wing wire was assumed to cross the front and left side seams of instrument bay door at 40 and 50 degree angles, respectively.
2. The inductive transfer impedances (L) of these seams are unknown. A best fit value was determined and used for all the wire computer runs. It is likely that in reality the impedance of these seams changes from flight to flight as the doors are opened and closed

In the figures to follow, each internal wire response was calculated for a triggered lightning channel attached at the nose of the F106B and an exit channel at the tail. Figures 4.6(a) - 4.6(f) show the internal wire voltage across the 50 ohm termination for the cases in which both a measured and predicted waveform are available. Figures 4.7(a) - 4.7(t) show the predicted wire voltages for the cases in which a measured response was unavailable. Figure 4.8 shows the predicted wire voltages for a possible multiple strike event. In this case, the model was run to 2 microseconds.

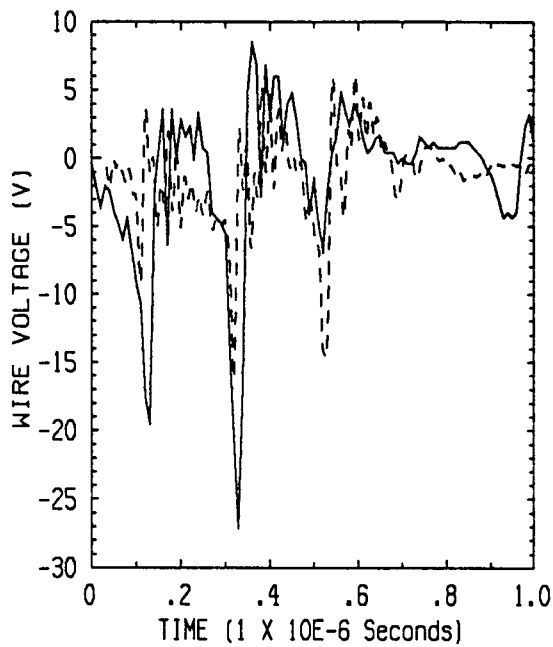
Some general comments may be made about the comparisons between measured and predicted internal wire voltages. Many of the waveshapes match quite closely, while magnitudes tend to vary more, sometimes by as much as a factor of two. However, it is important to note that an averaged value for the inductive transfer impedance,  $L$ , was used for all fuselage wire models, and another averaged value for all wing wire models. It is likely that  $L$  can change from flight to flight, as the doors are opened and closed. A factor of two variation in magnitude then is not surprising. This is supported by the observation that the predicted responses vary from the measured responses by approximately the same percentage for all strikes occurring on a given flight.

The largest waveform differences generally appear in the response of the wing wire. In particular there are higher frequencies in the predicted response than in the measured. These frequencies are related to the length of the wire and correspond to reflections, occurring probably on the shorted end of the wire. The fact that these do not appear in the measured waveforms may be because of the mutual effects of the cable bundles in which the test wire is located. The behavior of a single wire within a large bundle of variously sized and terminated wires may be significantly different than the behavior of an isolated wire, particularly at the higher frequencies.

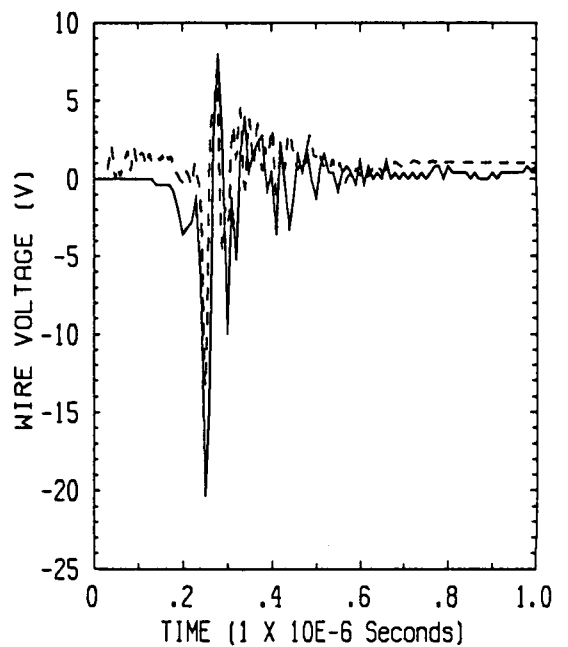
Based on the 1984 flight data, the fuselage and wing wire voltages vary in the range  $\pm 35$  V and  $\pm 5$  V, respectively, as upper limits. Most of the fuselage wire voltages are in the range  $\pm 15$  V, while the majority of wing wire voltages are in the range  $\pm 1.5$  V. These latter numbers correspond to typical  $B\text{-dot}$  longitudinal values of  $\pm 1500$  T/s and  $D\text{-dot}$  forward values of  $\pm 15$  A/square meter. Typical peak current magnitudes are in the range of  $\pm 1000$  amperes, but a few strikes were seen to have peaks as high as  $\pm 2000$  amperes or larger.

(text continued on page 93)

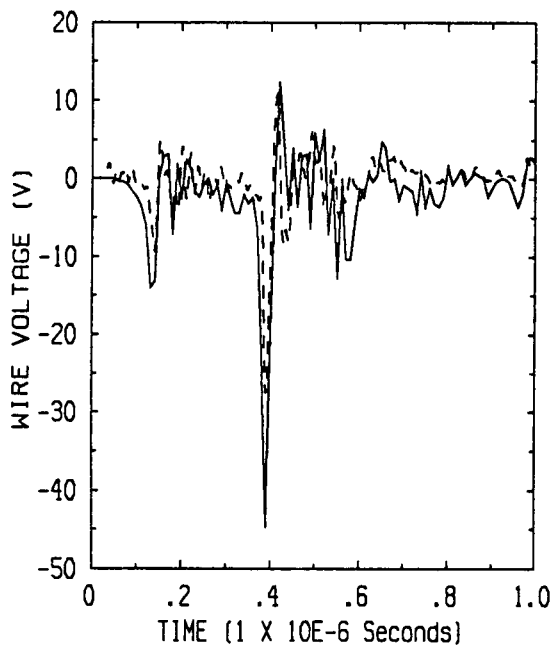




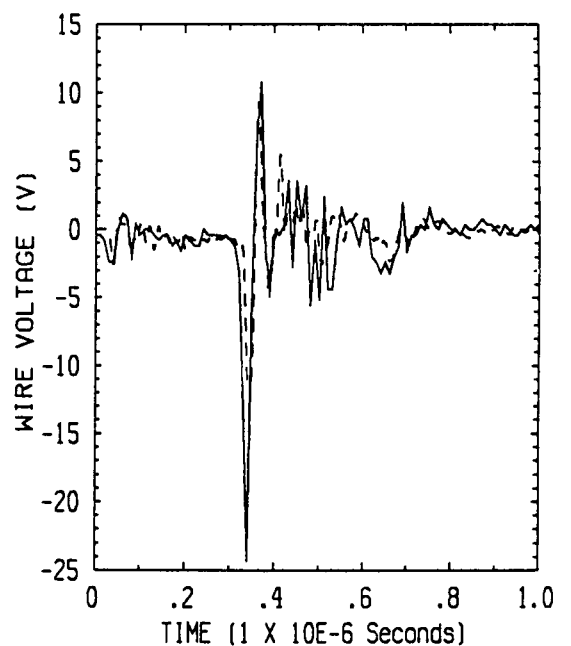
FUSELAGE WIRE VOLTAGES  
 - MEASURED; -- PREDICTED  
 Flight 84-014, run 002, strike 002



FUSELAGE WIRE VOLTAGES  
 - MEASURED; -- PREDICTED  
 Flight 84-015, run 001, strike 001

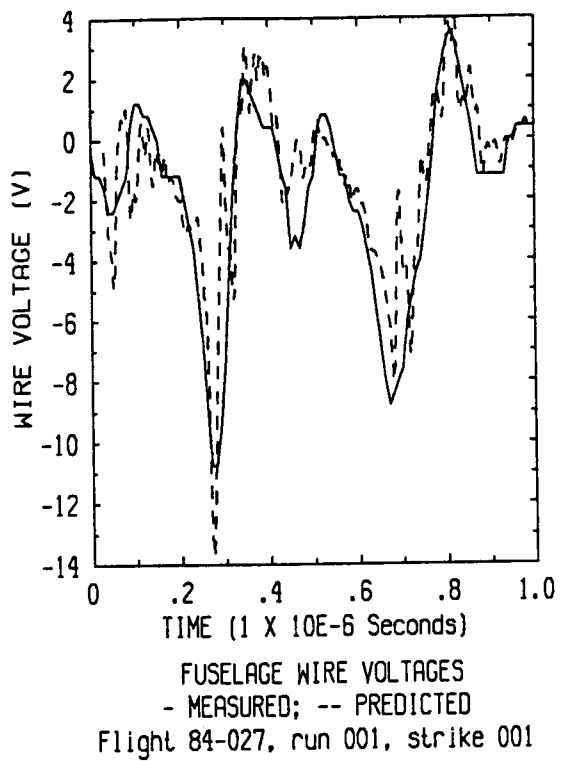
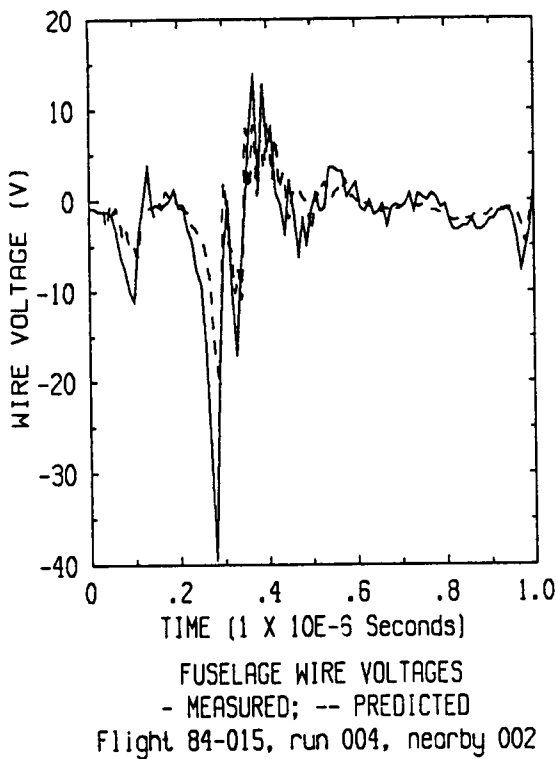


FUSELAGE WIRE VOLTAGES  
 - MEASURED; -- PREDICTED  
 Flight 84-015, run 002, strike 002



FUSELAGE WIRE VOLTAGES  
 - MEASURED; -- PREDICTED  
 Flight 84-015, run 003, strike 001

**Figure 4.6(a) Measured versus Predicted Internal Wire Responses**



(Note: This labeled nearby event is now suspected to have been a direct strike)

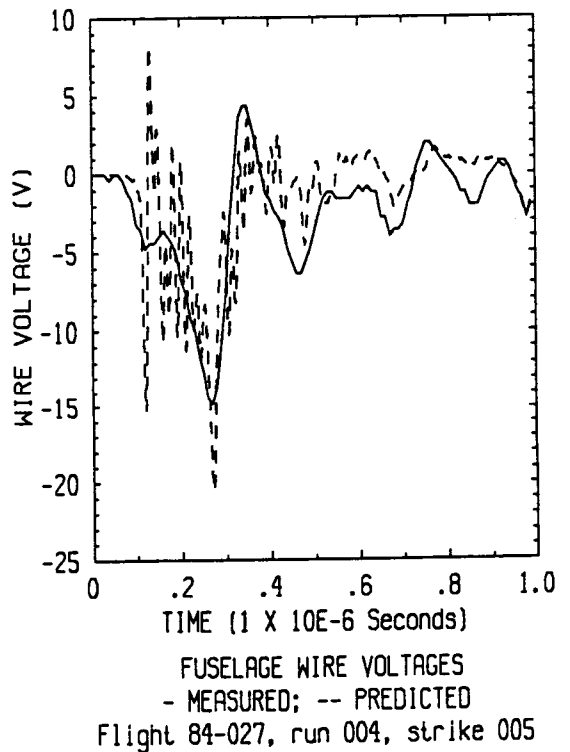
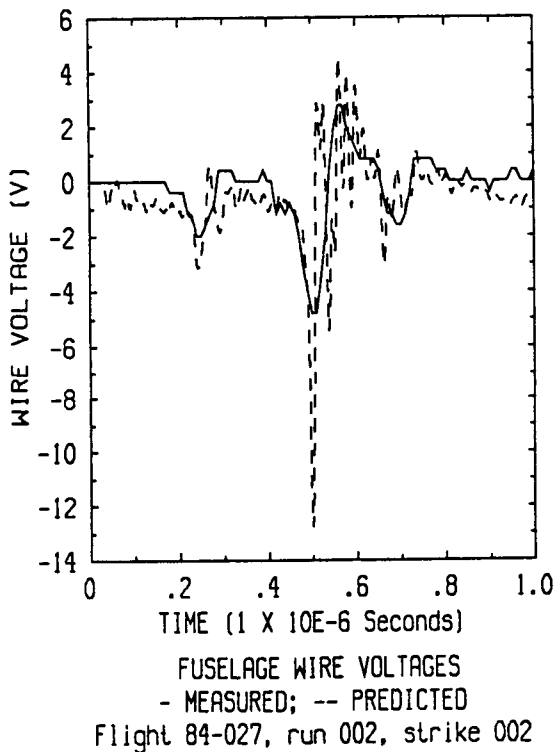
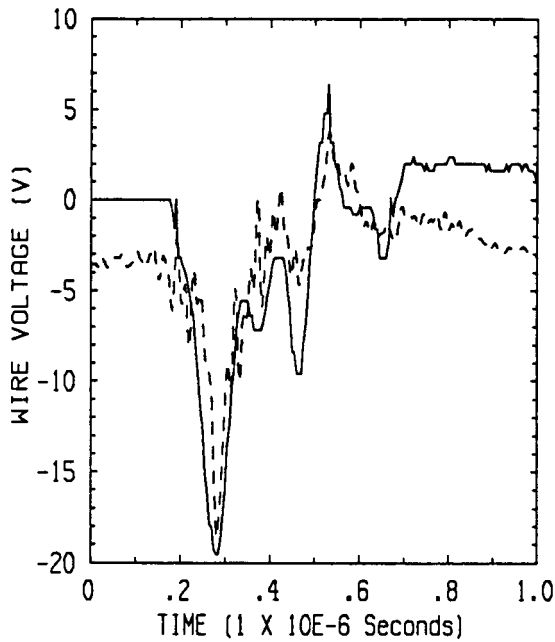
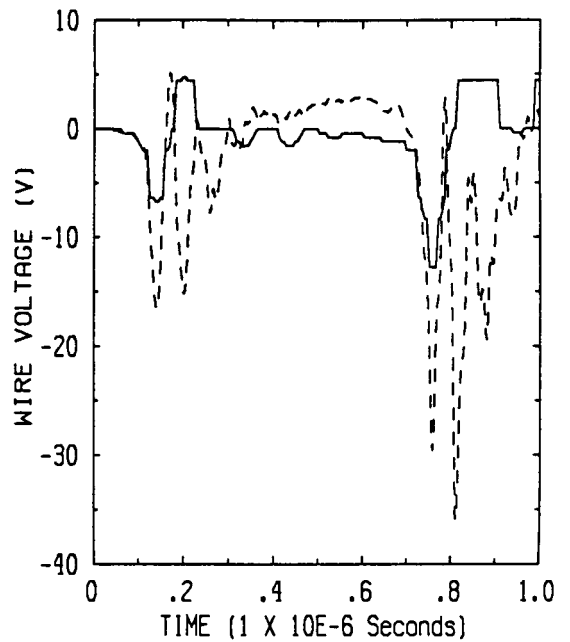


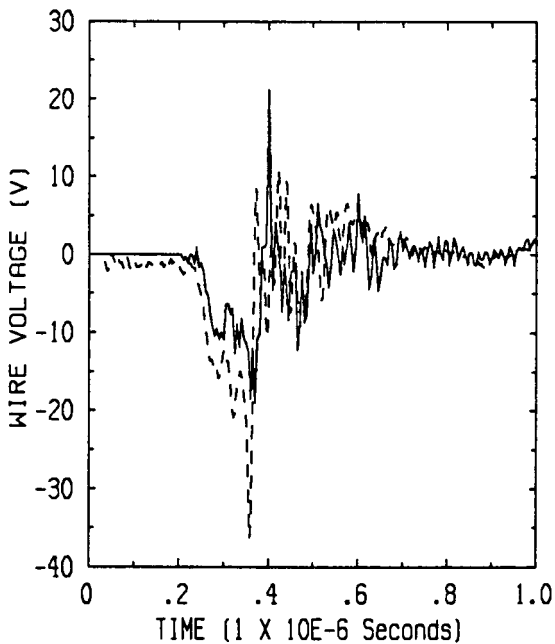
**Figure 4.6(b) Measured versus Predicted Internal Wire Responses**



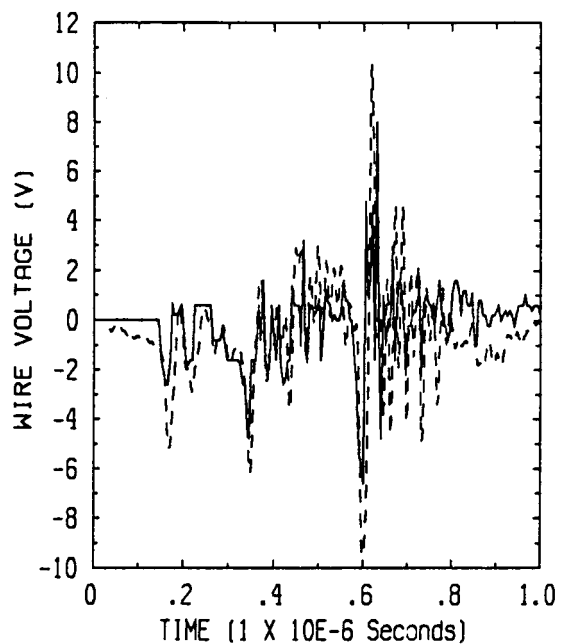
FUSELAGE WIRE VOLTAGES  
 - MEASURED; -- PREDICTED  
 Flight 84-035, run 001, strike 001



FUSELAGE WIRE VOLTAGES  
 - MEASURED; -- PREDICTED  
 Flight 84-037, run 008, strike 041

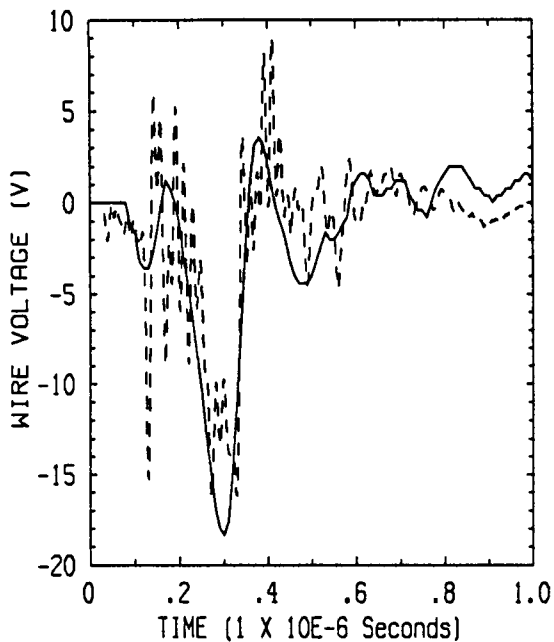


FUSELAGE WIRE VOLTAGES  
 - MEASURED; -- PREDICTED  
 Flight 84-042, run 001, strike 001

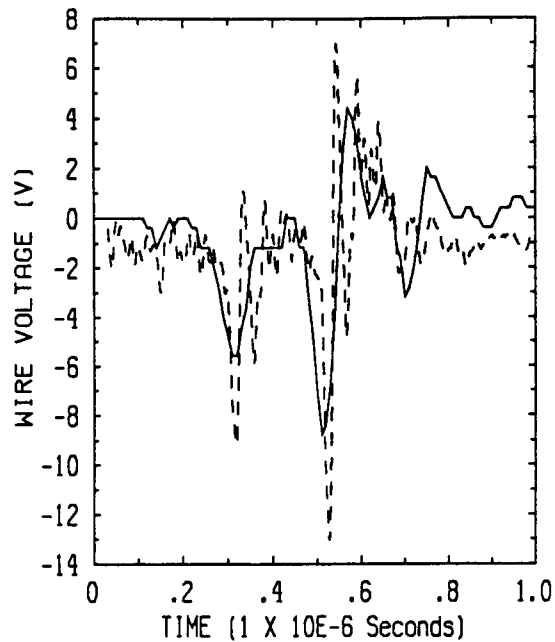


FUSELAGE WIRE VOLTAGES  
 - MEASURED; -- PREDICTED  
 Flight 84-042, run 003, strike 003

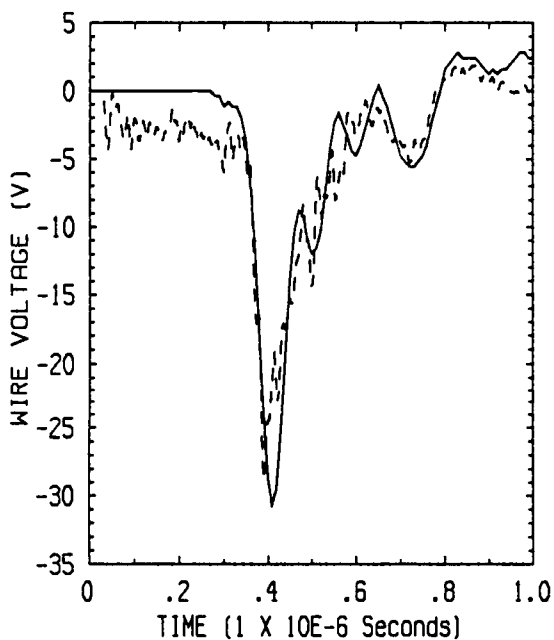
**Figure 4.6(c) Measured versus Predicted Internal Wire Responses**



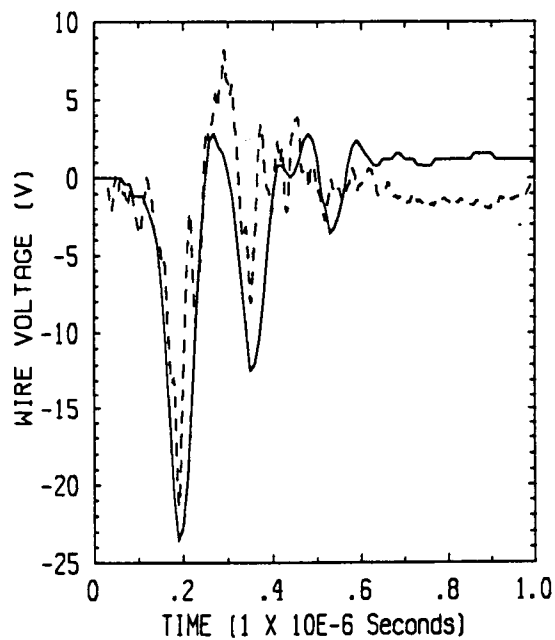
FUSELAGE WIRE VOLTAGES  
 - MEASURED; -- PREDICTED  
 Flight 84-027, run 005, strike 006



FUSELAGE WIRE VOLTAGES  
 - MEASURED; -- PREDICTED  
 Flight 84-029, run 001, strike 001

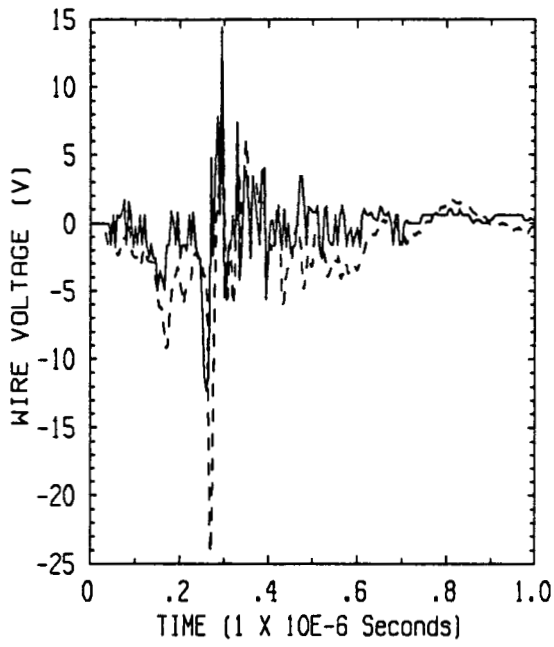


FUSELAGE WIRE VOLTAGES  
 - MEASURED; -- PREDICTED  
 Flight 84-032, run 002, strike 003

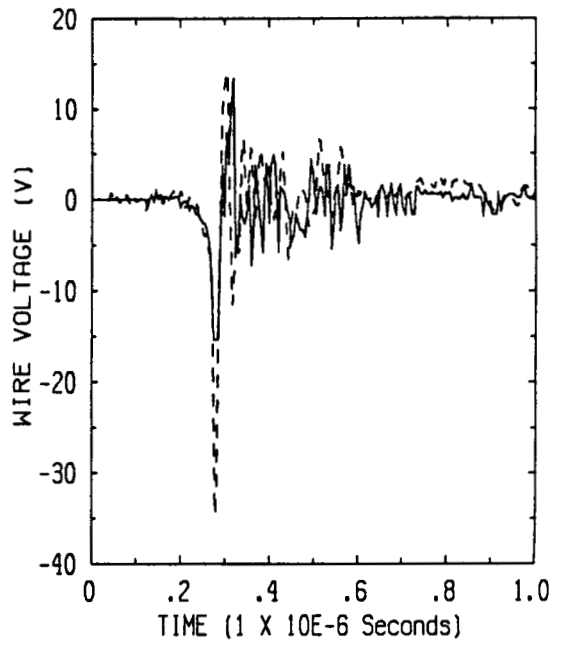


FUSELAGE WIRE VOLTAGES  
 - MEASURED; -- PREDICTED  
 Flight 84-032, run 003, strike 005

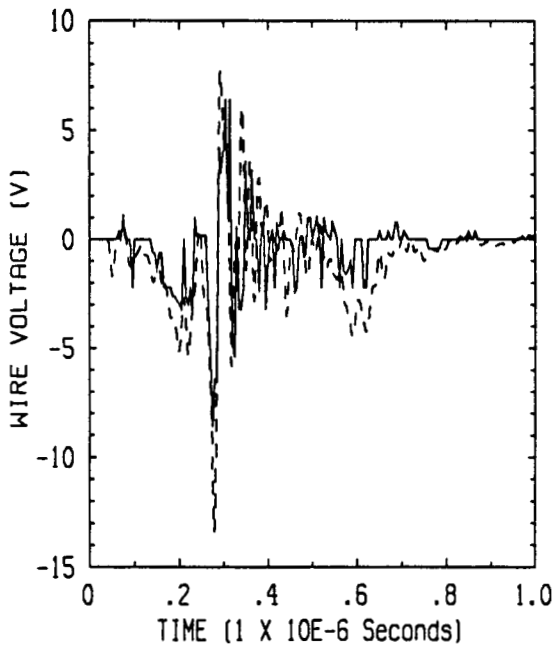
**Figure 4.6(d) Measured versus Predicted Internal Wire Responses**



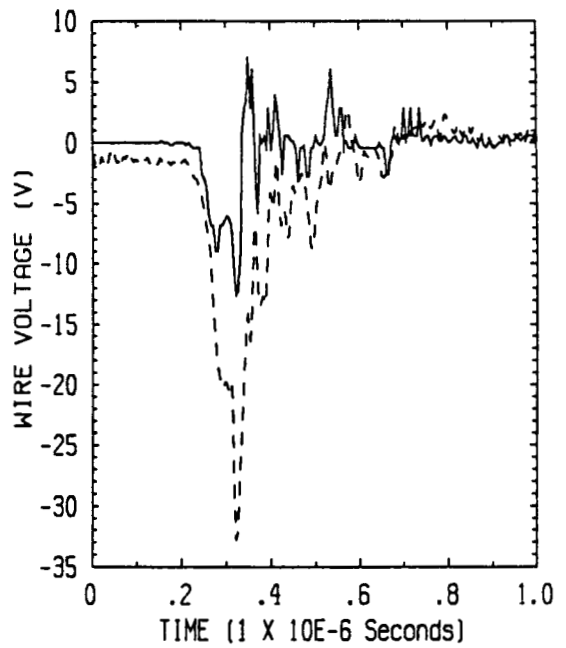
FUSELAGE WIRE VOLTAGES  
 - MEASURED; -- PREDICTED  
 Flight 84-042, run 005, strike 005



FUSELAGE WIRE VOLTAGES  
 - MEASURED; -- PREDICTED  
 Flight 84-043, run 002, strike 003

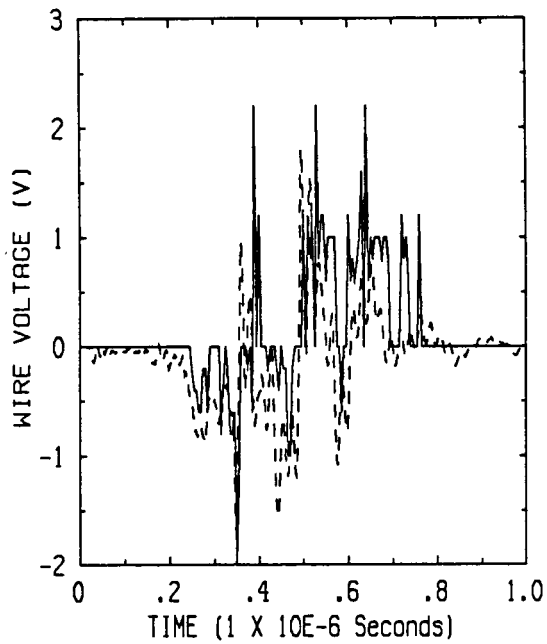


FUSELAGE WIRE VOLTAGES  
 - MEASURED; -- PREDICTED  
 Flight 84-043, run 003, strike 004

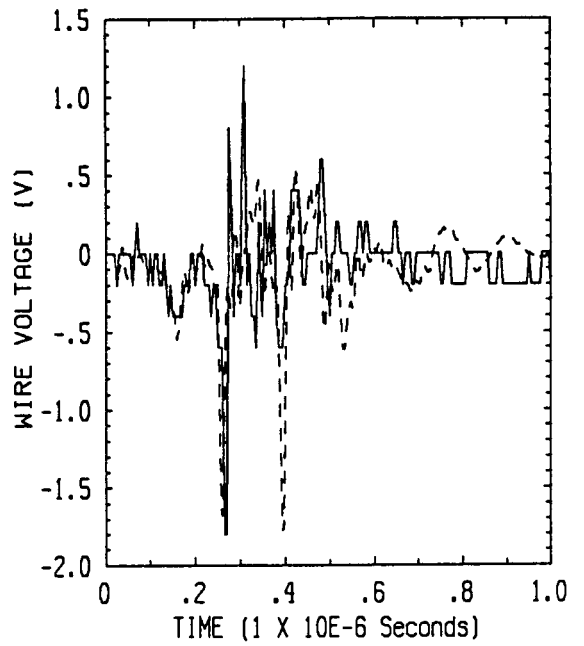


FUSELAGE WIRE VOLTAGES  
 - MEASURED; -- PREDICTED  
 Flight 84-050, run 002, strike 002

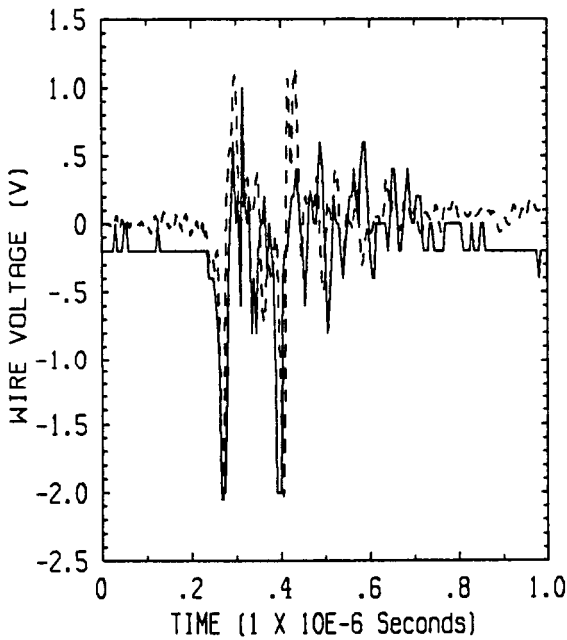
**Figure 4.6(e) Measured versus Predicted Internal Wire Responses**



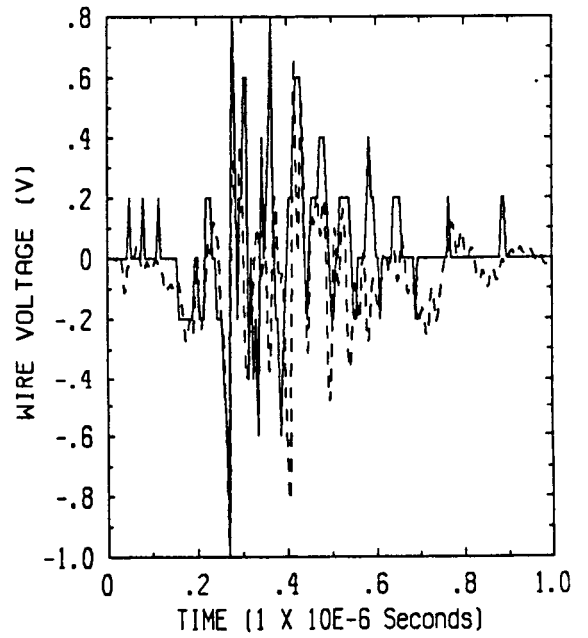
WING WIRE VOLTAGES  
 - MEASURED; -- PREDICTED  
 Flight 84-042, run 001, strike 001



WING WIRE VOLTAGES  
 - MEASURED; -- PREDICTED  
 Flight 84-042, run 005, strike 005

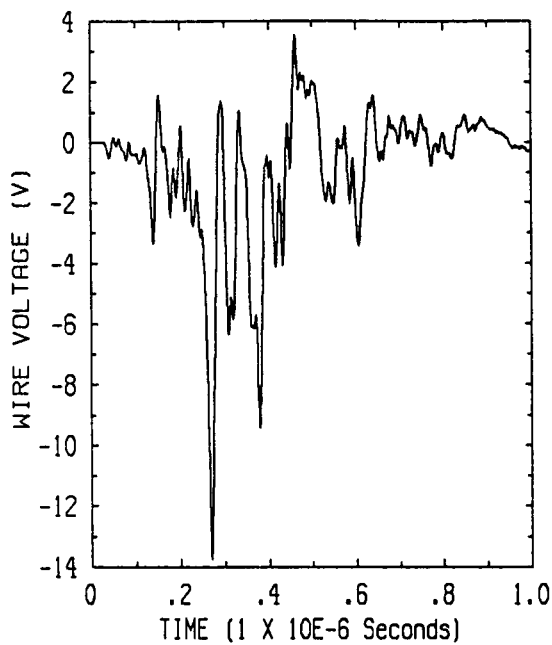


WING WIRE VOLTAGES  
 - MEASURED; -- PREDICTED  
 Flight 84-043, run 002, strike 003

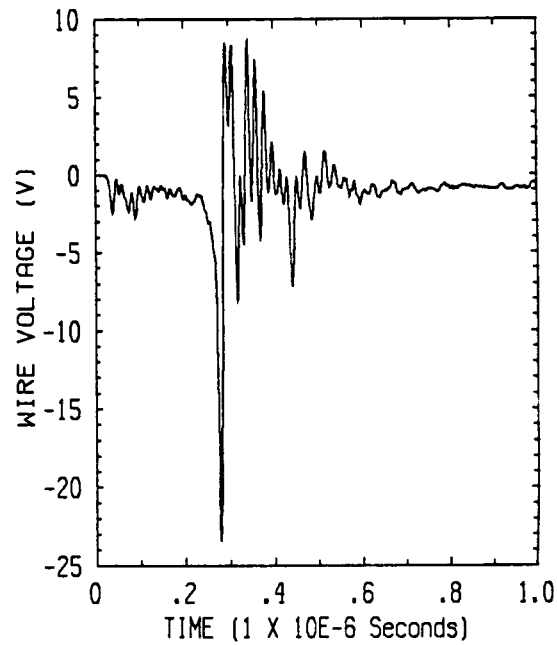


WING WIRE VOLTAGES  
 - MEASURED; -- PREDICTED  
 Flight 84-043, run 003, strike 004

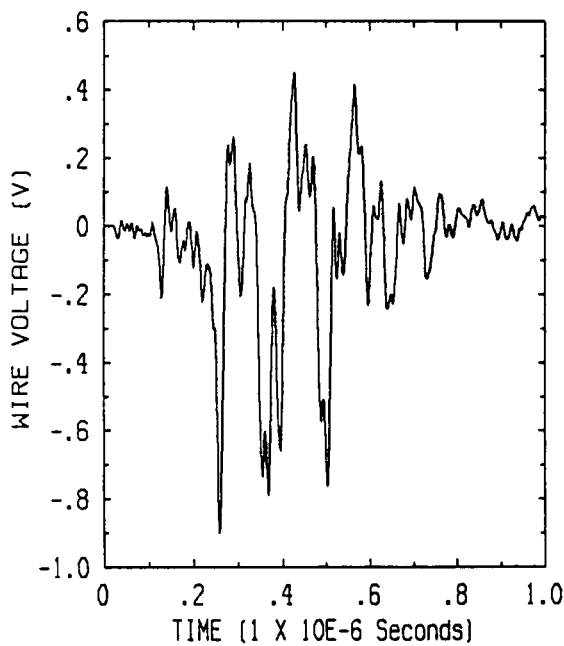
**Figure 4.6(f) Measured versus Predicted Internal Wire Responses**



PREDICTED FUSELAGE WIRE VOLTAGE

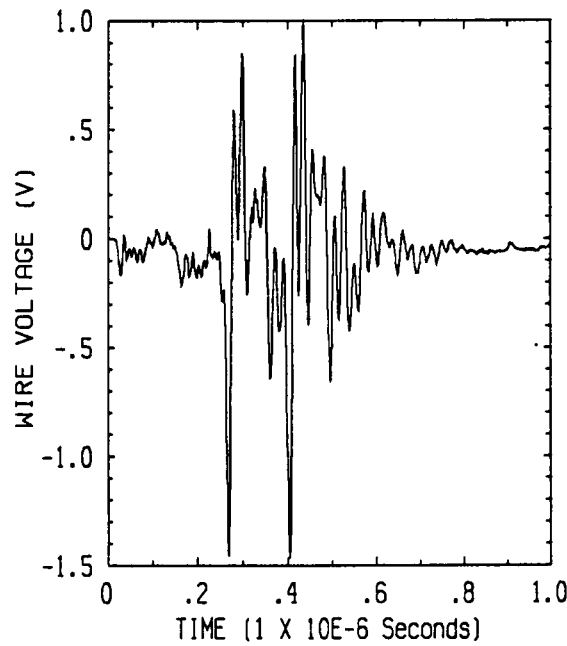


PREDICTED FUSELAGE WIRE VOLTAGE



PREDICTED WING WIRE VOLTAGE

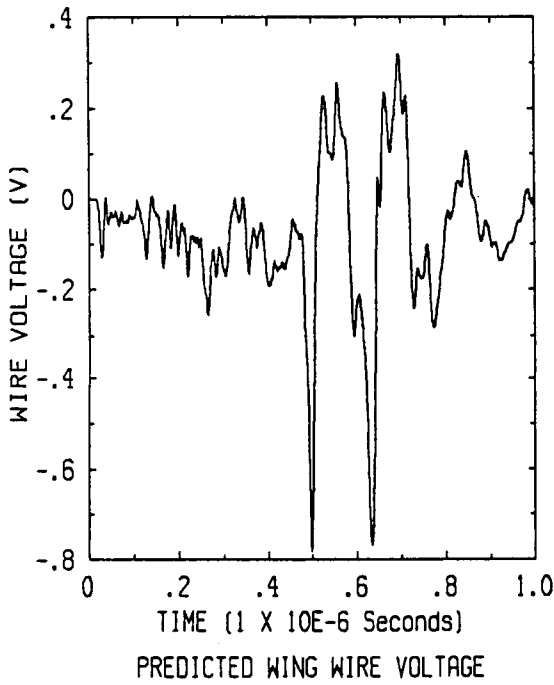
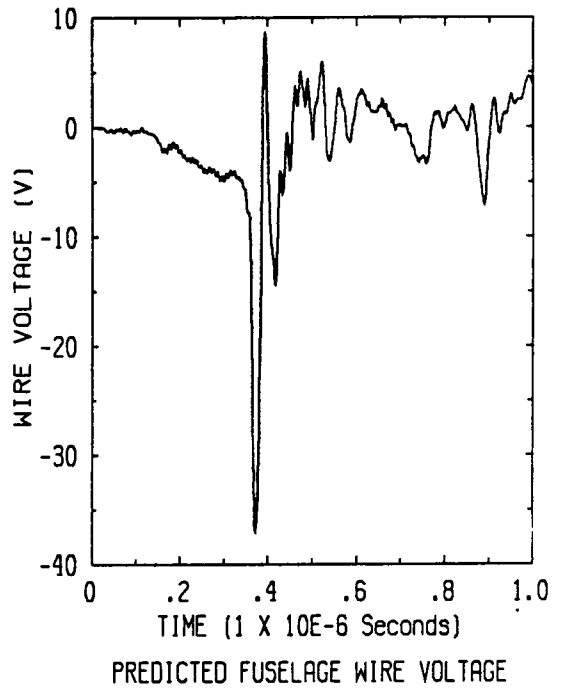
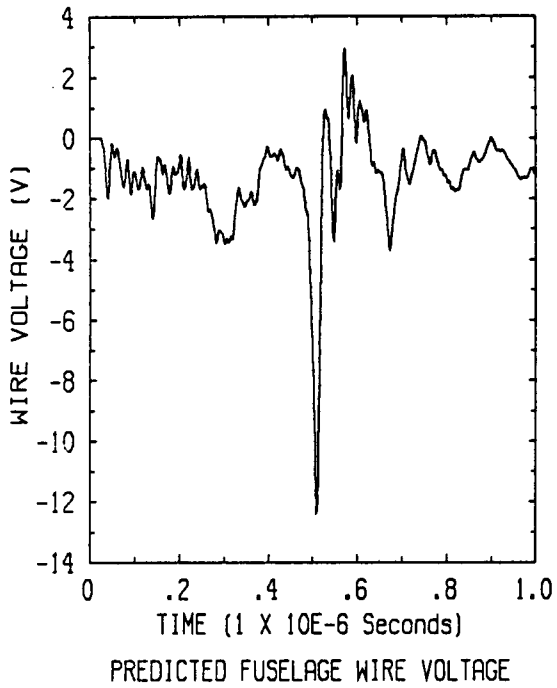
Flight 84-021, run 001, strike 001



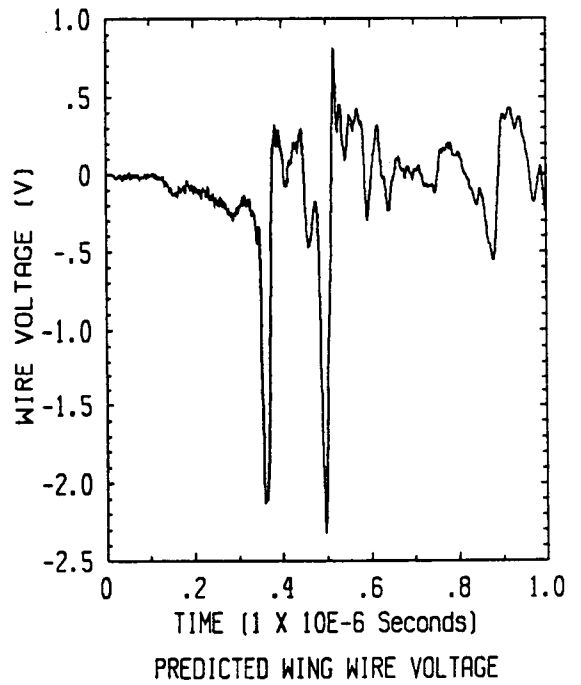
PREDICTED WING WIRE VOLTAGE

Flight 84-021, run 003, strike 001

**Figure 4.7(a) Predicted Internal Wire Responses**



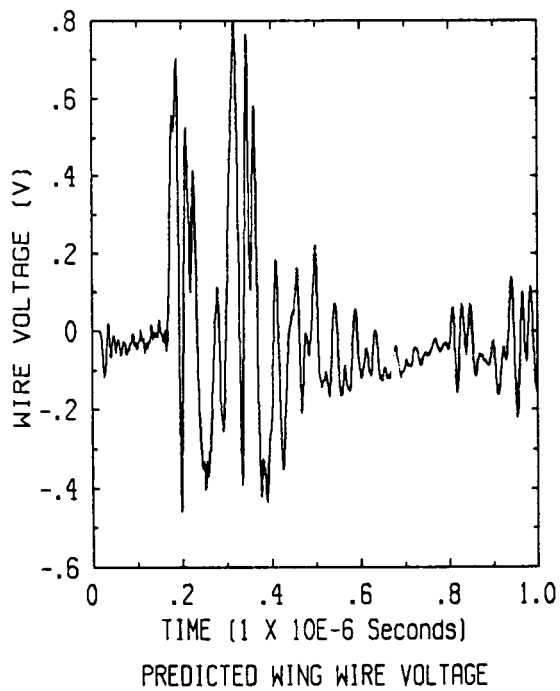
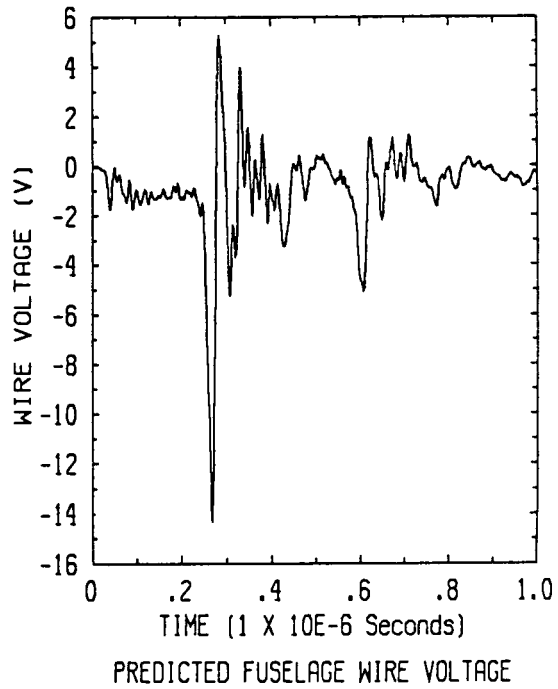
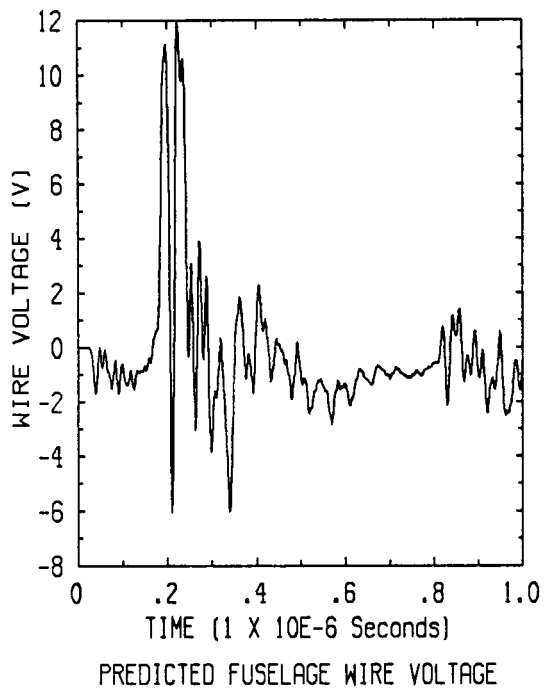
Flight 84-024, run 001, strike 001



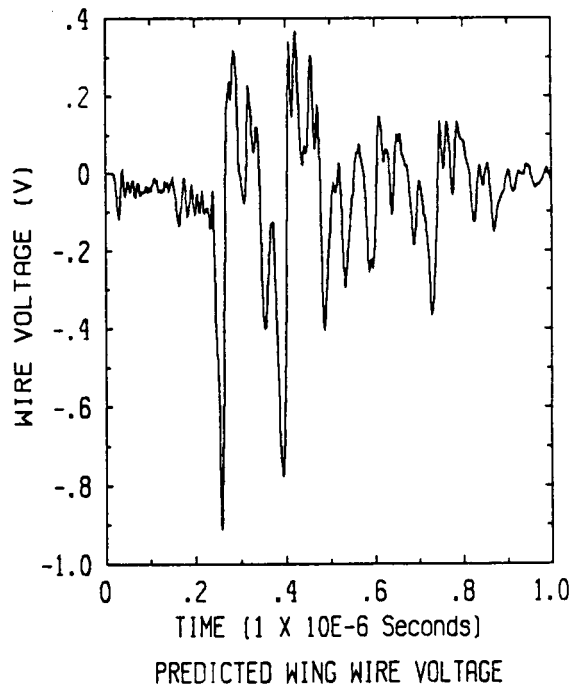
Flight 84-024, run 003, strike 003

**Figure 4.7(b) Predicted Internal Wire Responses**



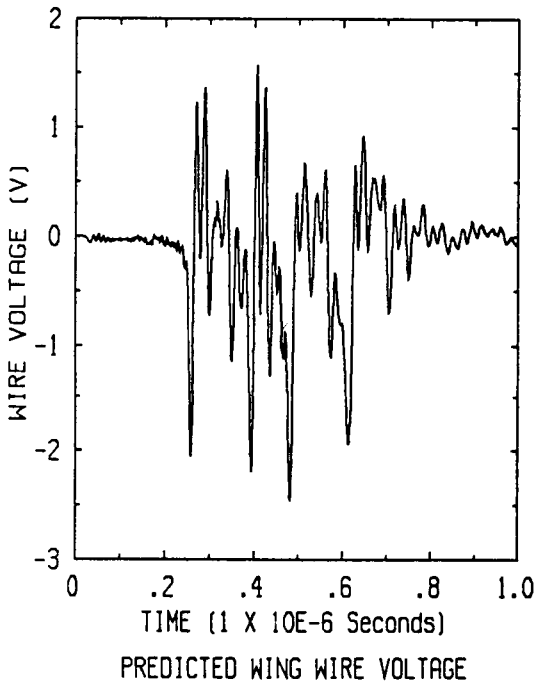
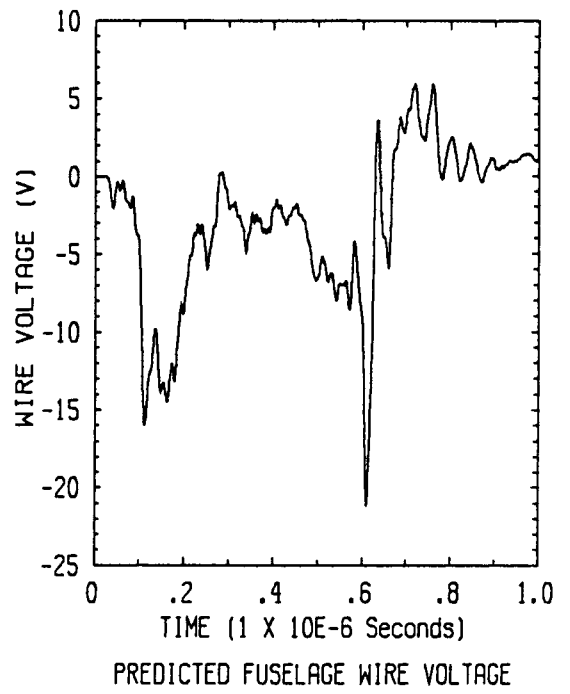
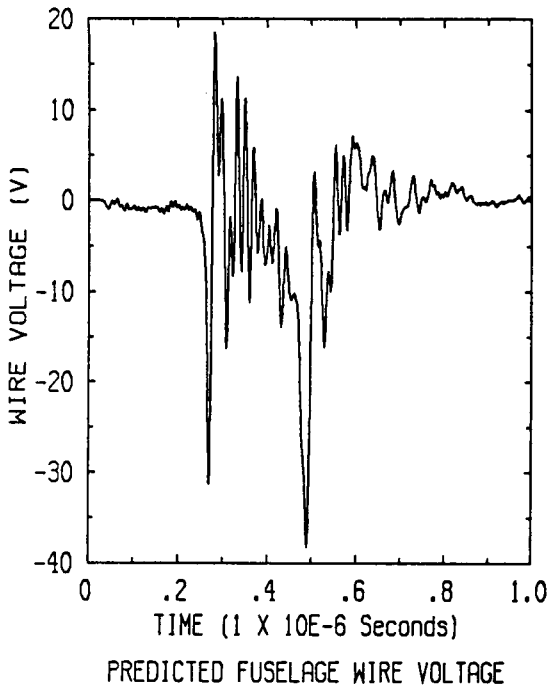


Flight 84-025, run 001, strike 001

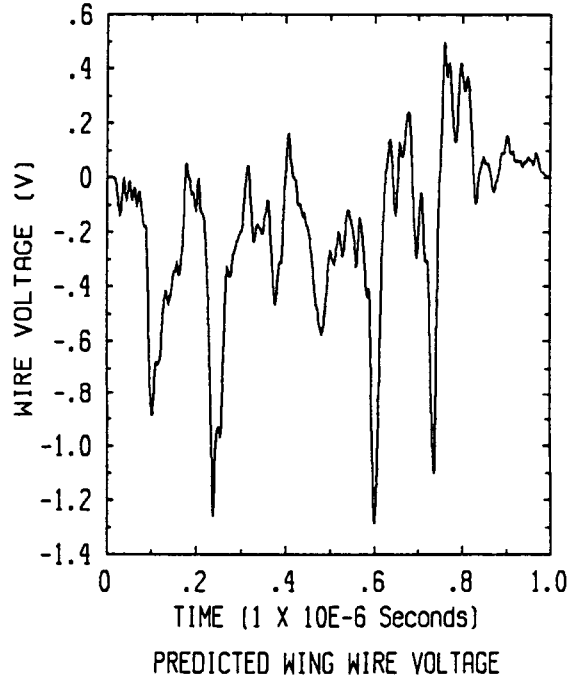


Flight 84-025, run 002, strike 003

**Figure 4.7(c) Predicted Internal Wire Responses**

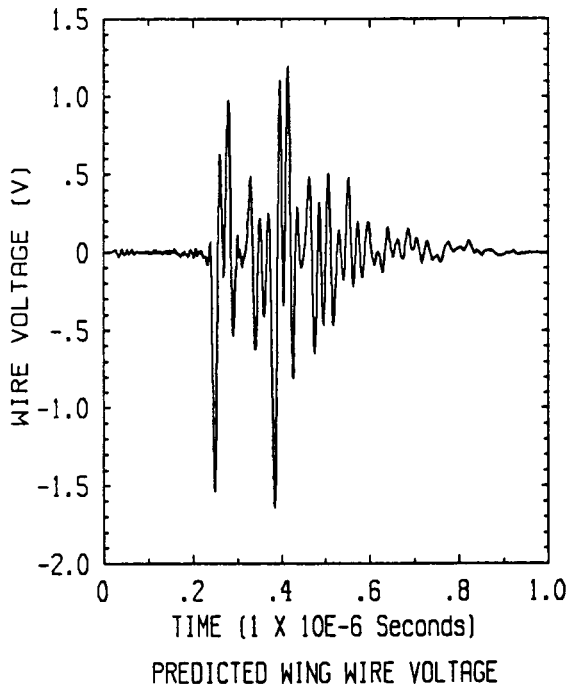
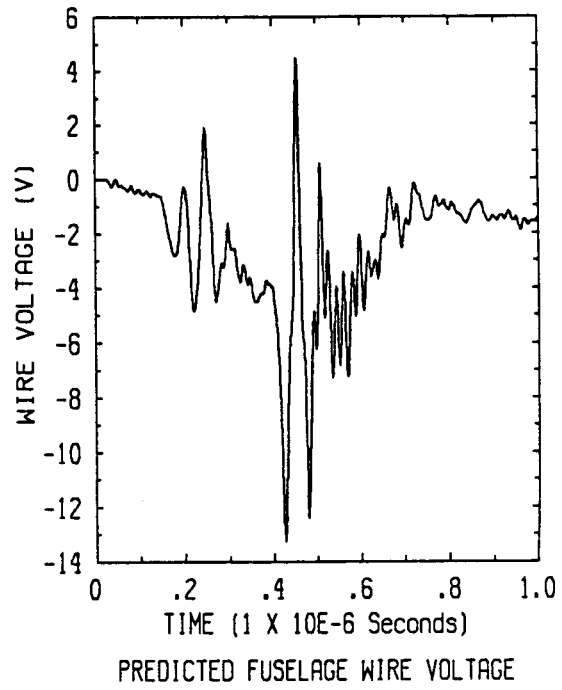
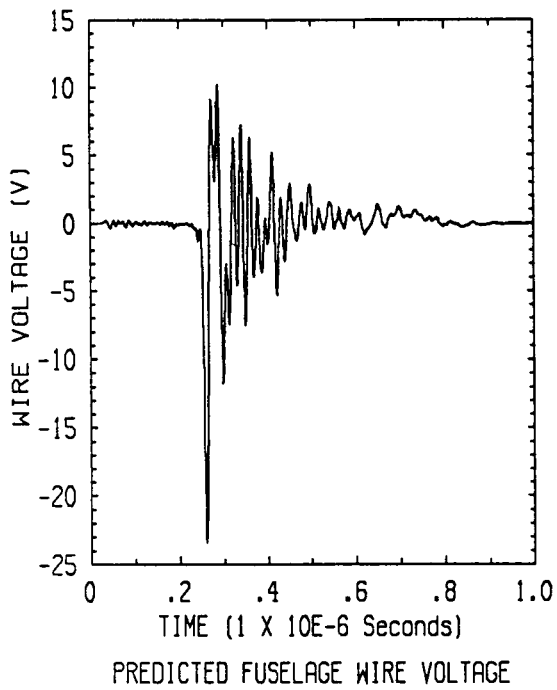


Flight 84-025, run 003, strike 004

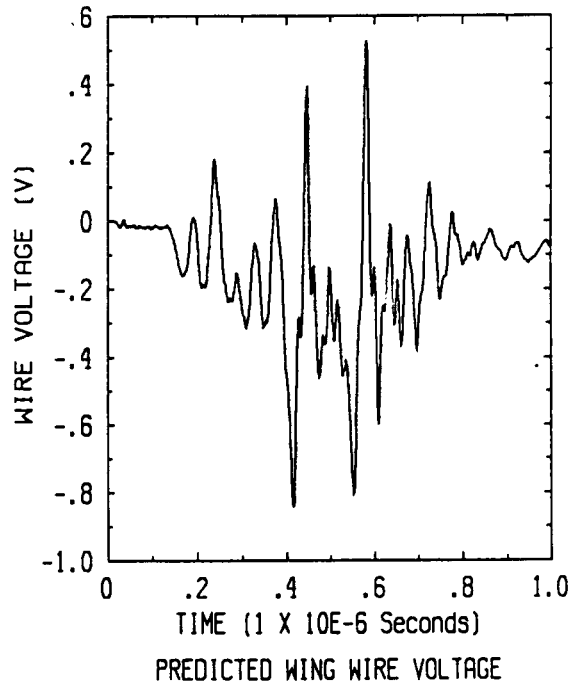


Flight 84-025, run 004, strike 005

**Figure 4.7(d) Predicted Internal Wire Responses**

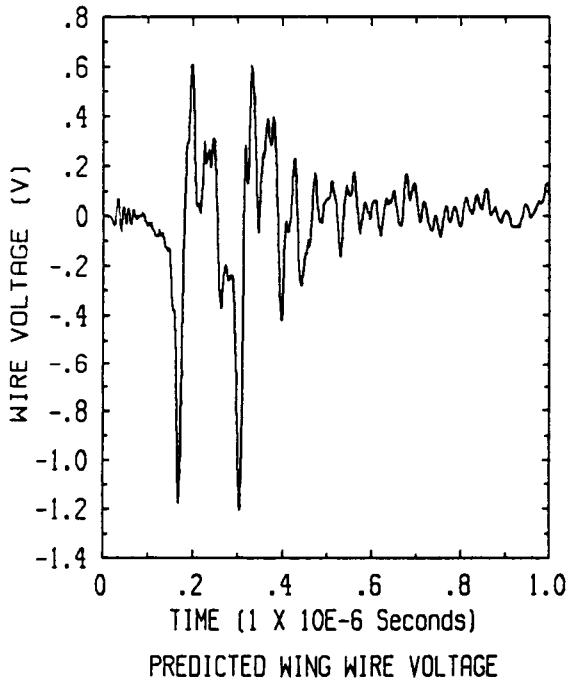
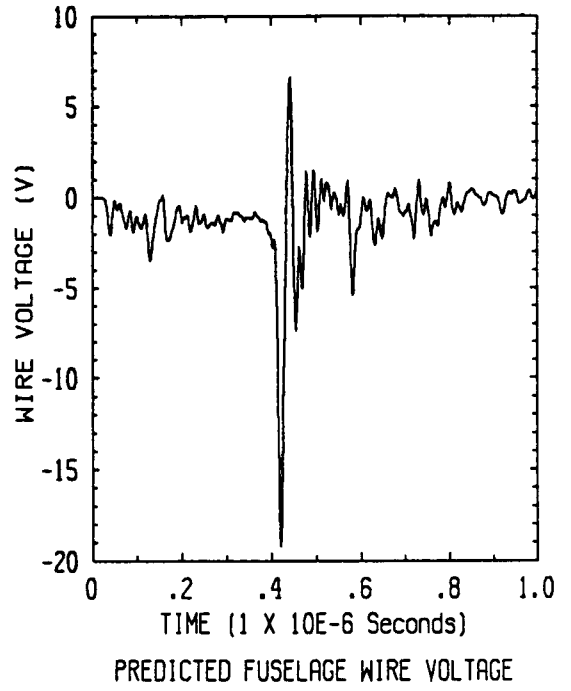
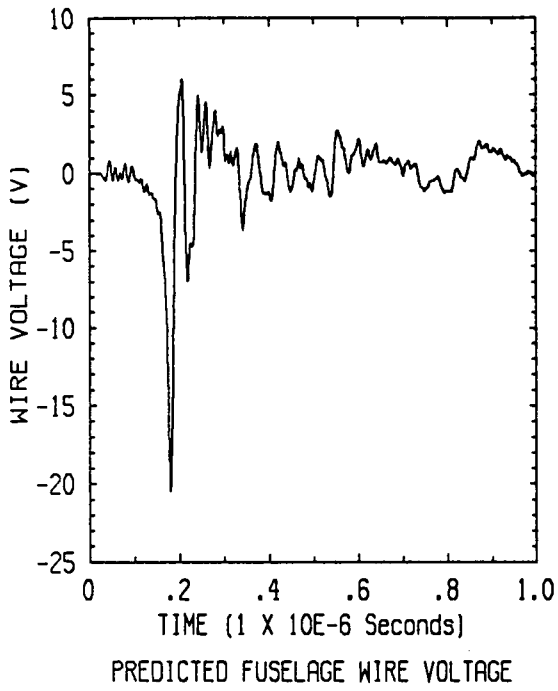


Flight 84-025, run 007, strike 010

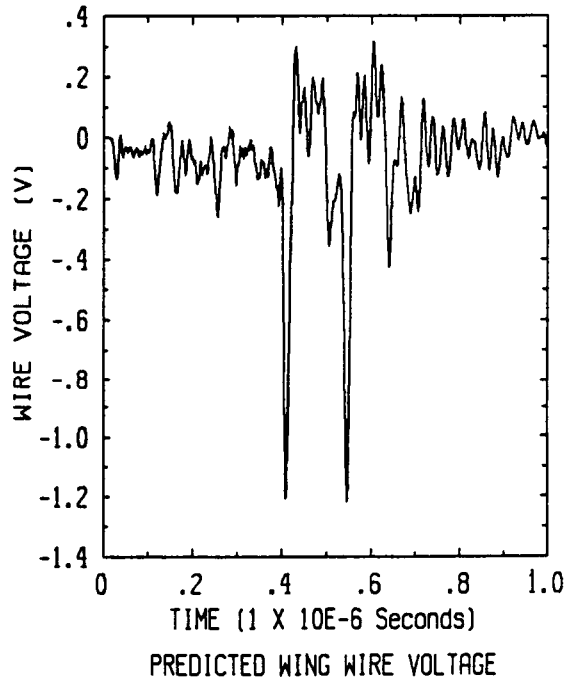


Flight 84-025, run 008, strike 011

**Figure 4.7(e) Predicted Internal Wire Responses**

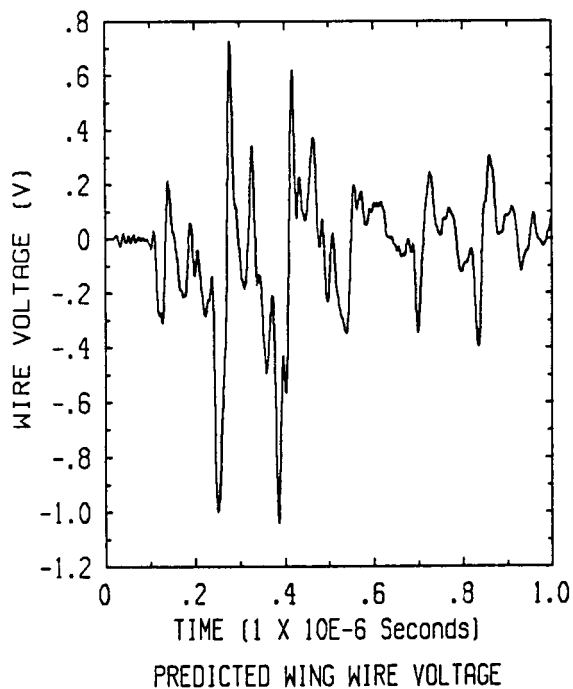
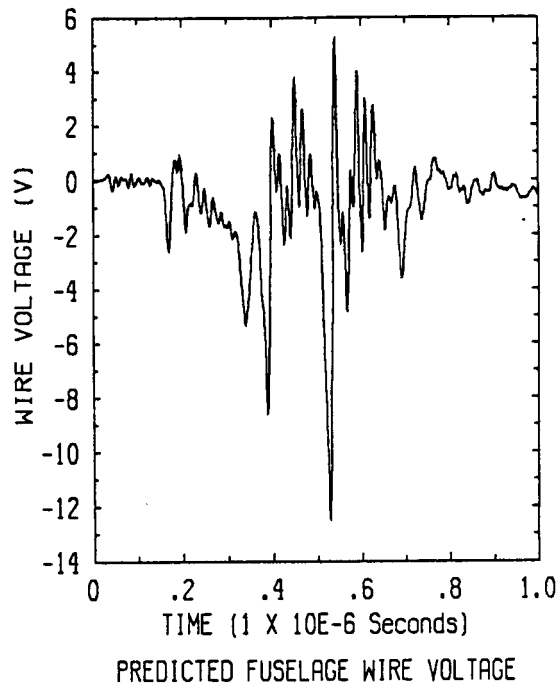
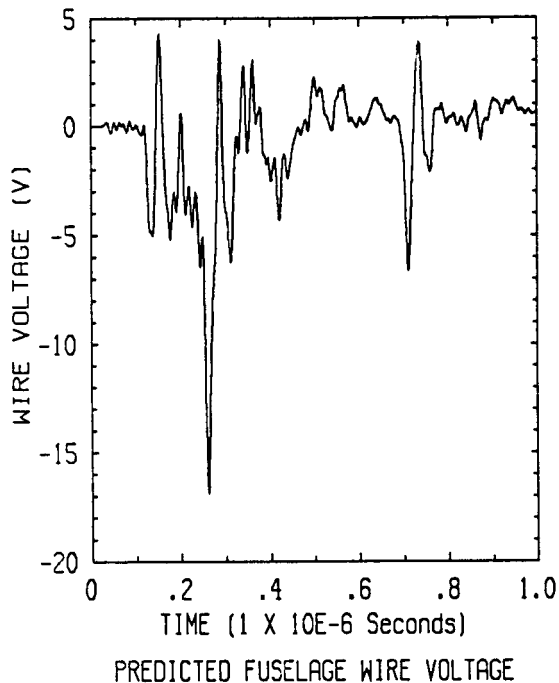


Flight 84-025, run 011, strike 014

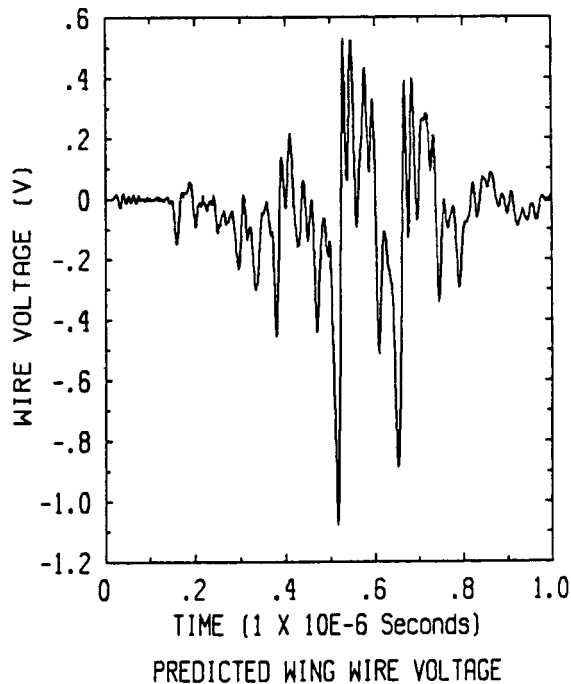


Flight 84-025, run 013, strike 017

**Figure 4.7(f) Predicted Internal Wire Responses**

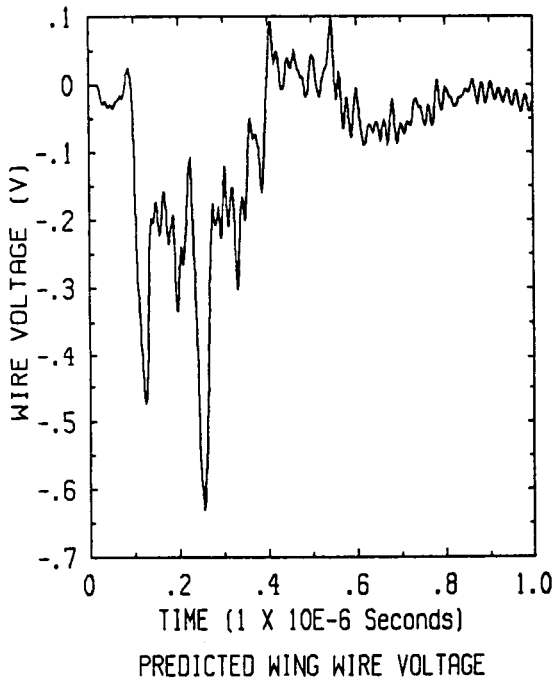
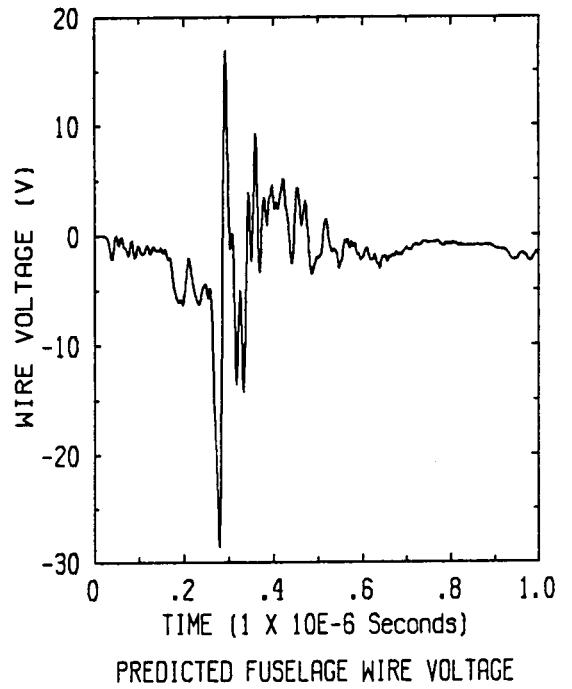
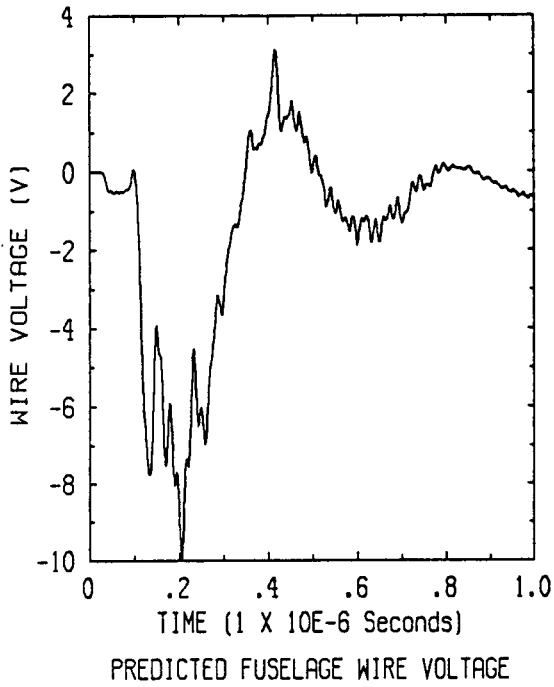


Flight 84-025, run 015, strike 019

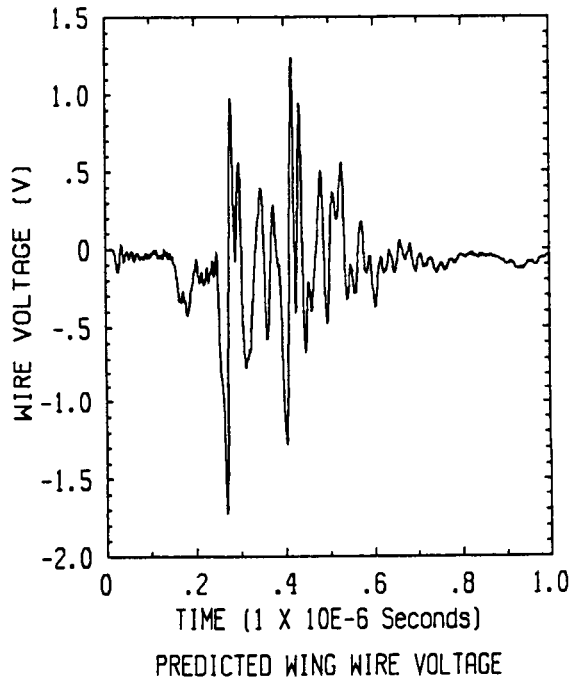


Flight 84-027A, run 001, strike 001

**Figure 4.7(g) Predicted Internal Wire Responses**

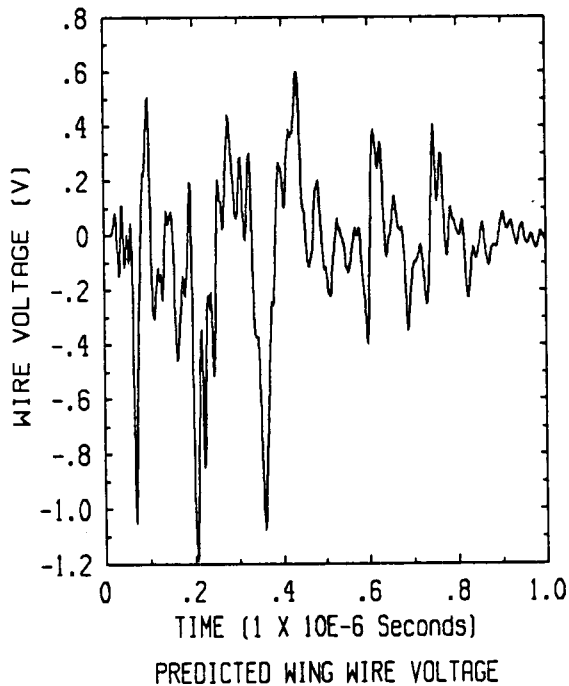
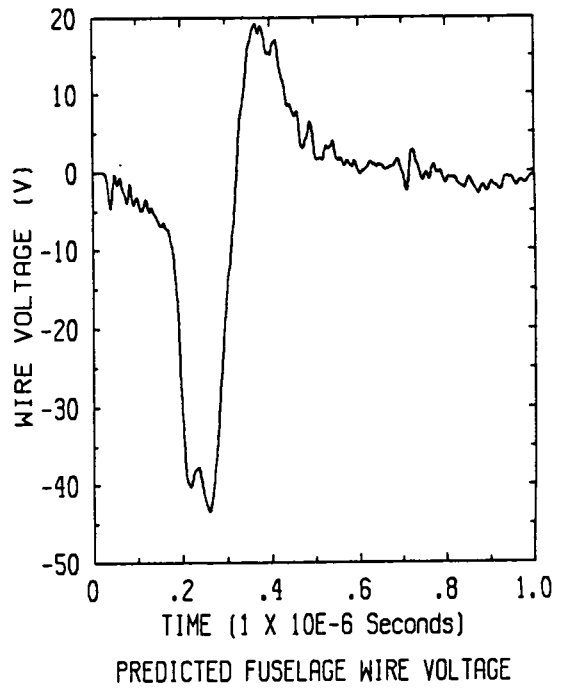
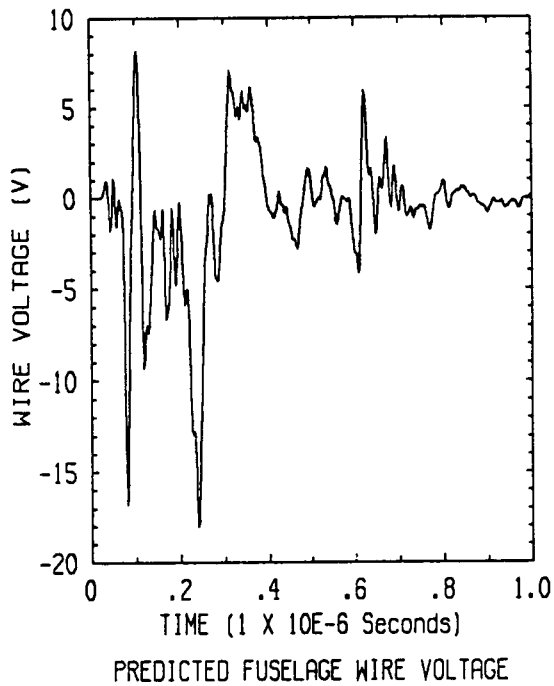


Flight 84-032, run 001, strike 002

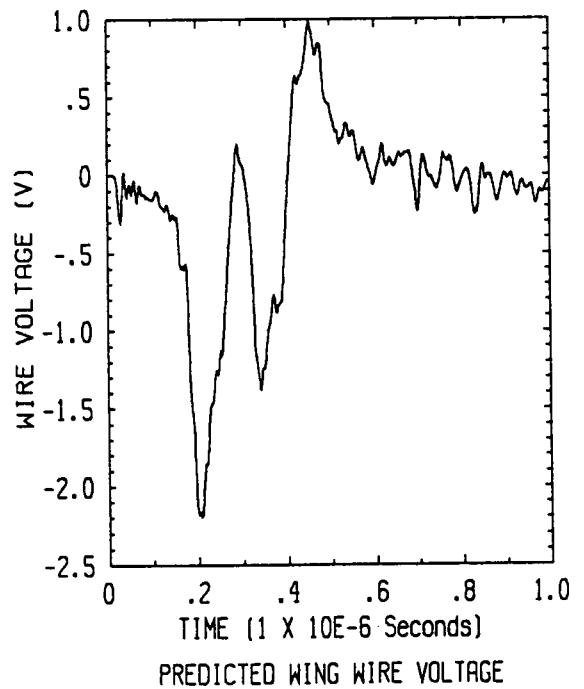


Flight 84-032, run 002, strike 004

**Figure 4.7(h) Predicted Internal Wire Responses**

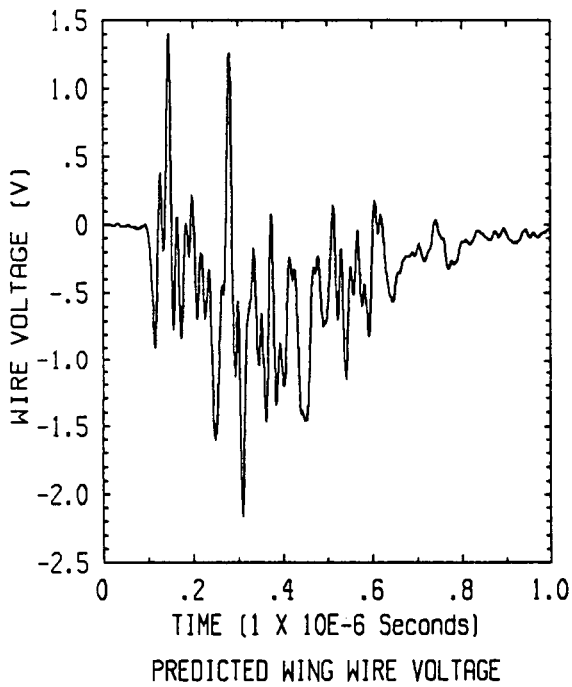
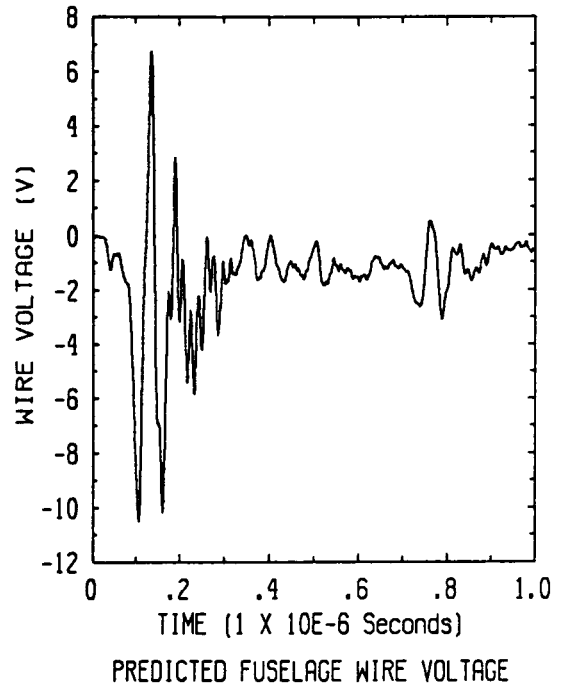
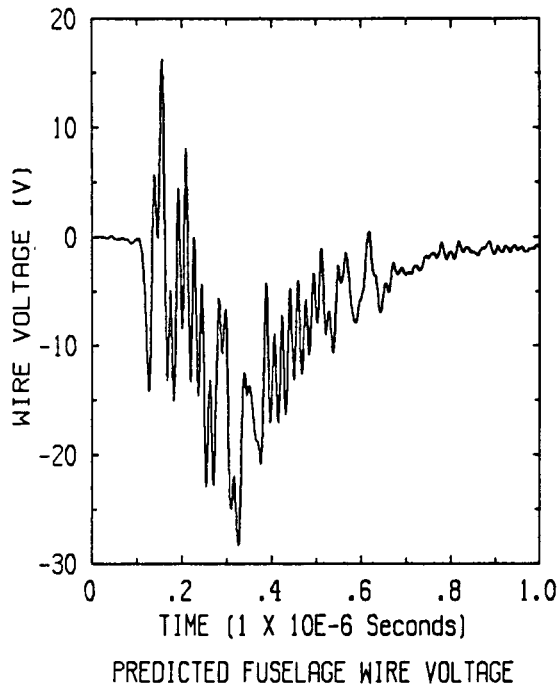


Flight 84-032, run 004, strike 013

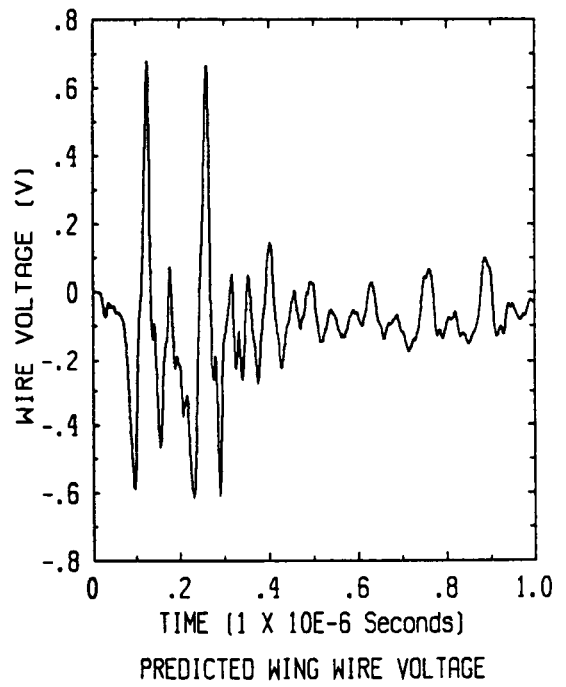


Flight 84-035, run 003, strike 004

**Figure 4.7(i) Predicted Internal Wire Responses**



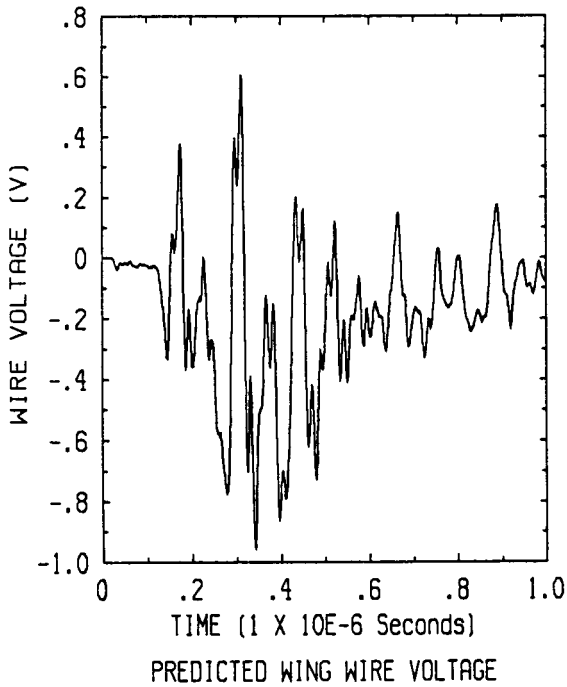
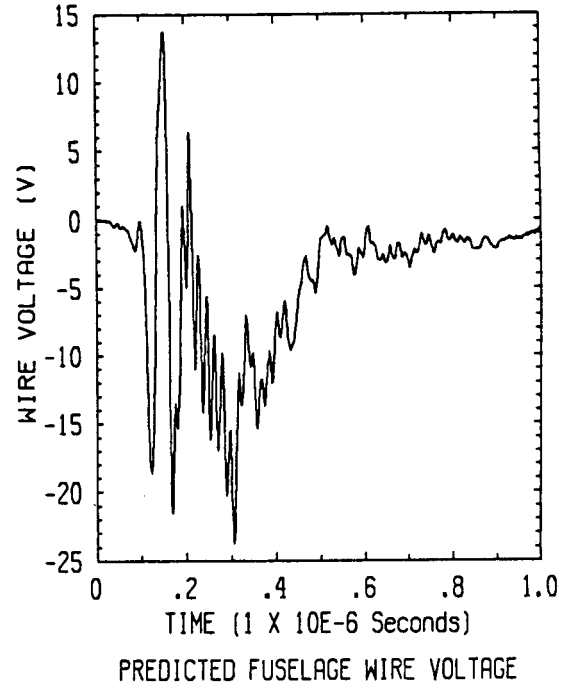
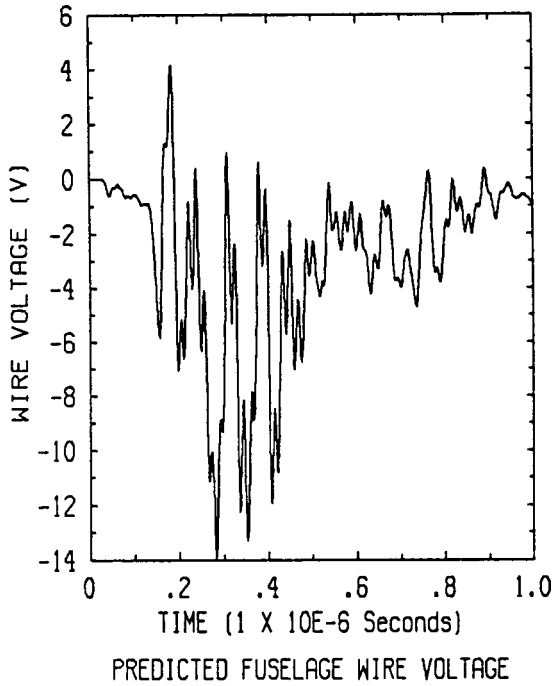
Flight 84-036, run 001, strike 001



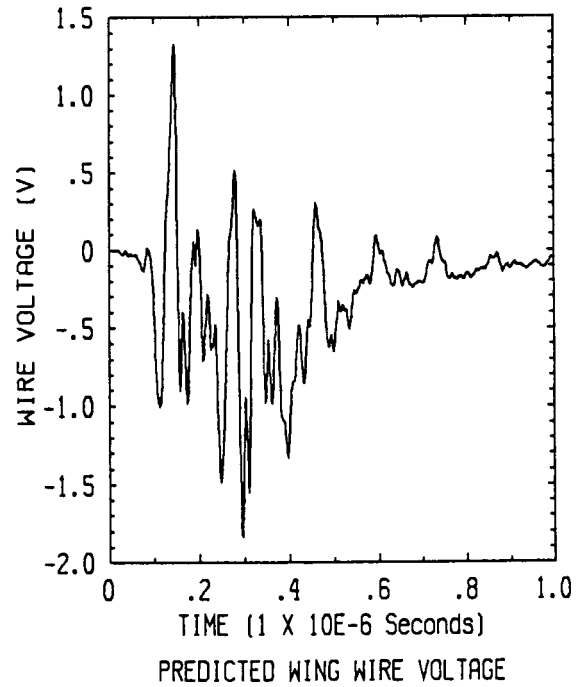
Flight 84-036, run 002, strike 002

**Figure 4.7(j) Predicted Internal Wire Responses**



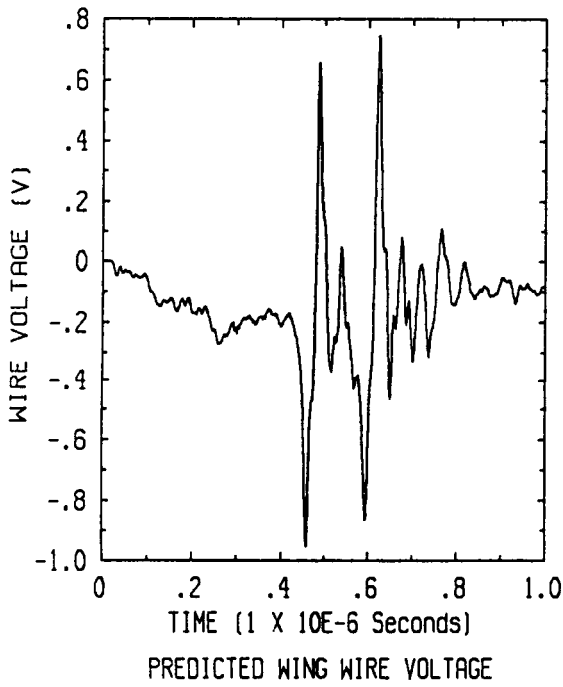
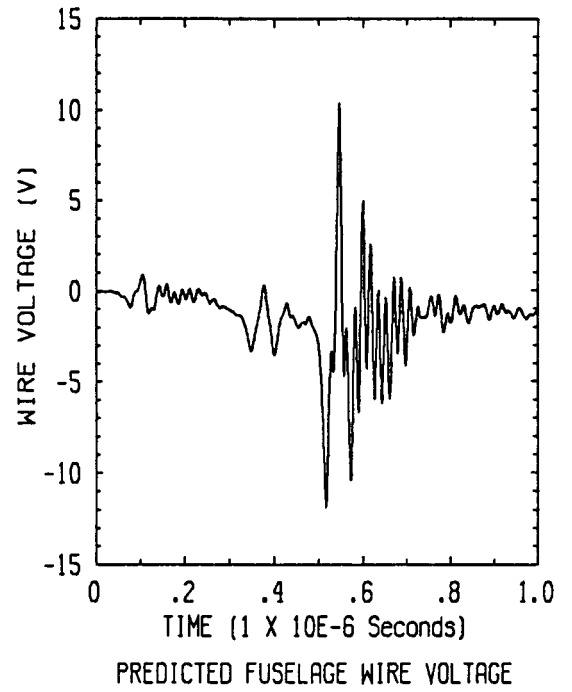
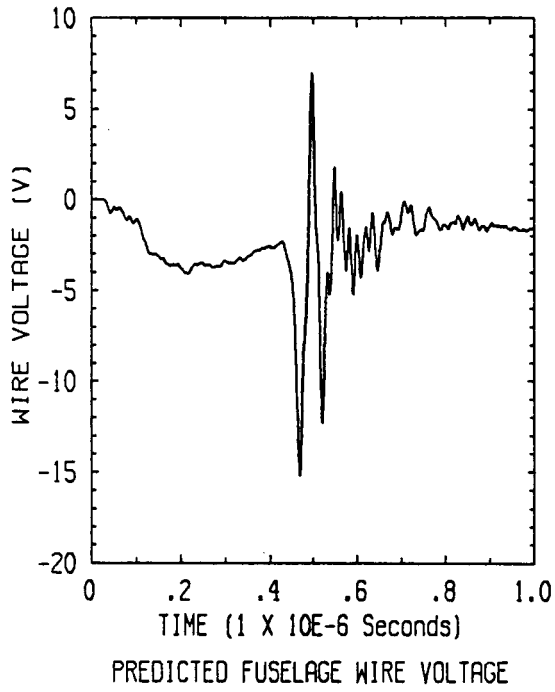


Flight 84-036, run 006, strike 009

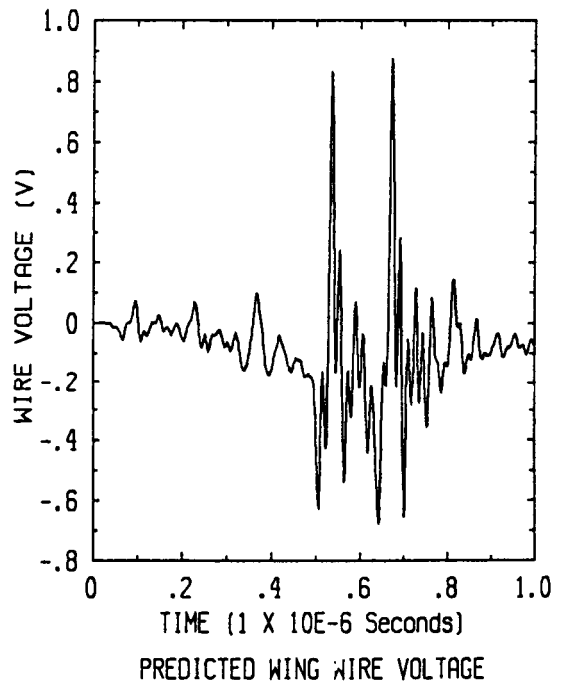


Flight 84-037, run 002, strike 018

**Figure 4.7(k) Predicted Internal Wire Responses**

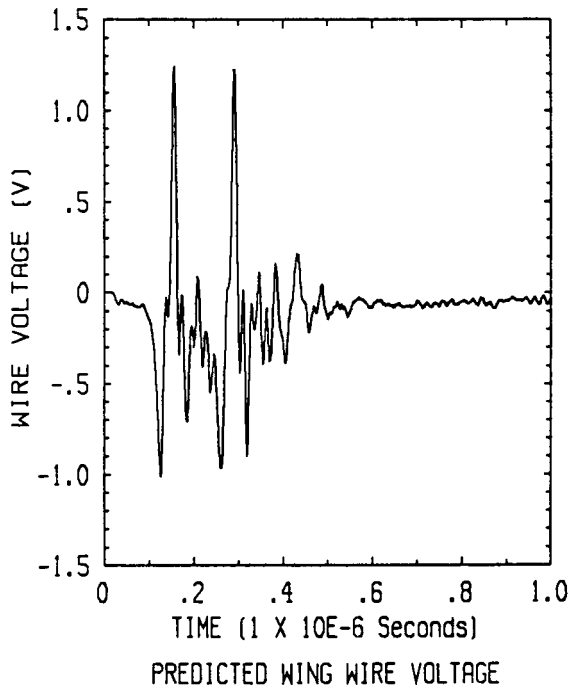
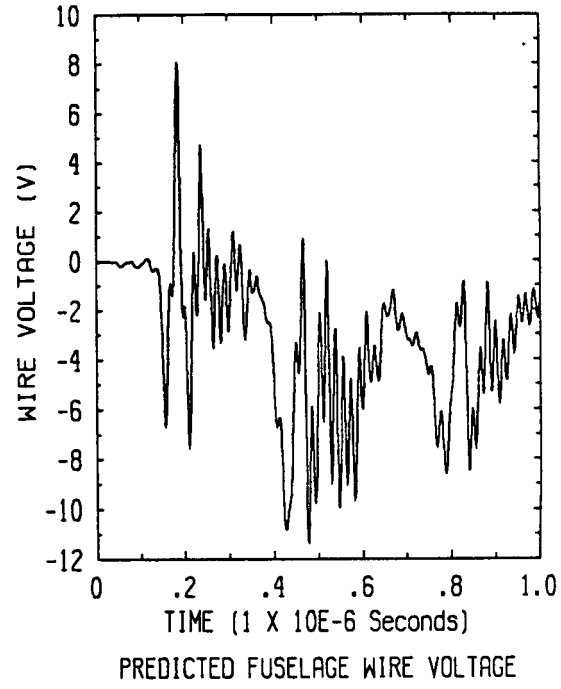
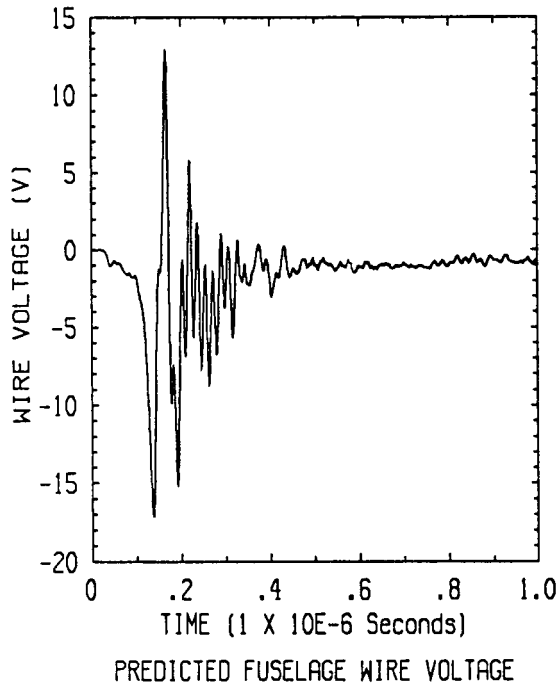


Flight 84-037, run 003, strike 022

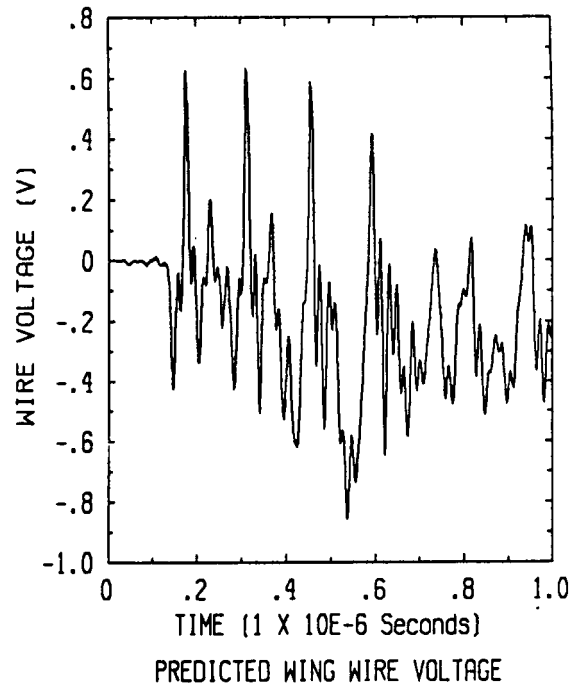


Flight 84-037, run 004, strike 024

**Figure 4.7(I) Predicted Internal Wire Responses**

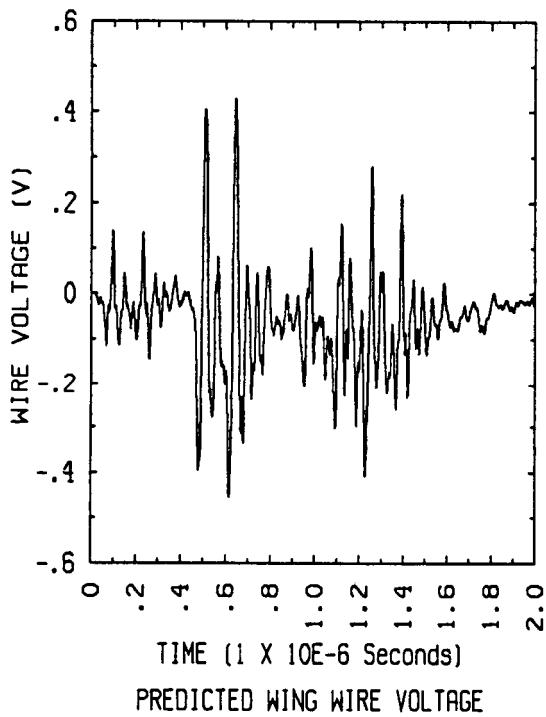
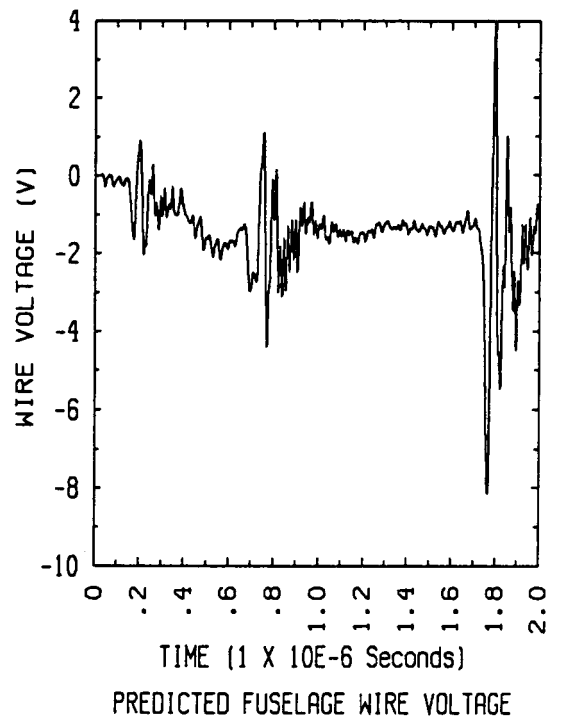
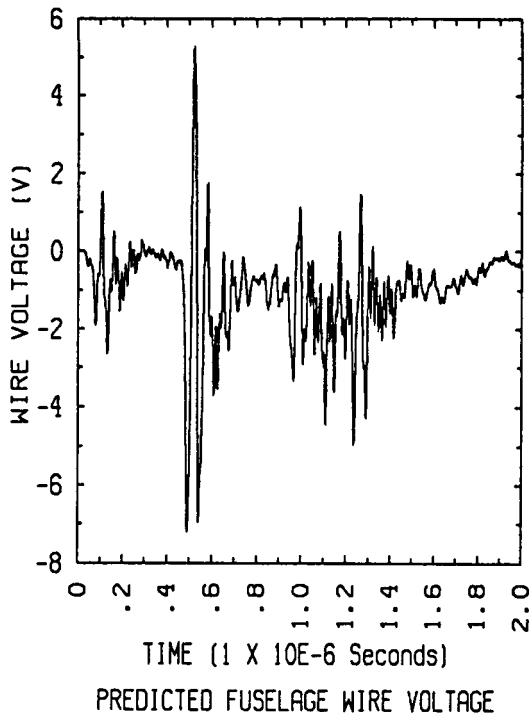


Flight 84-037, run 005, strike 029

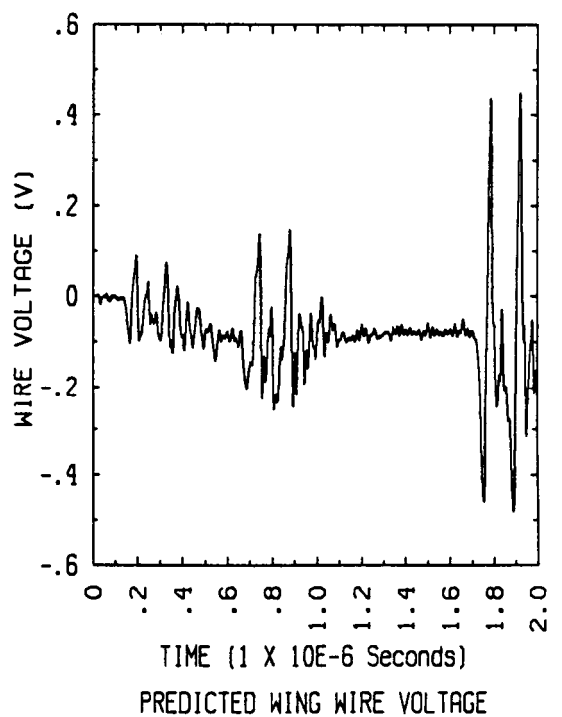


Flight 84-037, run 006, strike 034

**Figure 4.7(m) Predicted Internal Wire Responses**

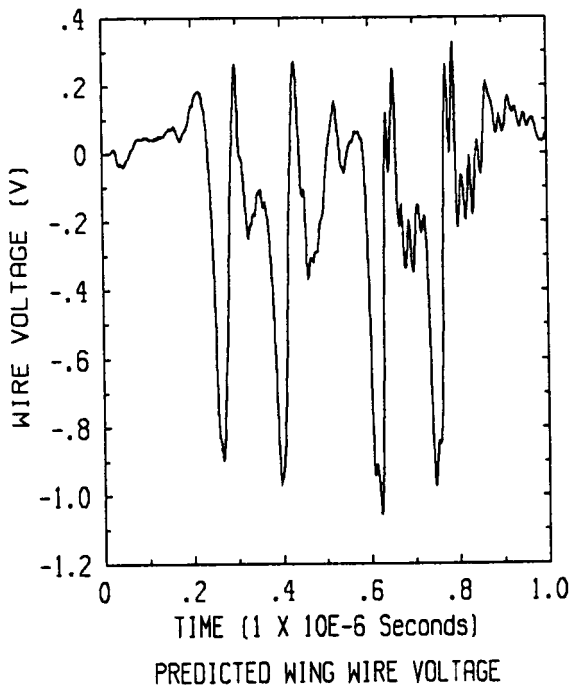
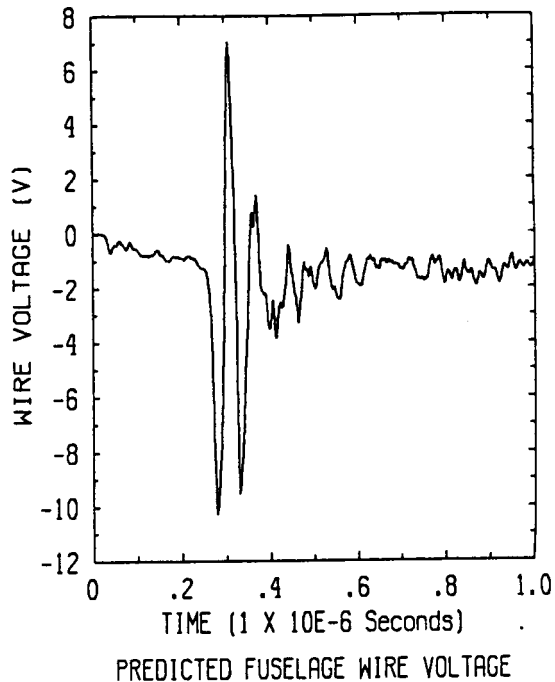
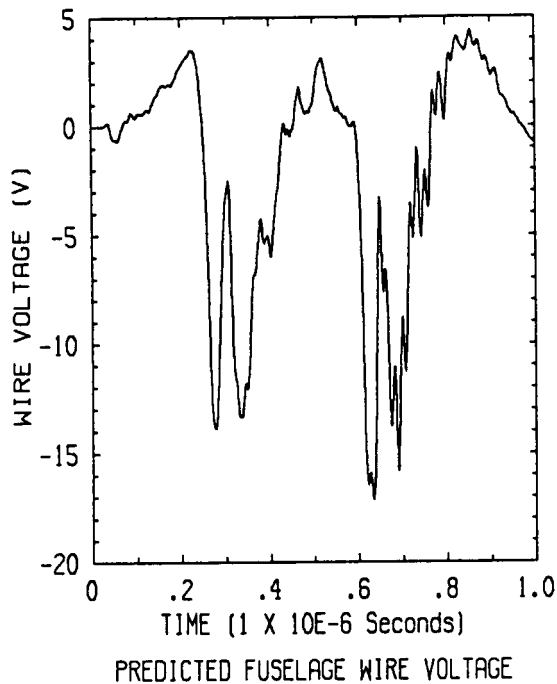


Flight 84-037, run 009, strike 044

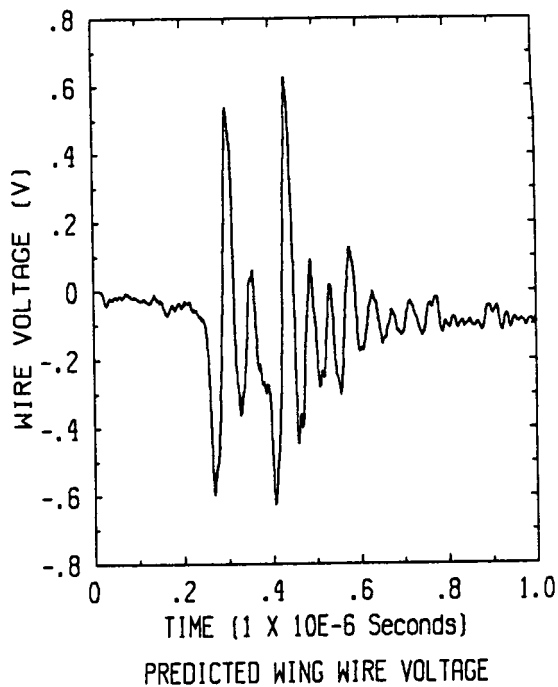


Flight 84-037, run 016, strike 063

**Figure 4.7(n) Predicted Internal Wire Responses**

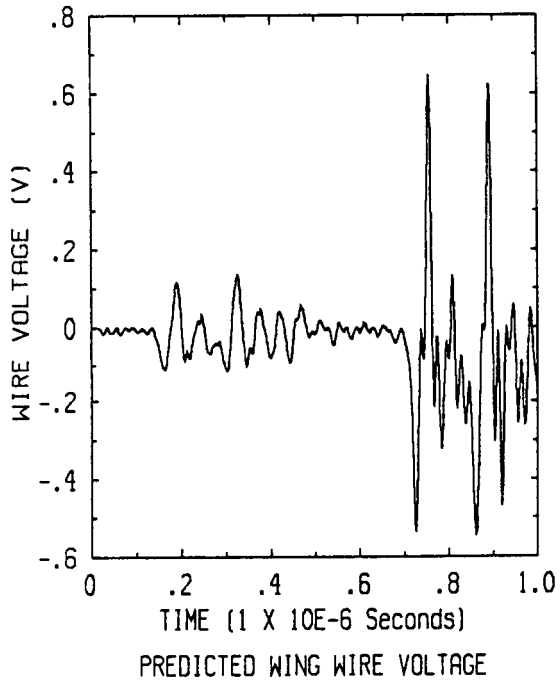
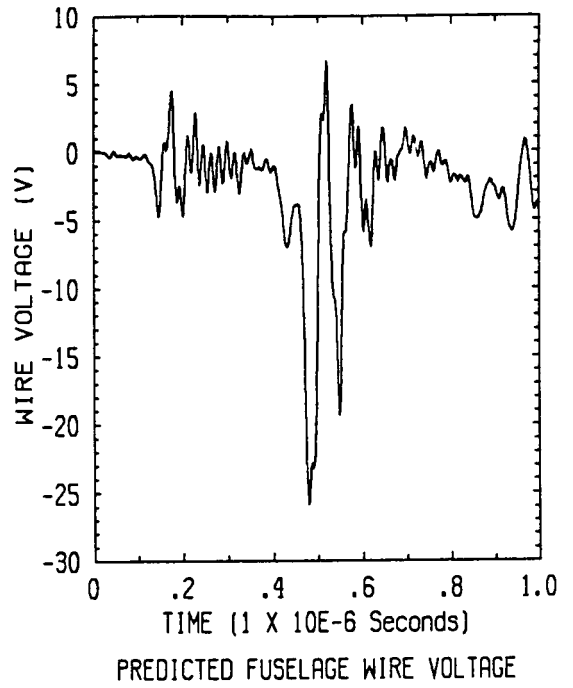
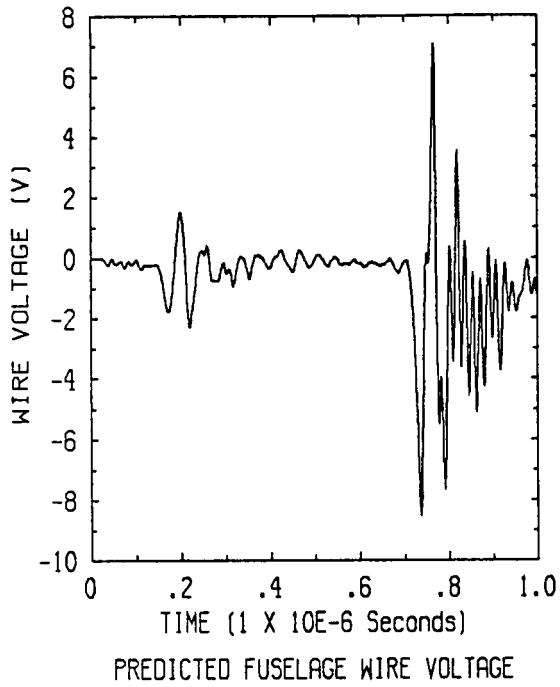


Flight 84-037, run 010, strike 052

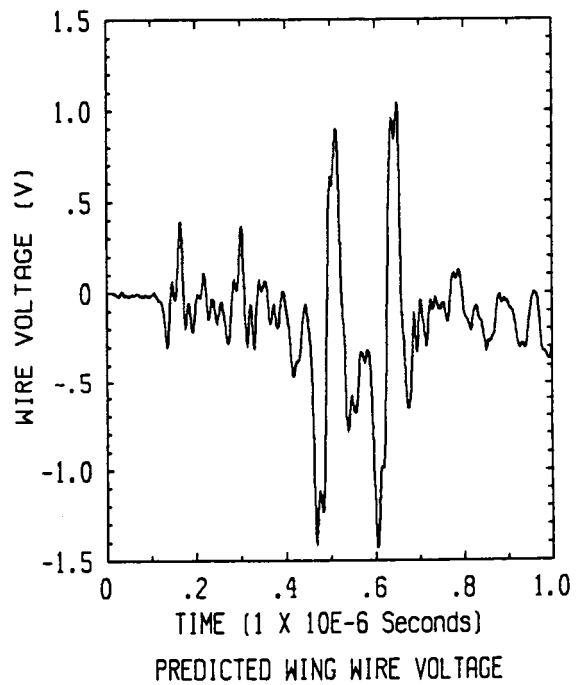


Flight 84-037, run 014, strike 058

**Figure 4.7(o) Predicted Internal Wire Responses**

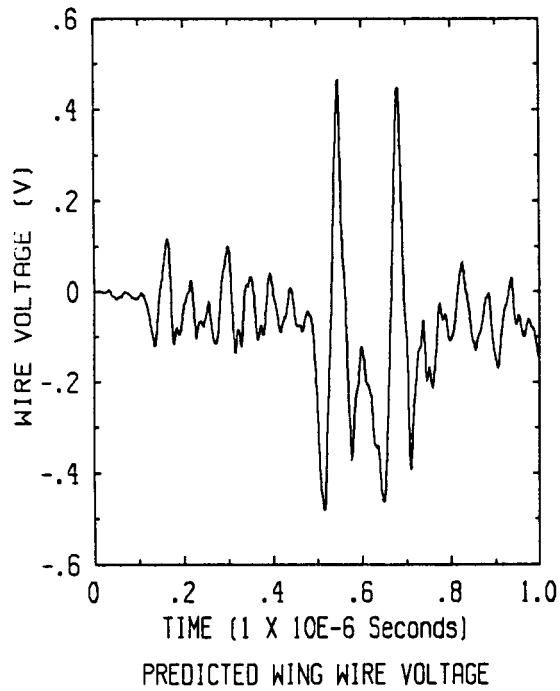
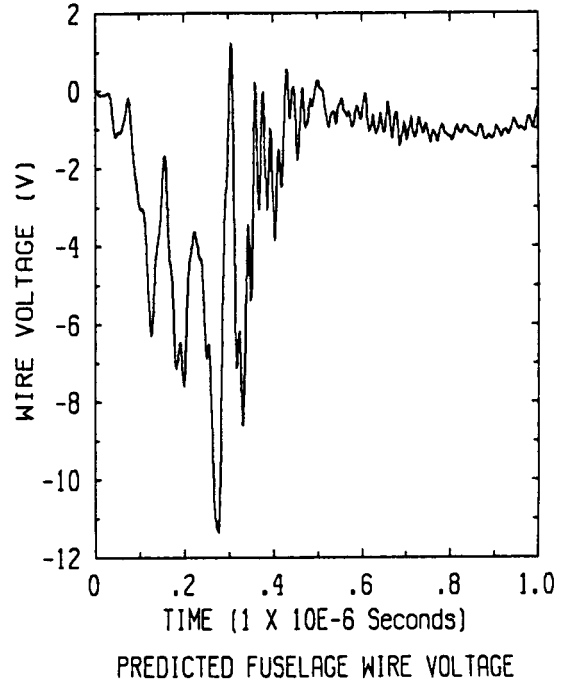
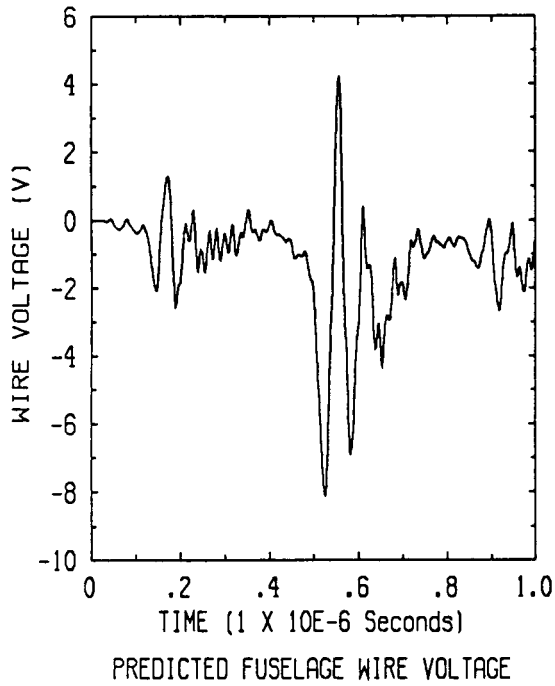


Flight 84-037, run 015, strike 062

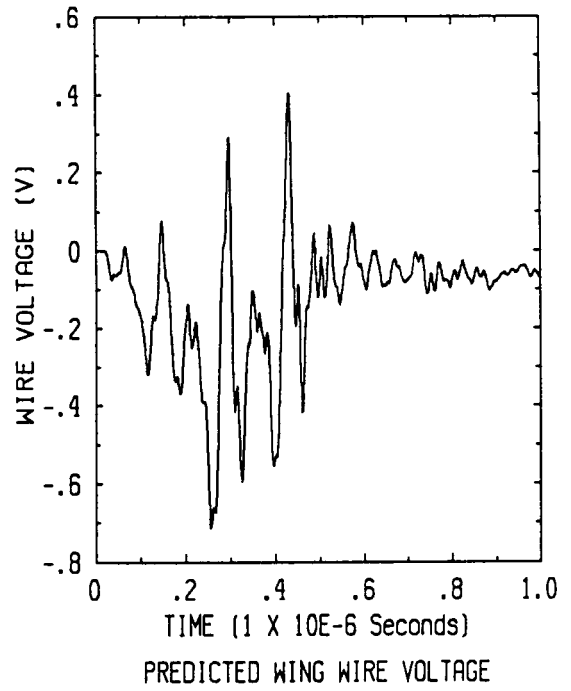


Flight 84-037, run 017, strike 066

**Figure 4.7(p) Predicted Internal Wire Responses**

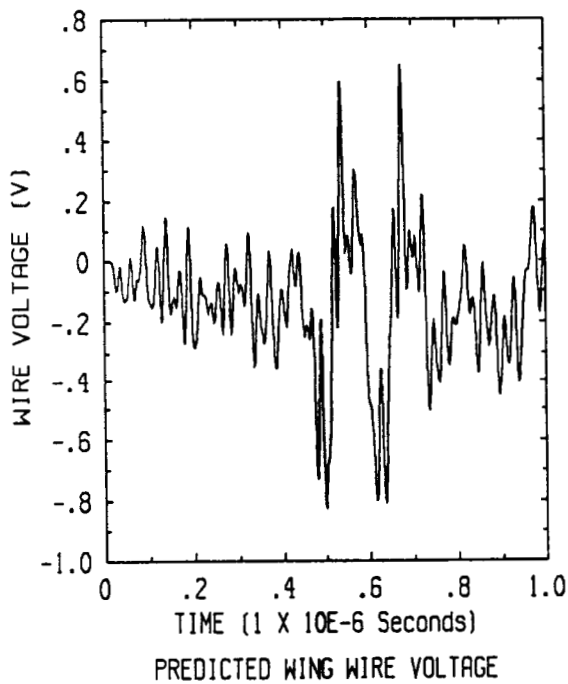
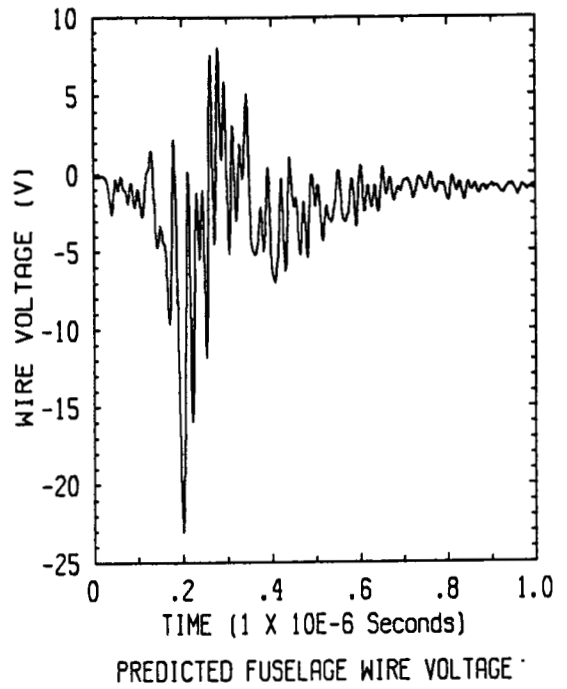
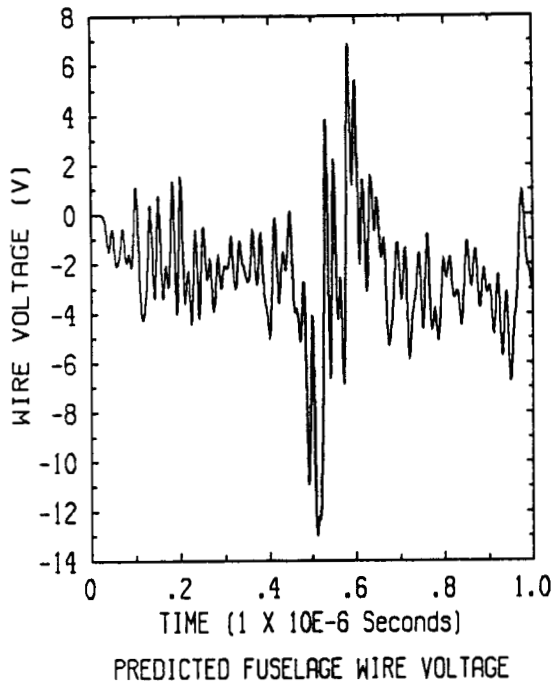


Flight 84-037, run 019, strike 071

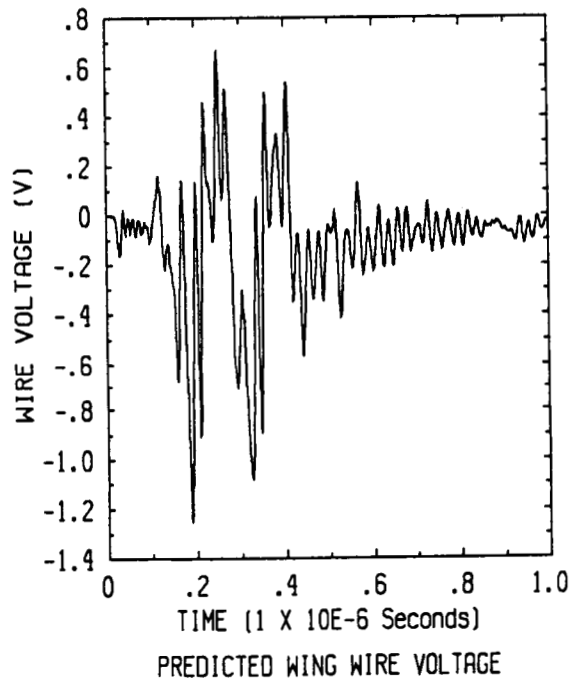


Flight 84-037, run 001, strike 002

**Figure 4.7(q) Predicted Internal Wire Responses**



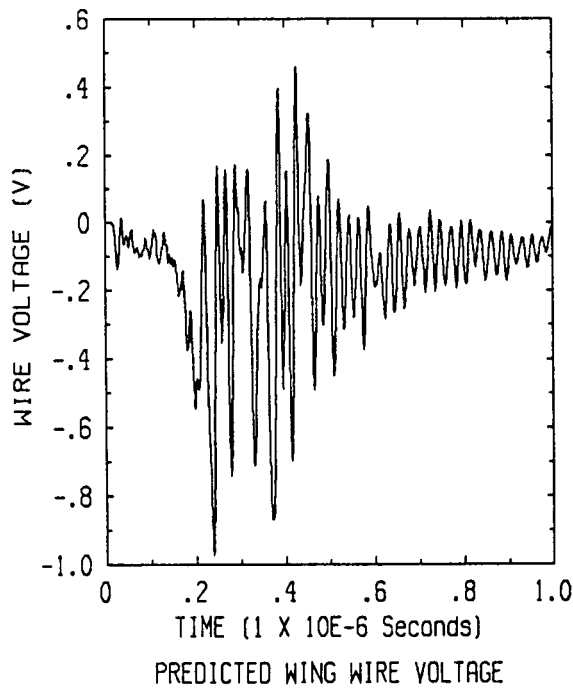
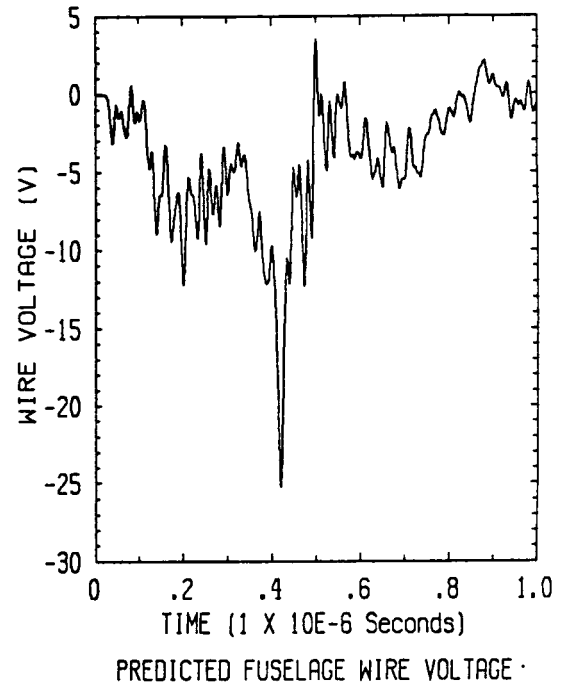
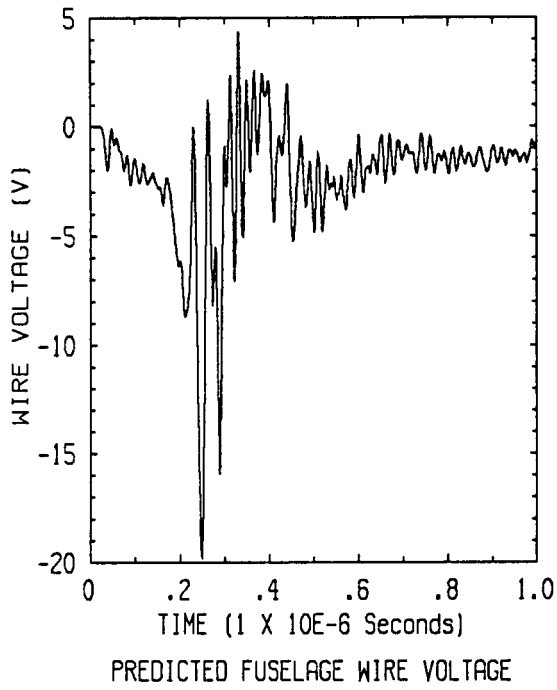
Flight 84-050, run 004, strike 007



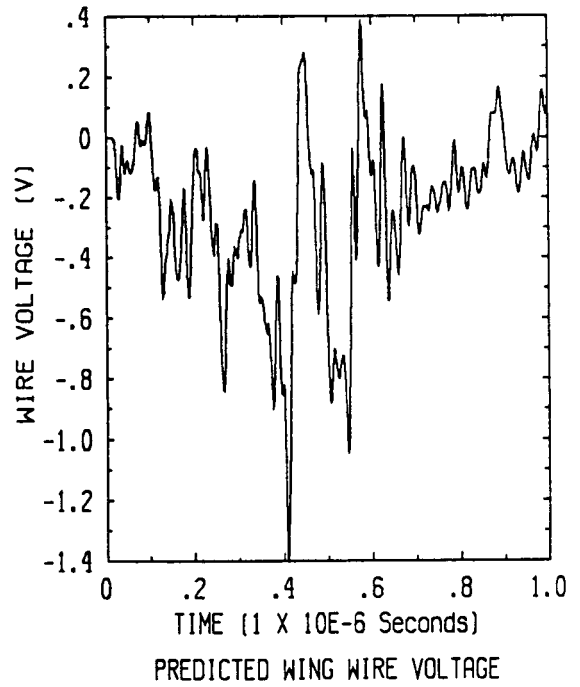
Flight 84-050, run 007, strike 016

**Figure 4.7(r) Predicted Internal Wire Responses**



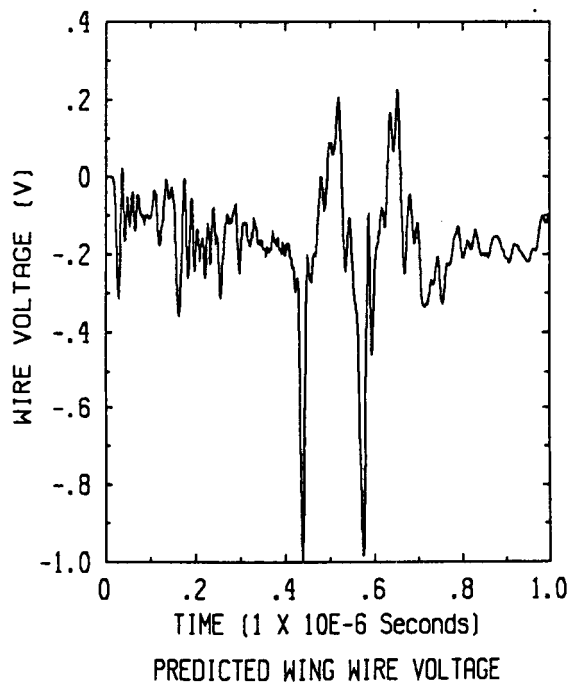
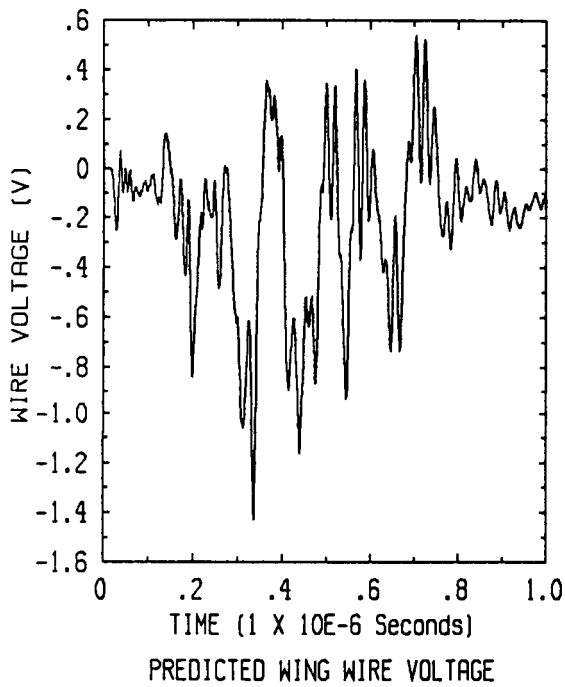
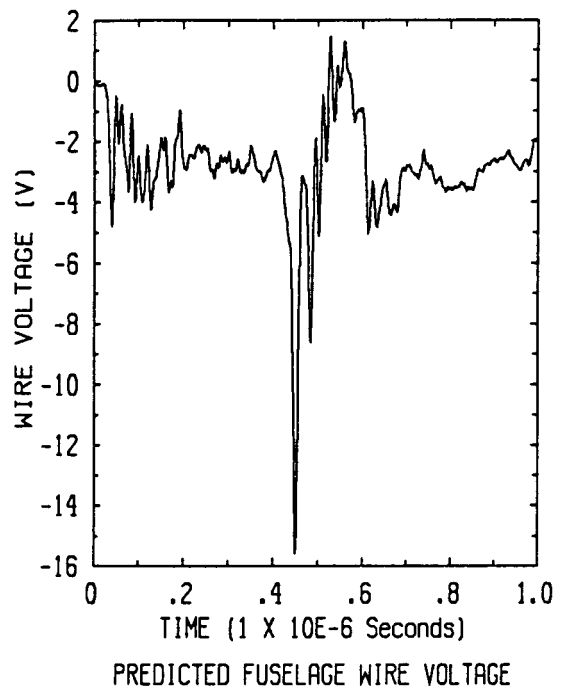
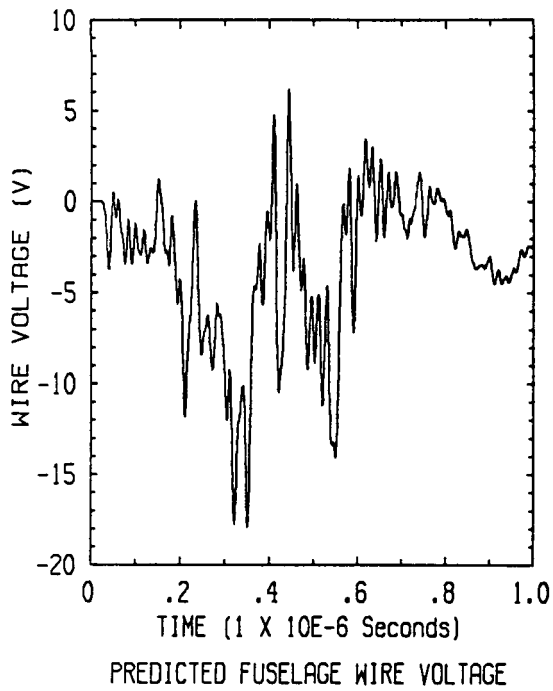


Flight 84-050, run 008, strike 020



Flight 84-050, run 010, strike 025

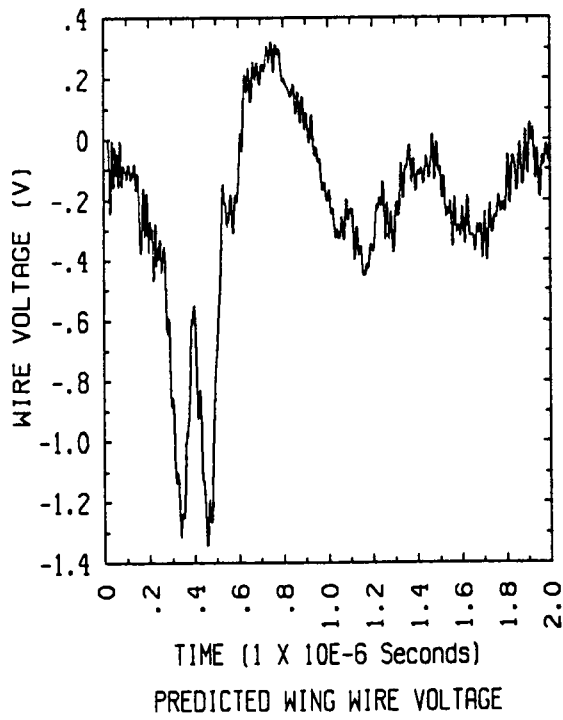
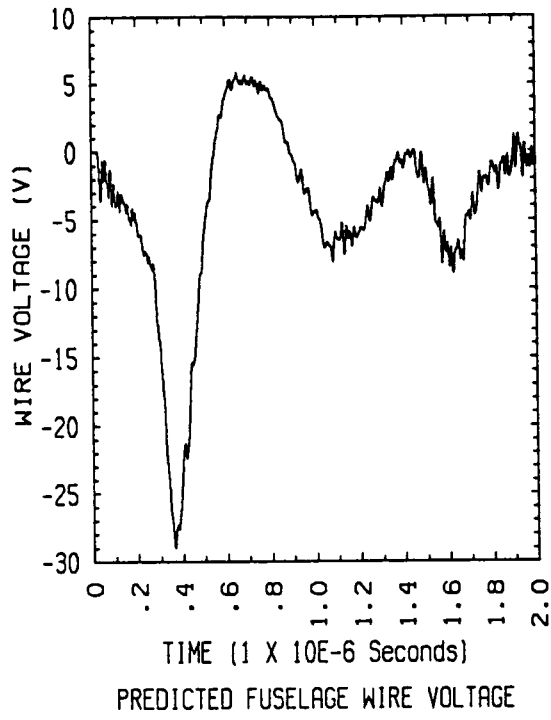
**Figure 4.7(s) Predicted Internal Wire Responses**



Flight 84-052, run 001, strike 001

Flight 84-052, run 002, strike 002

**Figure 4.7(t) Predicted Internal Wire Responses**



Flight 84-050, run 07A, strike 16A

**Figure 4.8 Predicted Internal Wire Responses for a Possible Multiple Strike Event**

## CHAPTER 5

# THE EFFECT OF THUNDERSTORM PARTICLES ON TRIGGERED LIGHTNING

### 5.1 Introduction

The initiation of lightning in a thunderstorm, either triggered or natural, is a phenomenon which is not fully understood. Maximum observed electric field levels within a cloud are generally significantly lower than the levels needed to start an electron avalanche which could lead to a lightning event. It is therefore necessary to look for sources of field enhancement which increase the electric field in local areas of the thundercloud to values which do result in avalanching. The presence of a large conducting object, such as the F106B aircraft, is one way in which this may be accomplished. Another candidate for enhanced fields is the region around a naturally occurring thunderstorm particle such as a water droplet or ice crystal. These often irregularly shaped particles can produce significant enhancements in small surrounding volumes. When one considers the number of these particles in a thundercloud, it is clear that they can be a major source of electrical corona within the cloud, and may contribute to the initiation of lightning.

In this chapter the effect of precipitation particles on lightning initiation will be investigated by studying the small scale alterations that they make in the overall electric field distribution of the cloud. It will be assumed that each particle is immersed in a uniform field over its volume (a very good approximation), and that individual particles do not electrically interact with other particles (possibly a less valid assumption). The alteration that the particles cause in the net avalanche rate will be calculated, and results from a nonlinear triggered lightning model compared for the cases in which thunderstorm particles are and are not present.

### 5.2 The Effect of Particles on Corona Formation

By locally redistributing the electric field energy density in a region of space, thunderstorm particles can affect the way in which electrons and ions are produced in an electron avalanche. In particular, a uniform electric field which is below breakdown intensity may be locally enhanced to a level which produces corona around the

particles. This occurs because the avalanche rate is strongly nonlinear with electric field, so that small electric field changes can result in large changes in charged particle production.

As an example of this consider the case of a spherical particle in a uniform static electric field,  $E_0$ , with magnitude ninety percent of air breakdown intensity. This is shown schematically in Figure 5.1. The electrical conductivity of the particle is important only for very fast field changes (of the order of microseconds), and in general the particle acts as a perfect conductor on the time scale of large scale thunderstorm fields. Because of this the well-known analytic development for the altered field distribution around a conducting sphere in a uniform electric field may be used. Figure 5.1 shows the regions around the particle in which fields larger and smaller than the ambient field exist. In addition the regions in which the field magnitude exceeds air breakdown level,  $E_b$ , are shown. These latter regions depend on the magnitude of the ambient field with respect to breakdown field. That is, if the ambient field drops, the breakdown region will shrink, finally disappearing altogether when the ambient field goes below one-third of the breakdown field. The other regions, those of enhanced and decreased field, are not dependent on ambient field strength.

The preceding discussion was based on a spherical particle. The situation for more irregular particles such as ice crystals or snow flakes is more complicated. Analytic solutions for these shapes do not exist, so approximations must be made in specifying the local field distribution around the particle. In general, however, a polarized particle will behave like an electric dipole to some level of approximation. The assumption used in the development presented here is to treat the local field distribution the same as that around a spherical particle, but to raise the maximum field enhancement to that determined from a previous study [3] (e.g., enhancement of five for columnar ice crystals and nine for a typical snowflake).

The importance of Figure 5.1 is that it shows that a conducting particle can cause electron avalanching to occur in a region of space which would have no avalanching in the particle's absence. The details of how much avalanching occurs because of the particle and the effects of irregularly shaped particles and particle density are left for the mathematical development of the next section.

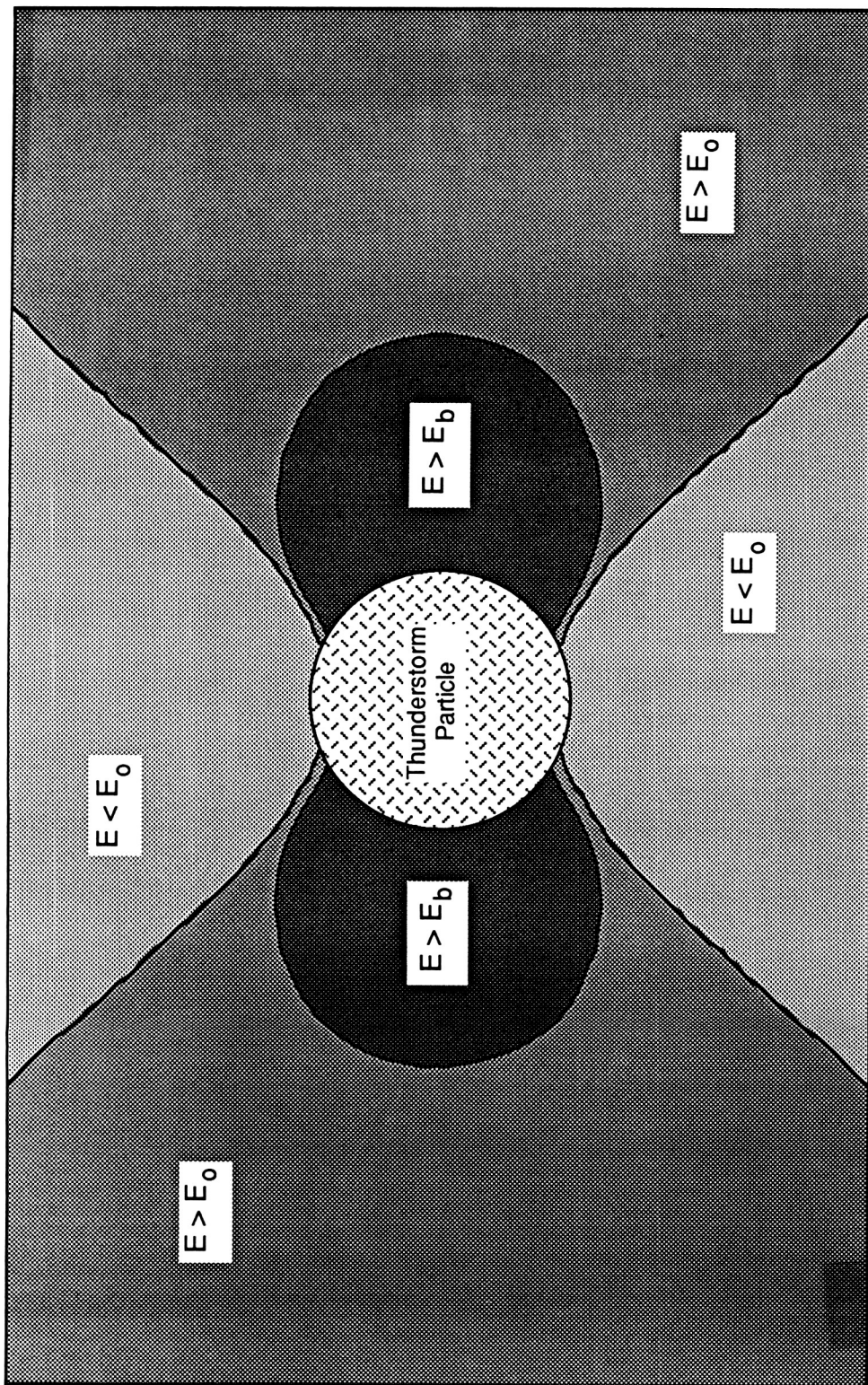


Figure 5.1 Electric Field Distribution Around a Typical Spherical Thunderstorm Particle  
 $E_0$  Is Ambient Field, Oriented Horizontally  
 $E_b$  Is the Field Required for Air Breakdown

### 5.3 Mathematical Development

To facilitate the mathematical development to follow, some symbols will first be defined. The development will be done in a spherical coordinate system, assuming no azimuthal variation. The ambient field is assumed to be oriented along the polar axis. The assumption of no azimuthal variation is strictly true only for spherical particles or cylindrical particles oriented with their axis along the polar axis. Particles not satisfying this criterion will be included in an approximate sense.

**Table 5.1**  
**Definition of Symbols Used in Section 5.3**

$a$	- approximate half size of particle (radius in the case of a spherical particle)
$E_o$	- ambient electric field intensity
$E_b$	- breakdown electric field intensity
$E_r$	- radial electric field intensity
$E_\theta$	- theta component of electric field intensity
$E_z$	- component of electric field intensity along polar axis
$f_{max}$	- maximum electric field enhancement factor (particle dependent, defined as the ratio of local electric field to ambient electric field)
$n$	- density of thunderstorm particles
$N$	- number of thunderstorm particles in a finite difference cell
$\rho$	- air density relative to sea level density
$\Delta V$	- volume around a particle in which field is above $E_b$

The objective of the analysis to follow is to develop a modified electron avalanche rate which accounts for the presence of thunderstorm particles. Previous work has assumed that corona formation occurs in clear air only. To include particles, it is necessary first to calculate the avalanche occurring around a single particle and then to consider the effects of a particle density in a given region of space. The electric field around a single particle is investigated first.

The field distribution outside of a spherical conducting particle placed in a uniform electric field is given by,

$$E_r(r,\theta) = E_o \left(1 + 2\frac{a^3}{r^3}\right) \cos \theta \quad (5.1)$$

$$E_\theta(r,\theta) = -E_o \left(1 - \frac{a^3}{r^3}\right) \sin \theta$$

Figure 5.2 shows the spherical coordinate system used in the analysis. For use here this expression is generalized to approximate the field distribution around irregularly shaped particles as follows,

$$E_r(r,\theta) = E_o \left[1 + (f_{\max} - 1)\frac{a^3}{r^3}\right] \cos \theta \quad (5.2)$$

$$E_\theta(r,\theta) = -E_o \left(1 - \frac{a^3}{r^3}\right) \sin \theta$$

Note that the only difference between equations (5.1) and (5.2) is that the 2 in the first of equations (5.1) has been replaced by the term  $f_{\max} - 1$  in equation (5.2). This reduces to equation (5.1) in the case of a sphere (for which  $f_{\max} = 3$ ). The justification for using equation (5.2) in the present model is not rigorous. Any conducting particle placed in a uniform electric field must polarize, and the resulting field distribution must in some sense resemble a dipole field. The assumption is made here, mainly for the purpose of making further analytic progress on particles in general, that the distribution



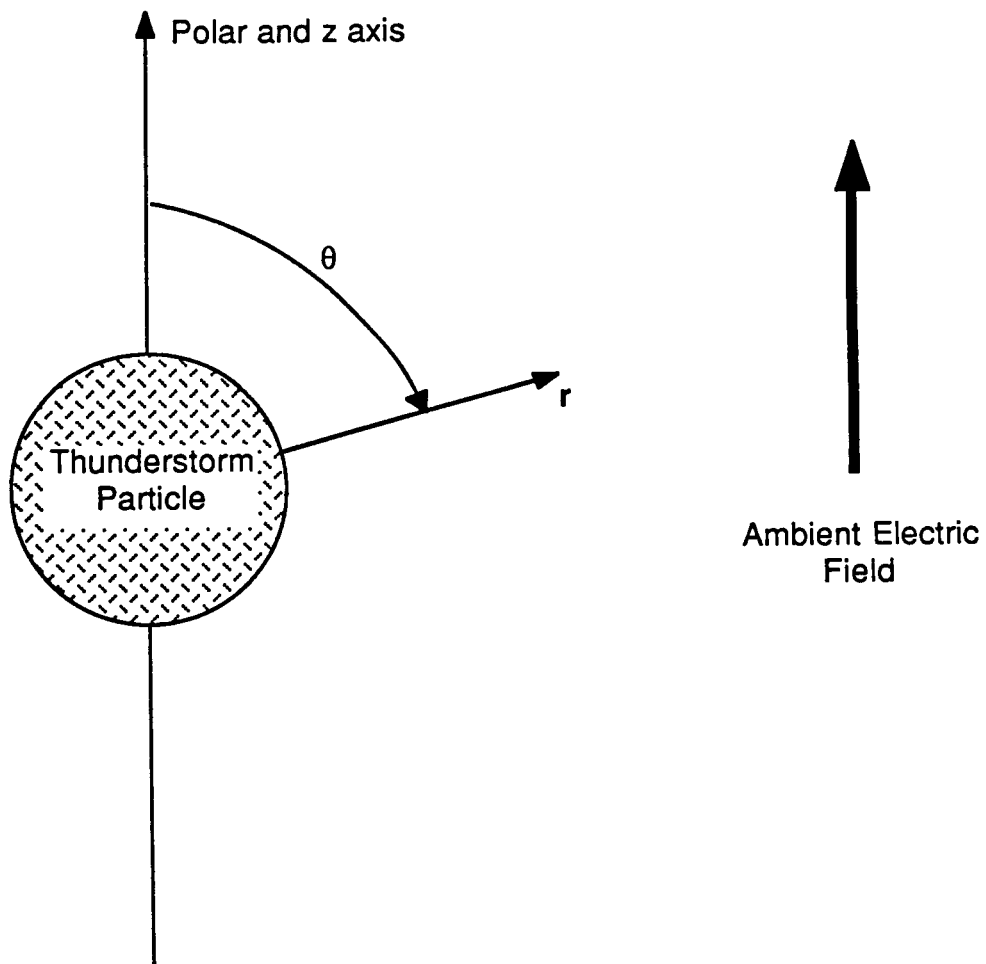


**Figure 5.2 Spherical Coordinate System Used in Analysis of Thunderstorm Particles**

is similar to that around a spherical particle, but with differing maximum field enhancements.

In addition, the electric field used in the calculations to follow is the component along the polar axis of the coordinate system. Strictly speaking, the total electric field is more appropriate. However, the form of the polar component is much easier to work with analytically, and introduces only a small error. The error is small because the axial oriented field is a good approximation to the total field at most locations. The axial field is easily calculated from equation (5.2) and is shown below.

$$E_z(r,\theta) = E_o \left[ 1 + (f_{\max} \cos^2\theta - 1) \frac{a^3}{r^3} \right] \quad (5.3)$$

This expression involves three physical quantities of interest, the ambient electric field, the size of the particle, and its shape (included in  $f_{\max}$ ). These three quantities, along with the breakdown field strength at a particular altitude and the particle density, completely determine the altered avalanche rate from the clear air expression. The next step in the analysis is to specify the volume around the particle over which avalanching occurs. In other words, over what volume is  $E_z$  larger than  $E_b$ ? The condition for this is expressed in equation (5.4).

$$E_o \left[ 1 + (f_{\max} \cos^2\theta - 1) \frac{a^3}{r^3} \right] \geq E_b \quad (5.4)$$

There are three possible regimes for equation (5.4). If  $E_o$  is larger than  $E_b$ , then equation (5.4) is satisfied in all of space. This is of course the trivial case in which air breakdown would occur in the absence of particles. A second regime is one in which equation (5.4) is satisfied nowhere in space. This occurs when  $f_{\max}$  is not large enough to raise the maximum enhanced field above  $E_b$ . In this case air breakdown is absent even in the presence of particles. The middle regime in which equation (5.4) is satisfied in a limited region of space is the most interesting. The conditions  $f_{\max} \geq \frac{E_b}{E_o}$  and  $E_o < E_b$  define this regime. Here air breakdown occurs when particles

are present but not when they are absent. From equation (5.4) the volume over which this occurs can be specified as below.

$$0 \leq \theta \leq \cos^{-1} \sqrt{\frac{E_b}{f_{\max} E_o}} \equiv A \quad (5.5)$$

$$a \leq r \leq a \sqrt[3]{\frac{f_{\max} \cos^2 \theta - 1}{\frac{E_b}{E_o} - 1}} \equiv Ba$$

Equation (5.5) represents a two dimensional projection of a three dimensional volume. The full volume is obtained by rotating the area specified in equation (5.5) around the polar axis of the particle. Note also that there are two of these volumes, one on either end of a symmetrically shaped particle. An expression for the volume over which the enhanced electric field is above  $E$  can now be derived by integrating over the limits of equation (5.5) and multiplying by two to account for both ends of the particle. Formally this is written,

$$\Delta V = 2 \int_0^{2\pi} \int_0^A \int_a^{Ba} r^2 \sin \theta \, dr d\theta d\phi \quad (5.6)$$

The details of the integration are straightforward, and the final expression for the avalanche volume is,

$$\Delta V = \frac{4\pi a^3}{9} \frac{E_o f_{\max}}{E_b - E_o} \left[ 1 + 2 \left( \frac{E_b}{E_o f_{\max}} \right)^{3/2} - 3 \left( \frac{E_b}{E_o f_{\max}} \right) \right] \quad (5.7)$$

The most important thing to notice about equation (5.7) is the way in which  $\Delta V$  depends on various quantities. A large  $\Delta V$  implies that the particle has a significant effect on electron avalanching, and a small  $\Delta V$  implies very little effect. Therefore it is clear that larger particles (large  $a$ ) are most effective at altering the

avalanche rate, since  $\Delta V$  varies as the cube of the particle dimension. The shape is also involved, but is less important, in the sense that  $\Delta V$  is nearly linearly dependent on  $f_{\max}$ . Of course it must be remembered that  $f_{\max}$  is quite important in determining whether there will be any avalanching at all around the particle.

Equation (5.7) gives the volume around a single particle in which avalanching will occur. To implement this concept in a numerical model, it is necessary to include the density of particles which is present in the region of interest. In a finite difference model the numerical region of interest is always a finite difference cell. Hence it is necessary to calculate the total volume which has fields above breakdown level in a given cell. The assumption is made that the electric field calculated in a finite difference cell is the ambient field in that cell, and that any particle density that may be present acts to enhance that field in small volumes around the particles. The total volume with field above breakdown strength in a single finite difference cell is then,

$$\Delta V_T = N\Delta V \quad (5.8)$$

where  $N$  is the number of particles in that cell and is numerically equal to the particle number density multiplied by the cell volume. In equation (5.8) the assumption has been made that the particles are noninteracting in the sense that none of the individual enhanced field volumes overlap. This appears to be a reasonable approximation for typical particle densities in thunderstorms. The assumption may be restated by saying that the total volume above breakdown must be less than the total cell volume.

The next step in the analysis is to calculate the number of electron-ion pairs produced in  $\Delta V_T$  per unit time. This is essentially the desired avalanche rate from particles. The rigorous method to find this quantity is to integrate the (strongly electric field dependent) avalanche rate over  $\Delta V$ . This is computationally inefficient in a finite difference code, however, so the method used here is somewhat different. The alternate method is to define an average electric field in the breakdown volume and to simply evaluate the altered avalanche rate for that electric field. One possible choice of this average field is to set it equal to the arithmetic average of the smallest and

largest fields in the volume. These fields are  $E_b$  and  $f_{\max} E_o$ , respectively. However, because the largest field exists only in a very small subvolume of  $\Delta V$  it would be better to favor the lower fields in any average. Therefore the geometric mean is used, as shown below.

$$\text{Average field} = \sqrt{E_b f_{\max} E_o} \quad (5.9)$$

The geometric mean is always less than or equal to the arithmetic mean, so this should be a more appropriate value to use in the model.

Finally the avalanche rate from particles may be formally written,

$$G_{\text{particles}} = G_{\text{clear air}}(\text{average field}) \frac{\Delta V_T}{V_{3D\text{cell}}} \quad (5.10)$$

This form is suitable for inclusion in the finite difference model documented in previous work [3]. It is simply an adjustment to the usual (clear air) avalanche rate by the ratio of volumes, and with the usual avalanche rate evaluated at an appropriate average field.

The last matter to be considered is the issue of irregularly shaped particles which may not be aligned with their axis along the ambient electric field. Although electrostatic forces would tend to align these particles, it is likely that hydrodynamic forces from winds and small scale turbulence would overwhelm the electrostatic force. Hence the particles are probably randomly oriented with respect to the field direction. This is taken into account in the present model by assuming that on the average half of the particles are aligned along the field and half are aligned across the field. The particles across the field make no contribution to the particle dependent avalanche rate. In the model this is accomplished simply by dividing the true particle density by two to arrive at an effective density. It should be understood that this is done only for the case of nonspherical particles ( $f_{\max} \neq 3$ ), because for spherical particles alignment is unimportant.

## 5.4 Results

One of the immediate results which can be calculated from the thunderstorm particle model is the effective ambient field which causes air breakdown to occur. This should be lower in the presence of thunderstorm particles than in their absence. An approximation to the breakdown field is achieved by finding the field level at which the avalanche rate becomes larger than the electron attachment rate. Although this is not a strict criterion for air breakdown it does serve to illustrate the difference in corona growth caused by particles. Three situations were analyzed:

(1) No particles

(2) Small particles with high density

$$\begin{aligned}a &= 1 \text{ mm} \\n &= 1 \times 10^5 \text{ particles/cubic meter} \\f_{\text{max}} &= 5\end{aligned}$$

(3) Large particles with low density

$$\begin{aligned}a &= 2 \text{ cm} \\n &= 100 \text{ particles/cubic meter} \\f_{\text{max}} &= 9.\end{aligned}$$

The cases were done at ten different relative air densities ranging from .1 to 1.0. All cases were investigated for an assumed water content of 0 percent. This may not be appropriate for the center of a thunderstorm, but the results are not greatly changed for any realistic water content. Table 5.2 shows the nominal breakdown field for the three cases above as a function of relative air density. The labeling of the cases corresponds to the numbering given above.

**Table 5.2**  
**Nominal Air Breakdown Field as a Function of Air Density**

$\rho$	E (MV/m)		
	Case 1	Case 2	Case 3
.1	.22	.21	.16
.2	.43	.42	.33
.3	.64	.63	.49
.4	.86	.84	.65
.5	1.07	1.05	.81
.6	1.29	1.26	.97
.7	1.50	1.48	1.13
.8	1.72	1.69	1.30
.9	1.93	1.90	1.46
1.0	2.15	2.11	1.62

The interesting thing to notice from Table 5.2 is that the small high density particles have almost no effect on the nominal breakdown field. That case is typical of small high density ice crystals that one might find in the upper portions of a thundercloud. Case 3 represents quite large particles such as snowflakes. Results from the model show that it is necessary to have particles this large in order for the particles to have any significant effect on the air breakdown field. Small particles with low field enhancement factors have no appreciable effect on the overall corona initiation process. Although they enhance the electric field in a local region the volume over which this occurs is so small that very few avalanche electrons are produced in a macroscopic sense. The reason for this is the cubic dependence on the particle size in the expression for the avalanche volume (equation 5.7)). In summary it appears that thunderstorm particles are of great significance in altering the breakdown field only in regions where large particles exist.

Although particles do not in most cases greatly change the minimum air breakdown electric field, their presence can significantly change the responses seen

on an aircraft. For example, if the F106B is placed in a given uniform electric field of sufficient magnitude to trigger a lightning strike, the responses seen when particles are present are larger than they are in clear air. This is true only for a fixed uniform field which is the same in both cases. It can be explained by noting that the breakdown process, particularly the electron avalanche rate, is strongly nonlinear with field intensity, so that even a small increase of the field strength above minimum breakdown can result in a large change in breakdown character. Of course, in the case under consideration here, the particles produce a small decrease in the breakdown field, equivalent to a small increase in the ambient field.

The thunderstorm particle model has been implemented in the nonlinear finite difference triggered lightning model, and a few different thunderstorm situations investigated. One typical of what the F106B may encounter is shown in Figures 5.3 and 5.4. The case shown there is of a field oriented from top to bottom of the F106B. The ambient field magnitude is .3 MV/m, and there is a charge of -.895 millicoulombs on the aircraft. The relative air density is .5. Figure 5.3 shows the aircraft responses in the case where no particles are present. Figure 5.4 shows the responses for a particle environment. The particle density is  $1 \times 10^5$  particles per cubic meter, the particle radius is 1 millimeter, and  $f_{\max}$  is set at 5. This corresponds to columnar ice crystals at a high altitude.

It has been assumed for this comparison that the ambient electric field is the same in both the particle and clear air cases. This results in larger aircraft responses in the particle case because of the larger avalanche rate. In practice it is likely that the presence of particles in the air would slightly lower the triggering field and produce aircraft responses similar in magnitude to the pure air case. This would occur because the initial lightning current which drives all of the aircraft sensor responses is strongly dependent on the temporal behavior of the air conductivity. A slight lowering of the ambient electric field slows the growth of the lightning current which in turn drops the peak sensor responses seen on the F106B.

The main things to notice about the comparison are the following. First, the magnitudes of the responses for the case with particles are approximately a factor of two larger for the D-dot responses and five or more larger for the B-dot response. This occurs because of the slight lowering of the effective breakdown field in the



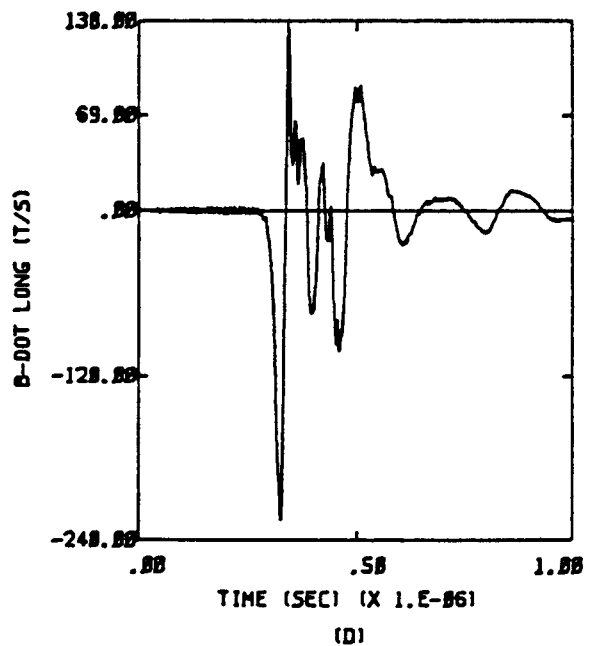
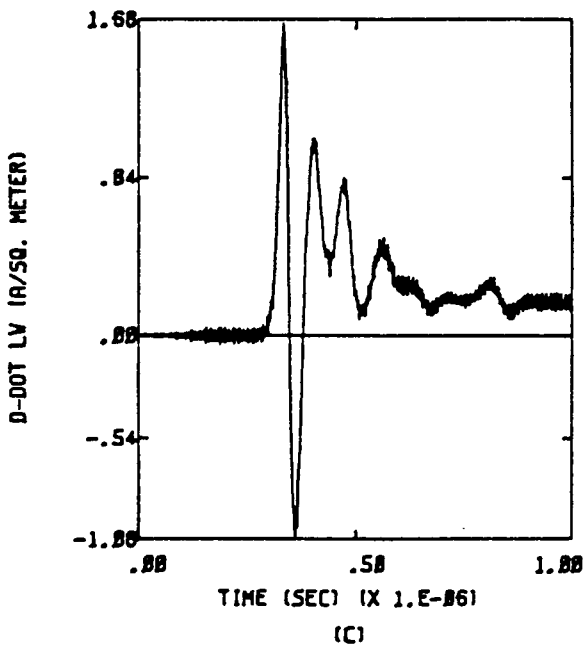
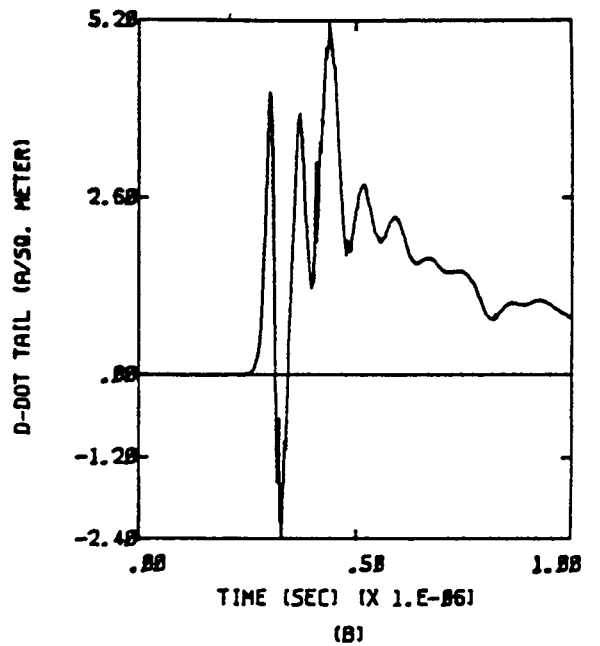
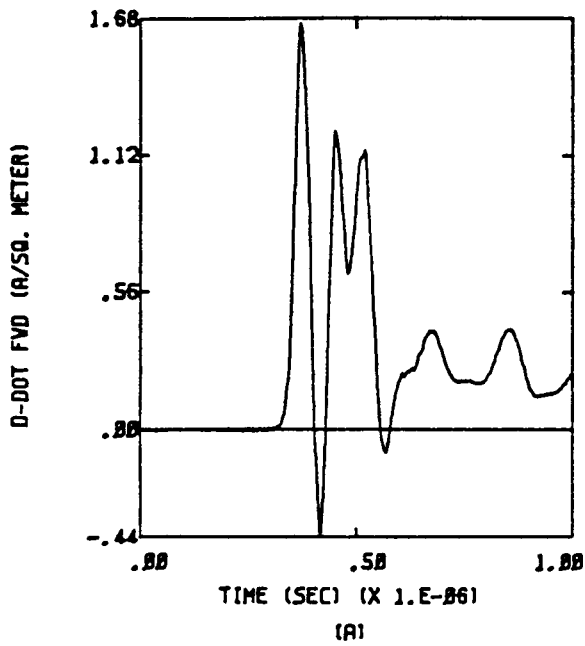
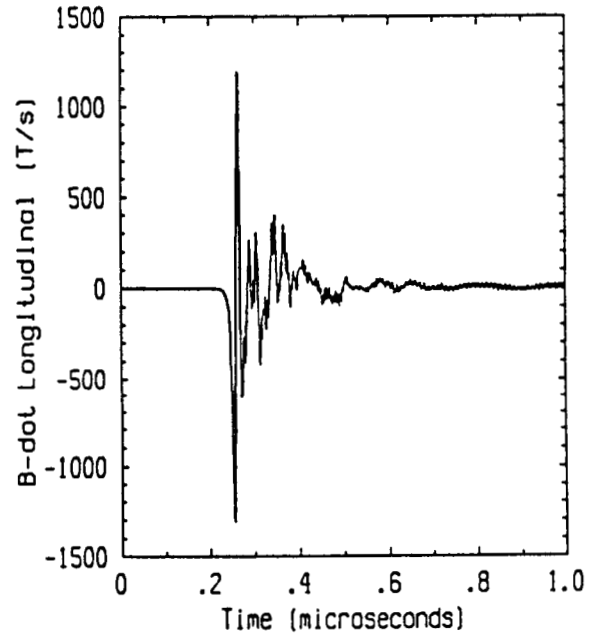
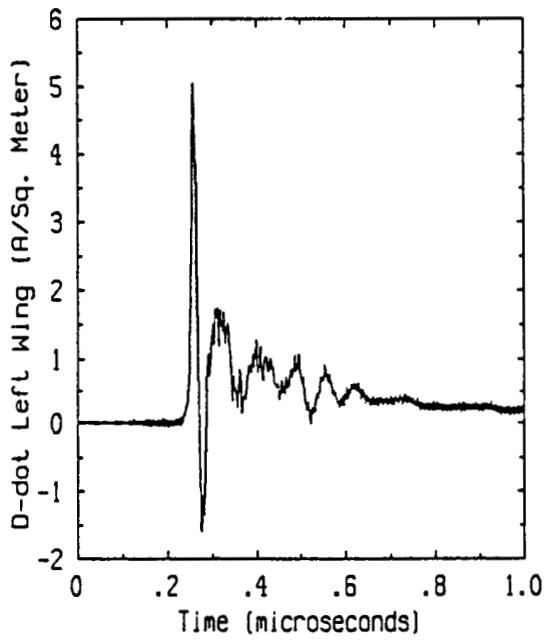
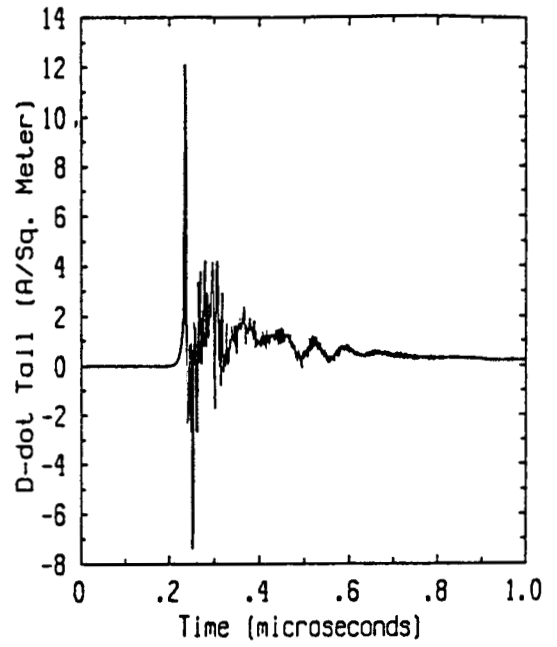
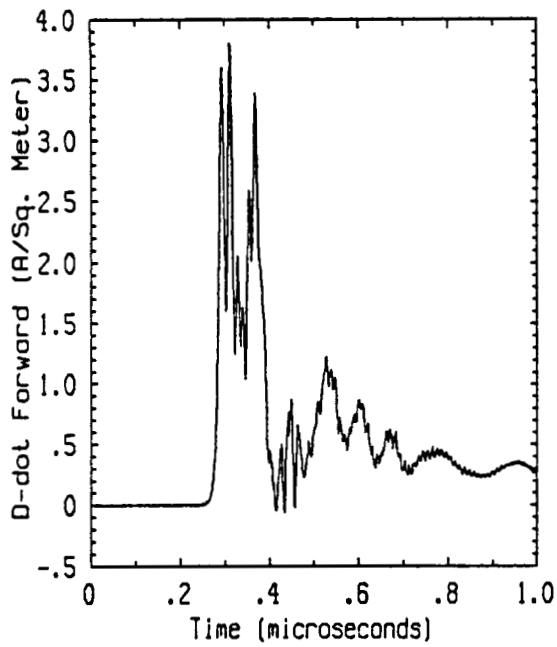


Figure 5.3 F106B Responses for a Vertically Oriented Ambient Field with Thunderstorm Particles Absent



**Figure 5.4 F106B Responses for a Vertically Oriented Ambient Field with Thunderstorm Particles Present**

particle case. This is also evidenced by the slightly earlier breakdown time. The second thing to notice, which may not be obvious from the plots themselves, is that the character of the responses is not greatly altered. If one ignores the larger first peak in the particle case, the rest of the waveforms are quite similar in terms of shape. The difference in scale of the plots of the two cases tends to obscure this character. The similarity is not completely unexpected, as the later portions of the waveforms must be characteristic of the resonances of the F106B, and are the same whether or not particles are present in the surrounding air. Although not shown in the figures, it may also be noted that the peak lightning currents in the two cases differed by approximately a factor of two, as would be expected from the D-dot responses.

In summary, the following has been learned from the thunderstorm particle model:

1. The electric field at which air breakdown occurs is not greatly altered by the presence of thunderstorm particles, except for the largest particles.
2. Particle size is much more important in altering the clear air avalanche rate than is particle density. This is because of the cubic variation of the avalanche volume with particle size.
3. Even though the effective breakdown field is not greatly changed by the presence of particles, aircraft responses may be significantly affected if breakdown occurs at the same field levels. This occurs because of the strongly nonlinear variation of breakdown characteristics with electric field. The net effect of particles is more likely to be a slight lowering of the trigger field with similar aircraft responses.

## CHAPTER 6

### SUMMARY AND CONCLUSIONS

The work documented in this report has concentrated on the triggered lightning environment of the F106B aircraft and the effect this environment has on aircraft internal and external electromagnetic responses. Models have been developed for lightning channels and internal wires on the aircraft. The effect of particles in the triggering event has been investigated, and form factors of the F106B measured. Several significant achievements may be highlighted.

#### 6.1 Form Factor Measurement

Although the method used to measure form factors on the F106B was not as successful as might be desired for large enhancements, the work performed was noteworthy nevertheless. The method has been widely utilized by other investigators and cited in the literature. However, no evaluation of the accuracy of the method by comparison with canonical shapes has been reported. The comparisons done in the present work define the limits within which reasonable results may be expected. Also, it has been shown that the method is accurate to 10 to 20 percent for moderate field enhancements in regions where the electric field is not rapidly varying in space. This should be true of the locations of the field mills on the F106B. Hence the form factors measured for these field mill locations may be usable in analyzing the measured field mill records on the aircraft. However, Mazur [13] has shown that even small errors in form factors can translate to large errors in ambient fields so any error in the form factors must be treated with caution.

#### 6.2 Lightning Channel Modeling

A lightning channel model utilizing a more complete air chemistry has been developed. The model, because it is two dimensional, is capable of following the development of the channel to late time (tens of microseconds). The model has been used to simulate a triggered strike to the nose of the F106B by placing a conical conducting structure representing the nose into the problem space.

### **6.3 Internal Wire Modeling**

The modeling of internal wires on the F106B has been quite successful, especially in view of the complicated internal structure of the aircraft. It has been shown that simple transmission line models employing discrete sources are adequate to simulate the majority of internal wire responses. The success of the modeling also provides additional validation of the linear transfer function models used to derive sources for the internal wires. These models, which use a measured response waveform to derive a lightning current from which internal wire sources are derived, have also been successfully used in modeling multiple simultaneous external electromagnetic responses. Examples of this are the successful overlays of I-dot measured and calculated responses presented in this report.

### **6.4 Thunderstorm Particle Modeling**

The modeling done in the investigation of the effect of thunderstorm particles on triggered lightning events has shown that the presence of particles does not greatly affect the threshold breakdown field intensity. The largest particles were shown to have the most effect on the breakdown field. However, because of the strongly nonlinear character of the breakdown on electric field strength, even a small change in threshold breakdown field can result in a large change in aircraft response. This has been illustrated by calculating the responses on the aircraft for both the clear air model and the model containing thunderstorm particles. The breakdown was found to be significantly larger in terms of aircraft response peak magnitudes for the case having particles. This finding could be of value in explaining some of the variability seen in measured F106B electromagnetic responses. The presence of various types of particles having varying shapes and enhancements in the air surrounding the F106B introduces an element of randomness into the triggered lightning process that is not present for the case of the aircraft flying in clear air. It should also be noted, however, that the most likely role for particles to play in triggered lightning is to slightly lower the initial breakdown field. The actual electron avalanche should then proceed similarly (with respect to the growth rate of the air conductivity), leading to similar aircraft responses for the pure air and particle cases in terms of peak amplitudes.

## REFERENCES

1. Mazur, V., Fisher, B.D., and Gerlach, J.C., "Conditions Conducive to Lightning Striking an Aircraft in a Thunderstorm," Proc. of the 8th Int. Aero. and Ground Conf. on Lightning and Static Elec., Fort Worth, TX, June 1983.
2. Rudolph, T.H., R.A. Perala, P.M. McKenna and S.L. Parker, "Investigations into the Triggered Lightning Response of the F106B Thunderstorm Research Aircraft," NASA CR-3902, June 1985.
3. Rudolph, T.H., R.A. Perala, C.C. Easterbrook and S.L. Parker, "Development and Application of Linear and Nonlinear Methods for the Interpretation of Lightning Strikes to In-Flight Aircraft," NASA CR-3974, September 1986.
4. Rudolph, T.H., and R.A. Perala, "Linear and Nonlinear Interpretation of the Direct Strike Lightning Response of the NASA F106B Thunderstorm Research Aircraft," NASA CR-3746, 1983.
5. Evteev, B.F., "Electric Field Measurements at the Surface of an Aircraft Model," Studies in Atmospheric Electricity, pp. 118-121, V.P. Kolokolov and T.V. Lobodin, Leningrad, USSR, 1972.
6. JSC Thunderstorm Experiment Result --- Electric Fields, Lightning, and Effects on Space Shuttle Operations, NASA TM X-74682, March 1977.
7. Masanori Hara and Masanori Akasaki, "A Method for Prediction of Gaseous Discharge Threshold Voltages in the Presence of a Conducting Particle," Journal of Electrostatics 2, No. 3, January 1977.
8. Latham, J., and B.J. Mason, "Electrical Charging of Hail Pellets in a Polarizing Electric Field," Proc. Roy. Soc., London, A266, 387-401, 1962.
9. Rustan, P.L., Jr., and J.P. Moreau, "Aircraft Lightning Attachment at Low Altitudes," Proc. of the 10th Int. Aerospace and Ground Conference on Lightning and Static Electricity, Paris, France, June 1985.
10. Fowler, R.J., "A Trajectory Theory of Ionisation in Strong Electric Fields," J. Phys. B, 16, p. 4495, 1983.
11. Gallimberti, I., "The Mechanism of the Long Spark Formation," J. Physique Colloq. 40, C7-193, 1979, R.
12. Hake, R.D., and A.V. Phelps, "Momentum-Transfer and Inelastic-Collision Cross Sections for Electrons in O<sub>2</sub>, CO, and CO<sub>2</sub>," Phys. Rev., Vol. 158, No. 1, June 1967, pp. 70-84.

## REFERENCES - cont'd

13. Mazur, V., L. Ruhnke, T. Rudolph, and R.A. Perala, "Effect of E-Field Mill Location on Accuracy of Electric Field Measurements with Instrumented Airplane," Proc. of the 11th Int. Aero. and Ground Conf. on Lightning and Static Elec., Dayton, OH, June 1986.



# Report Documentation Page

1. Report No. NASA CR-4104		2. Government Accession No.		3. Recipient's Catalog No.	
4. Title and Subtitle Experimental and Analytic Studies of the Triggered Lightning Environment of the F106B				5. Report Date December 1987	
				6. Performing Organization Code	
7. Author(s) Terence Rudolph, Calvin C. Easterbrook, Poh H. Ng, Robert W. Haupt, and Rodney A. Perala				8. Performing Organization Report No. EMA-87-R-37	
				10. Work Unit No. 505-66-21-04	
9. Performing Organization Name and Address Electro Magnetic Applications, Inc. P.O. Box 26263 Denver, CO 80226				11. Contract or Grant No. NAS1-17748	
				13. Type of Report and Period Covered Contractor Report	
12. Sponsoring Agency Name and Address National Aeronautics and Space Administration Langley Research Center Hampton, VA 23665-5225				14. Sponsoring Agency Code	
				15. Supplementary Notes Langley Technical Monitor: Felix L. Pitts	
16. Abstract <p>This report investigates the triggered lightning environment of the F106B aircraft. Scale modeling of the F106B with a metallized model has been done to measure electric field enhancement factors on the aircraft and on canonically shaped conducting objects. These are then compared to numerically determined quantities. Detailed numerical modeling is done of the development of the triggered lightning channel. This is done using nonlinear air chemistry models to model a variety of physical phenomena which occur in a triggered lightning event. The effect of a triggered lightning strike on internal wires in the F106B is investigated using finite difference models and transmission line models to calculate the electromagnetic coupling of lightning currents through seams and joints of the aircraft to internal cables. Time domain waveforms are computed and compared to measured waveforms. The effect of thunderstorm particles on the initial triggering of a lightning strike is investigated. The electric field levels needed to cause air breakdown in the presence and absence of thunderstorm particles are calculated. This is done as a function of the size, shape, and density of the particles.</p>					
17. Key Words (Suggested by Author(s)) Triggered lightning, F106B, scale modeling, numerical modeling, lightning, modeling			18. Distribution Statement Unclassified - Unlimited Subject Category 47		
19. Security Classif. (of this report) Unclassified		20. Security Classif. (of this page) Unclassified		21. No. of pages 120	22. Price A06